Subcontractor Report

Multi-Flexible-Body Analysis for Application to Wind Turbine Control Design

September 10, 1999 – October 31, 2003

D. Lee and D.H. Hodges
Georgia Tech Research Corporation
Atlanta, Georgia

NREL

Multi-Flexible-Body Analysis for Application to Wind Turbine Control Design

September 10, 1999 – October 31, 2003

D. Lee and D.H. Hodges
Georgia Tech Research Corporation
Atlanta, Georgia

NREL

National Renewable Energy Laboratory
1617 Cole Boulevard, Golden, Colorado 80401-3393
303-275-3000 • www.nrel.gov

Available electronically at http://www.osti.gov/bridge

Available for a processing fee to U.S. Department of Energy
and its contractors, in paper, from:
      U.S. Department of Energy
      Office of Scientific and Technical Information
      P.O. Box 62
      Oak Ridge, TN 37831-0062
      phone: 865.576.8401
      fax: 865.576.5728
      email: mailto:reports@adonis.osti.gov

Available for sale to the public, in paper, from:
      U.S. Department of Commerce
      National Technical Information Service
      5285 Port Royal Road
      Springfield, VA 22161
      phone: 800.553.6847
      fax: 703.605.6900
      email: orders@ntis.fedworld.gov
      online ordering: http://www.ntis.gov/ordering.htm

Printed on paper containing at least 50% wastepaper, including 20% postconsumer waste

Preface

This work was undertaken starting in the summer of 1998, when the NREL began to provide support to the principal investigator to begin development of an analysis and computer program to analyze flexible wind-turbines. The end product was to be able to handle aeroelastic analysis and control design but was to take into account such things as blade and tower flexibility, shaft flexibility, nacelle yaw and pitch, and two-bladed, teetering rotors. The principal investigator was indeed fortunate to have been joined in 1999 by a PhD student from Korea with strong analytical skills. Now that he has completed his degree, it is truly astounding how much work he did during his four years at Georgia Tech.

Contents

List of Figures

List of Tables

Chapter 1

Introduction

In the field of wind turbine design, accurate structural modeling is one of the most important research areas. Structural modeling is required to accurately predict the stress field, which is important in determining the turbine's lifetime. Furthermore, it is a primary ingredient in both performance and stability analyses. Finally, it is required for designing controls, which can significantly increase the turbine's efficiency when used properly. In order to be applicable to control design, a structural model needs to be efficient; an accurate but highly complex model might not be useful to a practical design of the control system. So, a feasible structural model could involve some points of compromise between accuracy and efficiency. An advanced modeling methodology is then needed to accurately capture the dynamic behavior of the whole system.

Wind turbines have certain characteristics that should be considered in their structural modeling. First, there are frequently large differences in the stiffnesses of the various subsystems, which calls for the system to be divided into two parts: (a) a collection of bodies that are sufficiently stiff to be modeled as rigid bodies, and (b) a collection of flexible bodies that undergo large displacements and rotations, so they cannot be treated as rigid. This raises research issues concerning how to appropriately model the rigid and flexible bodies and their connectivity. A second characteristic is that the derived mathematical system is time-dependent and periodic. This means that three important factors must be kept in mind. First, a periodic steady-state solution must be found instead of a constant steady-state solution, which is more common in engineering models. Second, stability criteria must be determined in a manner appropriate for a periodic system. Here, a conventional modal analysis would be meaningless, and Floquet theory [4, 10] must be used. Finally, a linearized model that is truly useful in the design of controls must be obtained from linearization about the periodic steady state.

The aim of this research has been to develop a theoretical and computational model for the structural dynamic and aeroelastic analysis of wind turbines, one that is also applicable to control system design. The model is intended to accurately analyze the dynamic and aeroelastic behavior of a wind turbine, which is described as a periodic system, with symbolic computing capability. To achieve this goal, a multi-flexible-body approach is developed. This approach is composed of Kane's method [9] for rigid body subsystem modeling and their connectivity, a mixed finite element method [6] for the flexible body modeling, and blade element momentum theory [3] for the aerodynamic modeling. The unified system model, obtained by combining the subsystem models, is a set of nonlinear ordinary differential equations with periodic coefficients. A computational framework for numerical analysis of the system equations is developed to identify useful information for the system. A finite-element-in-time scheme [1] is built for performing

nonlinear simulations, determining the nonlinear periodic steady-state solution, and analyzing the stability of small perturbations linearized about the nonlinear periodic steady-state solution. Finally, linear system matrices with explicit periodic coefficients are derived for application to control design.

The report is structured in the following manner. A brief description of this work is presented in Chapter 2. Chapter 3 describes the theoretical background of the research. The development of the computational framework is presented in Chapter 4. Chapter 5 presents a numerical validation of our method with numerical results from other codes. A stability analysis of a full wind turbine model, with parametric studies that exercise the key features of the present framework, is presented in in Chapter 6. Finally, Chapter 7 summarizes the contributions of this work. Appendix A presents a user's guide to the computer program WTFlex.

Chapter 2

Description of the Work

The objective of the proposed work is to build a theoretical and computational framework for the aeroelastic analysis of flexible rotating systems, specifically with application to wind turbine control design. This method is based on an integration of Kane's approach [8] for the analysis of the multi-rigid-body subsystem and a mixed finite element method for the analysis of the flexible-body subsystem. The combined analysis is then coupled with an aerodynamic model to form a unified framework for aeroelastic analysis.

Theoretical Modeling

The multi-rigid-bodies subsystem is modeled as a set of interconnected rigid bodies using Kane's method [8]. This method is known to lead to simpler equations than conventional methods because of the possibility of intelligent selection of generalized speeds that yield relatively simple dynamic equations [9].

The flexible portions are represented by geometrically-exact, mixed, beam-finite elements derived from the formulation of Ref. [6]. The use of the mixed formulation allows the direct determination of constraint forces and moments within the beam-finite element and at the boundaries, and thus allows simple connectivity between the finite elements and rigid bodies. Although the number of equations and unknowns increases, the resulting equations are simple and the coefficient matrices are very sparse. Thus, coupling these equations results in a set of nonlinear ordinary differential equations that is simpler in form than a set obtained by other means.

The aerodynamic forces are derived from thin airfoil theory, and the inflow model is from blade element momentum theory. The aerodynamic forces are transformed to be written in terms of variables that are appropriately expressed in the deformed blade frame for coupling of the structural model.

Computational Modeling

The strategy for solving the derived equations is to separate the solution into two parts: a nonlinear periodic steady-state and a transient solution linearized about the periodic steady state. The computational framework for the periodic steady-state can be built using finite elements in time [1]. To reduce the computational cost, a half-period time integration scheme is developed for two-bladed, horizontal-axis wind turbines (HAWTs). The scheme requires a boundary condition at beginning and ending time nodes instead of the more conventional periodicity condition presented in [1]. The steady-state over the whole period then can be calculated

from nonlinear simulation with the initial condition as the steady-state at the initial node, which is obtained from a half-period time integration scheme.

A Floquet stability analysis can be directly undertaken from the framework used to extract the periodic steady-state solution. The stability components implicitly mean the periodic stability of the linear system, which is linearized about the periodic steady-state solution. In this study, a simple method to connect the periodic steady-state and the Floquet stability is developed. Linearization about the periodic steady-state solution yields a set of dynamic equations with periodic coefficients.

This analysis can be directly connected to the application of realistic composite blades with initial twist and curvature. The beam model requires accurate cross-sectional stiffness and inertia coefficients, and these cross-sectional properties can be calculated using VABS (Variational Asymptotic Beam Sectional Analysis) [2]. The method was validated by the successful results of previous work, in which the mixed formulation and VABS are combined for various models [7, 11]. Also, it is possible to use the present framework in designing a controller for the whole wind turbine using symbolic tools.

The symbolic model resulting from the present formulation is one of the most important contributions of the present study. Figure 2.1 shows the advantage of the present framework over other methods of control design. This comparison must be tempered with the realization that there is a great deal of uncertainty in the best of aerodynamic models, although great advances are being made in use of computational fluid dynamics (CFD). Thus, this comparison applies primarily to the structural dynamic response problem and only secondarily to aeroelastic analyses. The first method presented in the figure represents a code with only multi-rigid-body modeling. The symbolic system matrix can be obtained using this methodology, but the accuracy of the solution may not be sufficient to obtain a realistic model, especially for realistic composite blades. Of course the numerical accuracy of this approach may be improved by increasing the number of the rigid bodies; but as the system model becomes larger, the ability of the code to derive a symbolic system matrix becomes strained, and the usefulness of a symbolic system matrix in control design becomes doubtful. The second method represents a code with numerical finite element method modeling. The results of the code would be very accurate, but it is not possible to represent the system as a symbolic time-domain model amenable to preliminary design or control synthesis. So, the model of the system can be marked as a "black box" that produces only time history responses to inputs. If one desires to model a given system with the best possible tool, this would be it. When coupled with CFD it would provide the state-of-the-art in predictive capability from "first principles." The last method in the figure represents the approach to multi-flexible-body modeling described in this report. Using this framework, one can obtain a symbolic system matrix similar to rigid-body modeling while maintaining the accuracy close to that of the numerical FEM modeling. For a complete aeroelastic framework, computational costs would increase considerably. Thus, symbolic computation for the structural modeling may have to be confined to expressing the boundary forces and moments in terms of other state variables. Of course, the number of states appropriate for control design would be problem dependent.
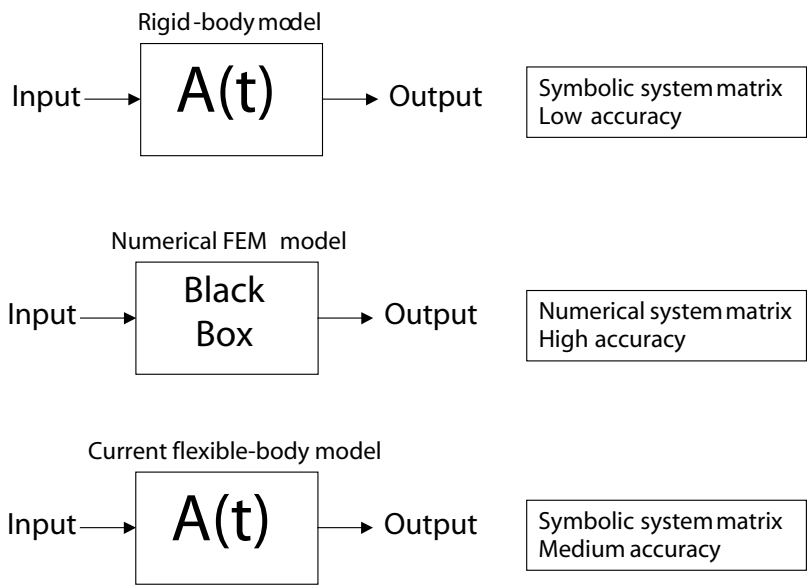
Figure 2.1: Comparison of three types of models showing advantages and disadvantages of each

Chapter 3

Theoretical Background

Structural Theory

All flexible elements are represented as beams using mixed finite elements. The starting point of the flexible body analysis is the weakest variational formulation given in Eq. (74) of Hodges [6]. The weakest form refers to a system description based on the extended Hamilton's principle which contains the least number of spatial or temporal derivatives of the variables. The governing equation in [6] was written as

$$
\begin{aligned}
\int_{t_1}^{t_2} \int_0^\ell & \left\{ \left[\left(\overline{\delta q'} \right)^T - \overline{\delta q}^T \widetilde{K} - \overline{\delta \psi}^T \left(\widetilde{e}_1 + \widetilde{\gamma} \right) \right] F + \left[\left(\overline{\delta \psi'} \right)^T - \overline{\delta \psi}^T \widetilde{K} \right] M \right. \\
& - \left(\overline{\dot{\delta q}}^T - \overline{\delta q}^T \widetilde{\Omega} - \overline{\delta \psi}^T \widetilde{V} \right) P - \left(\overline{\dot{\delta \psi}}^T - \overline{\delta \psi}^T \widetilde{\Omega} \right) H \\
& + \delta \gamma^T \left[\left(\frac{\partial U}{\partial \gamma} \right)^T - F \right] + \delta \kappa^T \left[\left(\frac{\partial U}{\partial \kappa} \right)^T - M \right] - \delta V^T \left[\rho \left(V - \widetilde{\overline{\xi}} \Omega \right) - P \right] \\
& - \delta \Omega^T \left(I \Omega + \rho \widetilde{\overline{\xi}} V - H \right) + \overline{\delta F}^T \left[e_1 + \widetilde{k} u - C^T \left(e_1 + \gamma \right) \right] - \left(\overline{\delta F'} \right)^T u \\
& - \overline{\delta P}^T \left(v + \widetilde{\omega} u - C^T V \right) + \overline{\dot{\delta P}}^T u + \overline{\delta M}^T \left(\Delta + \frac{\widetilde{\theta}}{2} + \frac{\theta \theta^T}{4} \right) \left(C k - k - \kappa \right) \\
& - \left(\overline{\delta M'} \right)^T \theta - \overline{\delta H}^T \left(\Delta + \frac{\widetilde{\theta}}{2} + \frac{\theta \theta^T}{4} \right) \left(C \omega - \Omega \right) + \overline{\dot{\delta H}}^T \theta \\
& \left. - \overline{\delta q}^T f - \overline{\delta \psi}^T m \right\} dx_1 dt \\
= & - \int_0^\ell \left(\overline{\delta q}^T \hat{P} + \overline{\delta \psi}^T \hat{H} - \overline{\delta P}^T \hat{u} - \overline{\delta H}^T \hat{\theta} \right) \Big|_{t_1}^{t_2} dx_1 \\
& + \int_{t_1}^{t_2} \left(\overline{\delta q}^T \hat{F} + \overline{\delta \psi}^T \hat{M} - \overline{\delta F}^T \hat{u} - \overline{\delta M}^T \hat{\theta} \right) \Big|_0^\ell dt,
\end{aligned}
\tag{3.1}
$$

where u is the column matrix of displacement measures of the beam reference line in the b basis (the undeformed beam cross-sectional frame basis), θ is the column matrix of Rodrigues parameters, so that the

matrix of direction cosines C, relating the B basis (the deformed beam cross-sectional frame basis) to the b basis, is given by

$$C = \frac{\Delta \left(1 - \frac{1}{4}\theta^T\theta\right) - \widetilde{\theta} + \frac{1}{2}\theta\theta^T}{1 + \frac{1}{4}\theta^T\theta},$$

(3.2)

F is the column matrix of section force resultant measures in the B basis, M is the column matrix of section moment resultant measures in the B basis, P is the column matrix of section linear momentum measures in the B basis, H is the column matrix of section angular momentum measures in the B basis, γ is the column matrix of force strains, κ is the column matrix of moment strains, k is the curvature vector for the undeformed beam in the b basis, K is the curvature vector for the deformed beam in the B basis, V is the column matrix of velocity measures of the beam reference line in the B basis, Ω is the column matrix of cross-sectional angular velocity measures in the B basis, ξ is the position of the section mass center of the undeformed beam relative to the undeformed beam reference line in the b basis, f is the distributed applied force per unit length in the B basis, m is the distributed applied moment per unit length (in the B basis), U is the strain energy per unit length, v and w are the generalized speeds of the body/frame to which the flexible subsystem is attached, Δ is the 3×3 identity matrix, e_1 is $\lfloor 1,0,0 \rfloor^T$, the tilde transforms a 3×1 column matrix into an antisymmetric 3×3 matrix, such as

$$\widetilde{\theta} = \begin{bmatrix} 0 & -\theta_3 & \theta_2 \\ \theta_3 & 0 & -\theta_1 \\ -\theta_2 & \theta_1 & 0 \end{bmatrix},$$

(3.3)

$\overline{\delta q}$ is the column matrix of virtual displacement measures in the B basis, $\overline{\delta\psi}$ is the column matrix of virtual rotation measures in the B basis, $\overline{\delta F}$ is the column matrix of virtual force transformed to the b basis, $\overline{\delta M}$ is a column matrix of virtual moment test functions, $\overline{\delta P}$ is the column matrix of virtual linear momentum measures transformed to the b basis, and $\overline{\delta H}$ is a column matrix of virtual angular momentum test functions. The overbar of the virtual variables indicate they are not the variation of a function. All "hatted" terms in the right side of the equation are the variable values at the boundaries. All "primed" terms and "dotted" terms represent the space and time derivative of the terms respectively.

The force variables (F and M) are related to strain measures (γ and κ) in accordance with the 1-D constitutive law as

$$\left\{ \begin{matrix} F \\ M \end{matrix} \right\} = [S] \left\{ \begin{matrix} \gamma \\ \kappa \end{matrix} \right\},$$

(3.4)

where $[S]$ is the cross-sectional stiffness matrix. The stiffness matrix may be calculated using VABS or other suitable means and is used to eliminate γ and κ in favor of F and M.

Moreover, the momentum variables (P and H) are related linearly to the velocity variables (V and Ω). When the locus of cross-section mass centroids is chosen as the reference line, these relations can be written for an arbitrary cross-section of the beam as

$$\left\{ \begin{matrix} P \\ H \end{matrix} \right\} = \begin{bmatrix} m\Delta & 0 \\ 0 & I \end{bmatrix} \left\{ \begin{matrix} V \\ \Omega \end{matrix} \right\},$$

(3.5)

where m is the mass per unit length of the beam element, and I is the moment of inertia matrix of the cross-section. By virtue of Eq. (3.5), the quantities P and H are eliminated in favor of V and Ω, the "generalized speeds" of the beam element.

The weakest form in Eq. (3.1) is integrated by parts in time, and the time integration is removed from variational quantities. This way only the spatial dependence is accounted for in the finite element modeling. The final weak form is obtained by removing some variables using Eq. (3.4) and (3.5) then reduces to

$$
\begin{aligned}
\int_0^\ell &\left\{ \left[\overline{\delta q}'^T - \overline{\delta q}^T \widetilde{\kappa} - \overline{\delta \psi}^T (\widetilde{e}_1 + \widetilde{\gamma}) \right] F + \overline{\delta q}^T \dot{P} \right. \\
&+ \left(\overline{\delta q}^T \widetilde{\Omega} + \overline{\delta \psi}^T \widetilde{V} \right) P + \left(\overline{\delta \psi}'^T - \overline{\delta \psi}^T \widetilde{\kappa} \right) M \\
&+ \overline{\delta \psi}^T \left(\dot{H} + \widetilde{\Omega} H \right) + \overline{\delta F}^T \left[e_1 - C^T (e_1 + \gamma) \right] \\
&- \overline{\delta F}'^T u - \overline{\delta M}^T \left(\Delta + \frac{1}{2}\widetilde{\theta} + \frac{1}{4}\theta\theta^T \right) \kappa - \overline{\delta M}'^T \theta \\
&- \overline{\delta P}^T \left[v + \widetilde{\omega} u - C^T V + \dot{u} \right] \\
&- \overline{\delta H}^T \left[\left(\Delta + \frac{1}{2}\widetilde{\theta} + \frac{1}{4}\theta\theta^T \right)(C\omega - \Omega) + \dot{\theta} \right] \\
&\left. - \overline{\delta q}^T f - \overline{\delta \psi}^T m \right\} dx_1 \\
&= \left(\overline{\delta q}^T \hat{F} + \overline{\delta \psi}^T \hat{M} - \overline{\delta F}^T \hat{u} - \overline{\delta M}^T \hat{\theta} \right) \Big|_0^\ell .
\end{aligned}
\tag{3.6}
$$

Dynamic Theory

Some elements of wind turbine systems are relatively stiff, and they are reasonably modeled as a multi-rigid-body system. The current approach applies Kane's approach to model the multi-rigid-body portion [8]. In Kane's approach, the equations of motion are described in terms of configuration variables that are used in conventional dynamic modeling, and motion variables that are a linear combination of the time derivatives of the former. Here, the definition of the motion variables, which is expressed as kinematical differential equations, strongly affects the length of the equations of motion. The following explains the procedure for selecting appropriate generalized speeds, which produce a compact set of governing equations. Here, we assume that the rigid bodies are connected to each other in such a way that there only one or two degrees of freedom are introduced by the connectivity. The case for three degrees of freedom is excluded here, because the selection of appropriate generalized speeds is not unique in that case [9].

If rigid bodies A and B have a single common axis, parallel to which is the unit vector $\mathbf{i}$, the preferred definition of the generalized speed is

$$
U_o = {}^n\boldsymbol{\omega}^B \cdot \mathbf{i}.
\tag{3.7}
$$

Here, ${}^n\boldsymbol{\omega}^B$ is the angular velocity of body B with respect to the inertial frame n. If rigid bodies B and C are connected in such a way that ${}^B\boldsymbol{\omega}^C$ can be expressed as $\sigma_1\mathbf{i} + \sigma_2\mathbf{j}$, where σ_1 and σ_2 are time-dependent scalars, while $\mathbf{i}$ and $\mathbf{j}$ are unit vectors permanently fixed in B and C, respectively, the generalized speeds are

$$
\begin{aligned}
U_x &= \left({}^n\boldsymbol{\omega}^C - \sigma_2\mathbf{j} \right) \cdot \mathbf{i} \\
U_y &= {}^n\boldsymbol{\omega}^C \cdot \mathbf{j}.
\end{aligned}
\tag{3.8}
$$

Finally, if body A is clamped to a flexible body, the following definition would match the kinematical equations of the finite element model for the flexible body:

$$\lfloor U_1\, U_2\, U_3 \rfloor^T = {}^n\boldsymbol{\omega}^T \cdot \lfloor \mathbf{t}_1\, \mathbf{t}_2\, \mathbf{t}_3 \rfloor^T$$
$$\lfloor U_4\, U_5\, U_6 \rfloor^T = {}^n\boldsymbol{v}^T \cdot \lfloor \mathbf{t}_1\, \mathbf{t}_2\, \mathbf{t}_3 \rfloor^T. \tag{3.9}$$

Here, $\mathbf{t}_i$ is the set of unit vectors at the point where the rigid-body system is connected to the flexible body.

Using the choices of generalized speed described earlier, one can generate the nonlinear, time-dependent equations of motion for the multi-rigid-body subsystem using Autolev,$^{\text{TM}}$ a commercially available symbol manipulator capable of deriving equations of motion of rigid-body mechanisms using Kane's method. (Autolev was developed by Online Dynamics, Inc.) The equations of motion for the current model can be represented in symbolic form as

$$G_i(\dot{U}, U, q, F_e, M_e) = 0, \qquad i = 1, 2, \cdots, n, \tag{3.10}$$

where

$$U = \lfloor U_1\, U_2\, \cdots\, U_n \rfloor^T$$
$$q = \lfloor q_1\, q_2\, \cdots\, q_n \rfloor^T. \tag{3.11}$$

Here, U_i are generalized speeds, q_i are generalized coordinates, and n is the degrees of freedom of the multi-rigid-body system. Also, F_e and M_e are the external force and moment components, which would be calculated in the flexible-body analysis.

The rigid-body subsystems are coupled with flexible subsystems by transferring the information at the interface between them. For example, in the mixed finite element model for a blade, the blade root is clamped to a rigid-body called H, and thus the blade root displacement $\hat{u}_0$ and orientation variables $\hat{\theta}_0$ are set equal to zero. The inertial velocity of the mass center of H and angular velocity of H define the motion of the frame to which the blades are clamped and thus determine the variables v_0 (the blade root velocity written in b frame) and ω needed in the mixed finite element formulation. One can solve for the blade root force $\hat{F}_0$ and moment $\hat{M}_0$ in terms of the element internal variables. This set of forces is applied at the points where the blades are attached to the hub, and the moment is applied to H. Accomplishing the above transfer couples the two systems, and one obtains the equations of motion for the complete system.

Aerodynamic Theory

Fig. 3.1 shows the frames used in aerodynamic modeling. Frame a is fixed in the rotor hub at the rotor, which is rotating with angular speed Ω about the $\mathbf{a}_3$ axis. Frame B is fixed at the deformed beam reference line, which coincides with $\mathbf{B}_1$ axis at each spatial node. Here it is assumed that the line of the aerodynamic center coincides with the deformed beam reference line. Frame Z fixes at the zero-lift line, which coincides with the $\mathbf{Z}_2$ axis. For simplicity, the distinction between the Z and B frames is ignored, so that the zero-lift line is along $\mathbf{B}_2$. The relative wind velocity vector is denoted by $\mathbf{W} = W_2\mathbf{B}_2 + W_3\mathbf{B}_3$. Therefore, the angle of attack is the angle between $\mathbf{B}_2$ and $\mathbf{W}$.

The aerodynamic loads are derived from thin-airfoil theory. These distributed loads stem from the circulatory lift, L_C; the noncirculatory lift, L_{NC}; the circulatory moment, M_C; the noncirculatory moment, M_{NC}; and the profile drag, D. In the mixed variational formulation, these loads are the force per unit length
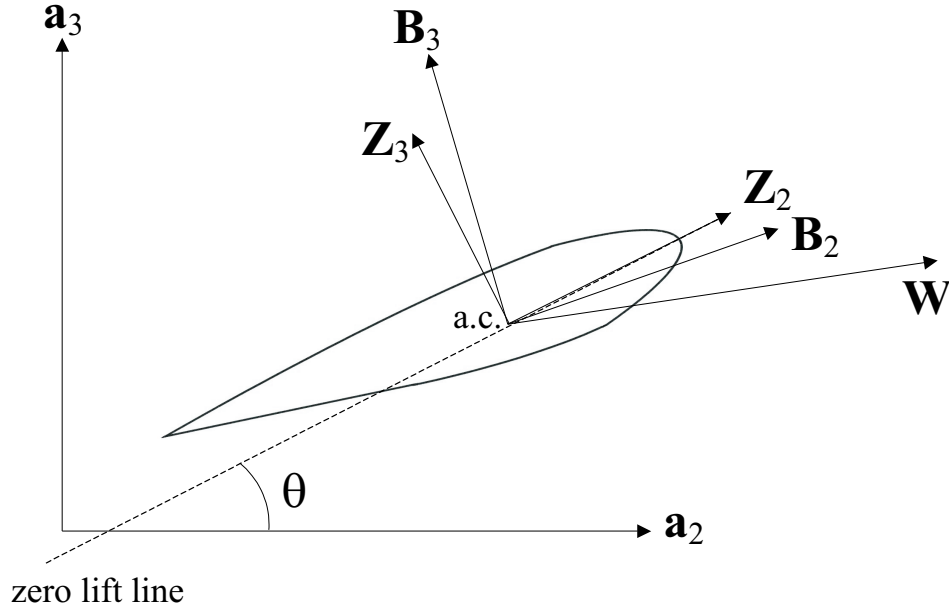
Figure 3.1: Schematic of airfoil and aerodynamic forces

f_B applied at the reference line and the moment per unit length m_B about the reference line, both of which are expressed in the deformed beam cross-sectional frame B:

$$f_B = \frac{\rho_\infty c a}{2} \left\{ \begin{array}{c} 0 \\ \left(W_{B_3} - \frac{c}{2}\Omega_1\right) W_{B_3} - \frac{c_d}{a} W_{B_2} W \\ \left(\frac{c}{2}\Omega_1 - W_{B_3}\right) W_{B_2} - \frac{c_d}{a} W_{B_3} W - \frac{c}{4}\dot{V}_{B_3} + \frac{c^2}{16}\dot{\Omega}_1 \end{array} \right\}$$

$$m_B = -\frac{1}{32}\rho_\infty c^3 a \left\{ \begin{array}{c} W_{B_2}\Omega_1 - \dot{V}_{B_3} + \frac{3c}{8}\dot{\Omega}_1 \\ 0 \\ 0 \end{array} \right\}.$$

(3.12)

Here, Ω_1 is the component of the cross-sectional angular velocity parallel to the $\mathbf{B}_1$ direction, ρ_∞ is the mass density of the air, c is the airfoil chord length, a is the lift curve slope, c_d is the sectional drag coefficient, V_{B_3} is the cross-sectional reference line velocity component normal to the zero-lift line, W is the magnitude of the relative wind velocity, and W_{B_2} and W_{B_3} are the components of the relative wind velocity in the B basis. The expressions of W_{B_2} and W_{B_3} are

$$W_{B_2} = e_2^T(V_B + C^{Ba}\lambda e_3) = e_2^T C(v_b + \widetilde{\omega}_b u_b + \dot{u}_b + C^{ba}\lambda e_3)$$
$$W_{B_3} = e_3^T(V_B + C^{Ba}\lambda e_3) = e_3^T C(v_b + \widetilde{\omega}_b u_b + \dot{u}_b + C^{ba}\lambda e_3).$$

(3.13)

where λ is the induced velocity, ω_b is the column matrix of angular velocity measures of the undeformed blade reference frame in the b basis, and C^{ba} is the transformation matrix from rotating frame a to un-

deformed blade reference frame b, which reduce to the identity matrix if there is no initial curvature and twist.

The inflow is calculated using the following equation from [3] as

$$\lambda = V_\infty + \Omega_0 R \left(\frac{\sigma a}{16}\right) \left[-1 + \sqrt{1 + \frac{32 x \theta}{\sigma a R}}\right].$$ (3.14)

where V_∞ is wind free-stream speed, Ω_0 is the nominal rotor angular speed, R is the radius of the rotor, σ is the solidity, x is the minimum distance from the rotating axis to the point of interest, and θ is the angle between the zero-lift line and the rotor's plane of rotation. Equation (3.14) can be used with simplifying assumptions that the lift coefficient is linear, the drag coefficient is small, and total vertical flow on the a_3 axis is positive [5]. Otherwise, the second term in the right side of Eq. (3.14) would be a function of V_∞.

To calculate θ, let $\mathbf{h} = C_{21}^{Za} \mathbf{a}_1 + C_{22}^{Za} \mathbf{a}_2$ represent the projection of $\mathbf{Z}_2$ (the zero-lift line unit vector) in the $\mathbf{a}_1$-$\mathbf{a}_2$ plane (i.e., the "plane of rotation"). Introduction of the rule of dot products,

$$\mathbf{Z}_2 \cdot \mathbf{h} = |\mathbf{Z}_2||\mathbf{h}| \cos \theta$$ (3.15)

leads to

$$\theta = \cos^{-1} \left[\sqrt{\left(C_{21}^{ZA}\right)^2 + \left(C_{22}^{ZA}\right)^2}\right] \operatorname{sign}\left(C_{23}^{Za}\right).$$ (3.16)

The sign of θ was determined based on the orientation of $\mathbf{Z}_2$: if the $\mathbf{a}_3$ component of $\mathbf{Z}_2$ is positive, then the airfoil is pitched nose up; the sign of θ can therefore be determined by the sign of C_{23}^{Za} since $\mathbf{Z}_2 \cdot \mathbf{a}_3 = C_{23}^{Za}$.

The remaining quantities needed to calculate the inflow are

$$x = \sqrt{(\mathbf{R} \cdot \mathbf{a}_1)^2 + (\mathbf{R} \cdot \mathbf{a}_2)^2}$$ (3.17)

$$R = [x]_{x_1 = \ell}$$ (3.18)

$$\sigma = \frac{bc}{\pi R},$$ (3.19)

where $\mathbf{R}$ is the position vector from the point at the center of rotation to a point on the deformed reference line, and b equals the number of rotor blades.

Note that the aerodynamic theory in this work is only applicable over the linear region of the lift curve. So, it has very limited applicability for realistic analysis of wind turbines, which should include such phenomena as nonlinear effects, the ground effect because of proximity to the ground, and unsteady wake effects. For more practical applications, future research is recommended to incorporate more sophisticated aerodynamic modeling. While such research is believed to be feasible, the calculation of symbolic system matrices will almost certainly be impossible.

Chapter 4

Development of the Computational Model

The previously described models for the flexible-body subsystem, the rigid-body subsystem, and aerodynamics are integrated into a unified framework for the aeroelastic analysis of a whole system. Also, the framework can be easily used for structural dynamic analysis simply by removing the aerodynamic terms.

Nonlinear Simulation

The nonlinear simulation is essential to an investigation of the behavior of the system with various conditions. The time-finite element method can be used to do the analysis. This is undertaken by converting the formulation into its weakest form in both space and time. Thus, the spatial and temporal derivatives are transferred to the variations via integration by parts and weak enforcement of boundary and initial and final conditions. The analytical form of the governing equation is given in Eq. (3.1), removing some variables by Eq. (3.4) and Eq. (3.5). To obtain space-time finite elements, the following shape functions can be used:

$$
\begin{aligned}
\overline{\delta q} &= \overline{\delta q}_i \left(1 - \eta\right)\left(1 - \tau\right) + \overline{\delta q}_j \eta \left(1 - \tau\right) \\
&\quad + \overline{\delta q}_k \eta \tau + \overline{\delta q}_l \left(1 - \eta\right)\tau \\
\overline{\delta \psi} &= \overline{\delta \psi}_i \left(1 - \eta\right)\left(1 - \tau\right) + \overline{\delta \psi}_j \eta \left(1 - \tau\right) \\
&\quad + \overline{\delta \psi}_k \eta \tau + \overline{\delta \psi}_l \left(1 - \eta\right)\tau \\
\overline{\delta F} &= \overline{\delta F}_i \left(1 - \eta\right) + \overline{\delta F}_j \eta \\
\overline{\delta M} &= \overline{\delta M}_i \left(1 - \eta\right) + \overline{\delta M}_j \eta \\
\overline{\delta P} &= \overline{\delta P}_k \left(1 - \tau\right) + \overline{\delta P}_l \tau \\
\overline{\delta H} &= \overline{\delta H}_k \left(1 - \tau\right) + \overline{\delta H}_l \tau,
\end{aligned}
\tag{4.1}
$$

where η and τ are dimensionless spatial and temporal coordinates within the element. With these shape functions, along with constant shape functions for all element variables, the spatial and temporal integration of the governing equation can be performed explicitly to obtain a set of nonlinear algebraic equations. Figure 4.1 shows the composition of the space-time finite element with virtual variables.
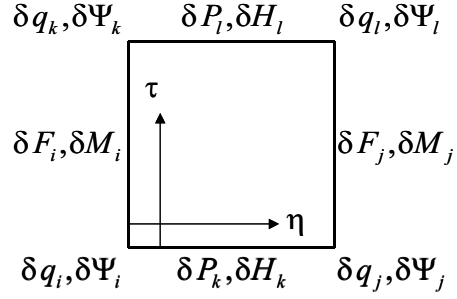
Figure 4.1: Space-time finite element and virtual variables

The state variables can be discretized using nodal variables at the four corners of a space-time finite element. If a constant shape function is used, the state variables can be simply expressed as

$$
\begin{aligned}
u &= \frac{u_i + u_j + u_k + u_l}{4} \\
\theta &= \frac{\theta_i + \theta_j + \theta_k + \theta_l}{4} \\
V &= \frac{V_i + V_j + V_k + V_l}{4} \\
\Omega &= \frac{\Omega_i + \Omega_j + \Omega_k + \Omega_l}{4} \\
F &= F_m \\
M &= M_m,
\end{aligned}
\tag{4.2}
$$

where variables with subscripts i, j, k, or l denote the nodal variables, and the variables with subscript m denote the element variables.

The alternative way to build the set of equations is to apply the shape function for the space finite element to Eq. (3.6):

$$
\begin{aligned}
\overline{\delta q} &= \overline{\delta q}_i \left(1 - \eta\right) + \overline{\delta q}_{i+1}\eta \\
\overline{\delta \psi} &= \overline{\delta \psi}_i \left(1 - \eta\right) + \overline{\delta \psi}_{i+1}\eta \\
\overline{\delta F} &= \overline{\delta F}_i \left(1 - \eta\right) + \overline{\delta F}_{i+1}\eta \\
\overline{\delta M} &= \overline{\delta M}_i \left(1 - \eta\right) + \overline{\delta M}_{i+1}\eta \\
\overline{\delta P} &= \overline{\delta P}_i \\
\overline{\delta H} &= \overline{\delta H}_i.
\end{aligned}
\tag{4.3}
$$

By collecting terms with various test function coefficients, one can obtain the set of finite element

equations. The whole set of equations for a blade is

$$\overline{\delta q}_1 : -\overline{F}_1 + \frac{\Delta x}{2}\left(\dot{\overline{P}}_1 + \widetilde{\overline{\Omega}}_1\,\overline{P}_1 - \widetilde{\overline{\kappa}}_1\overline{F}_1 - mg_B\right) + \hat{F}_0 = 0$$

$$\overline{\delta q}_i : -\overline{F}_{i+1} + \frac{\Delta x}{2}\left(\dot{\overline{P}}_{i+1} + \widetilde{\overline{\Omega}}_{i+1}\,\overline{P}_{i+1} - \widetilde{\overline{\kappa}}_{i+1}\overline{F}_{i+1} - mg_B\right) + \overline{F}_i$$
$$+ \frac{\Delta x}{2}\left(\dot{\overline{P}}_i + \widetilde{\overline{\Omega}}_i\,\overline{P}_i - \widetilde{\overline{\kappa}}_i\overline{F}_i - mg_B\right) = 0$$

$$\overline{\delta q}_{n+1} : \overline{F}_n + \frac{\Delta x}{2}\left(\dot{\overline{P}}_n + \widetilde{\overline{\Omega}}_n\,\overline{P}_n - \widetilde{\overline{\kappa}}_n\overline{F}_n - mg_B\right) = 0$$

$$\overline{\delta \psi}_1 : -\overline{M}_1 + \frac{\Delta x}{2}\left[\dot{\overline{H}}_1 + \widetilde{\overline{\Omega}}_1\,\overline{H}_1 - \widetilde{\overline{\kappa}}_1\overline{M}_1 - \left(\widetilde{e}_1 + \widetilde{\overline{\gamma}}_1\right)\overline{F}_1\right] + \hat{M}_0 = 0$$

$$\overline{\delta \psi}_i : -\overline{M}_{i+1} + \frac{\Delta x}{2}\left[\dot{\overline{H}}_{i+1} + \widetilde{\overline{\Omega}}_{i+1}\,\overline{H}_{i+1} - \widetilde{\overline{\kappa}}_{i+1}\overline{M}_{i+1} - \left(\widetilde{e}_1 + \widetilde{\overline{\gamma}}_{i+1}\right)\overline{F}_{i+1}\right] + \overline{M}_i$$
$$+ \frac{\Delta x}{2}\left[\dot{\overline{H}}_i + \widetilde{\overline{\Omega}}_i\,\overline{H}_i - \widetilde{\overline{\kappa}}_i\overline{M}_i - \left(\widetilde{e}_1 + \widetilde{\overline{\gamma}}_i\right)\overline{F}_i\right] = 0$$

$$\overline{\delta \psi}_{n+1} : \overline{M}_n + \frac{\Delta x}{2}\left[\dot{\overline{H}}_n + \widetilde{\overline{\Omega}}_n\,\overline{H}_n - \widetilde{\overline{\kappa}}_n\overline{M}_n - \left(\widetilde{e}_1 + \widetilde{\overline{\gamma}}_n\right)\overline{F}_n\right] = 0$$

$$\overline{\delta F}_1 : \overline{u}_1 + \frac{\Delta x}{2}\left[e_1 - \overline{C}_1^T\left(e_1 + \overline{\gamma}_1\right)\right] = 0 \qquad (4.4)$$

$$\overline{\delta F}_i : \overline{u}_{i+1} + \frac{\Delta x}{2}\left[e_1 - \overline{C}_{i+1}^T\left(e_1 + \overline{\gamma}_{i+1}\right)\right] - \overline{u}_i + \frac{\Delta x}{2}\left[e_1 - \overline{C}_i^T\left(e_1 + \overline{\gamma}_i\right)\right] = 0$$

$$\overline{\delta F}_{n+1} : -\overline{u}_n + \frac{\Delta x}{2}\left[e_1 - \overline{C}_n^T\left(e_1 + \overline{\gamma}_n\right)\right] + \hat{u}_{n+1} = 0$$

$$\overline{\delta M}_1 : \overline{\theta}_1 - \frac{\Delta x}{2}\left(\Delta + \frac{1}{2}\widetilde{\overline{\theta}}_1 + \frac{1}{4}\overline{\theta}_1\,\overline{\theta}_1^T\right)\kappa_1 = 0$$

$$\overline{\delta M}_i : \overline{\theta}_{i+1} - \frac{\Delta x}{2}\left(\Delta + \frac{1}{2}\widetilde{\overline{\theta}}_{i+1} + \frac{1}{4}\overline{\theta}_{i+1}\,\overline{\theta}_{i+1}^T\right)\kappa_{i+1}$$
$$- \overline{\theta}_i - \frac{\Delta x}{2}\left(\Delta + \frac{1}{2}\widetilde{\overline{\theta}}_i + \frac{1}{4}\overline{\theta}_i\,\overline{\theta}_i^T\right)\kappa_i = 0$$

$$\overline{\delta M}_{n+1} : -\overline{\theta}_n - \frac{\Delta x}{2}\left(\Delta + \frac{1}{2}\widetilde{\overline{\theta}}_n + \frac{1}{4}\overline{\theta}_n\,\overline{\theta}_n^T\right)\kappa_n + \hat{\theta}_{n+1} = 0$$

$$\overline{\delta P}_i : \dot{\overline{u}}_i - \overline{C}_i^T\overline{V}_i + v + \widetilde{\omega}\left(\frac{x_i}{2}e_1 + \overline{u}_i\right) = 0$$

$$\overline{\delta H}_i : \dot{\overline{\theta}}_i - \left(\Delta + \frac{1}{2}\widetilde{\overline{\theta}}_i + \frac{1}{4}\overline{\theta}_i\,\overline{\theta}_i^T\right)\left(\overline{\Omega}_i - \overline{C}\omega\right) = 0,$$

where Δx is the length of a spatial element.

Here, the equations corresponding to $\overline{\delta q}_i$ and $\overline{\delta \psi}_i$ are the discretized equations of motions, equations corresponding to $\overline{\delta F}_i$ and $\overline{\delta M}_i$ are the discretized strain-displacement relations, and equations corresponding $\overline{\delta P}_i$, $\overline{\delta H}_i$ are the velocity-displacement kinematical equations. The overbar or hat of the variables indicates the element or boundary variables, respectively and the subscript 1 or $n+1$ of the virtual variables indicates the root or tip of the system, respectively. Note that using the equations above, the blade root forces ($\hat{F}_0$) and moments ($\hat{M}_0$) can be explicitly written in terms of the other variables and can be easily transferred to the discrete portion of the system. On the other hand, v and ω appearing in the kinematic equations are calculated by the rigid-body analysis, as discussed in the next section. Also, note that P, H, γ and κ are still used in the equation above to represent the equation in a more compact manner, although they are eliminated using V, Ω, F and M in the actual computation.

To obtain the algebraic equations, one needs to transform the variables with time derivative to nodal variables at the ends of the time element, so that

$$\dot{\bar{u}} = \frac{\bar{u}_{j+1} - \bar{u}_j}{\Delta t}$$
$$\dot{\bar{\theta}} = \frac{\bar{\theta}_{j+1} - \bar{\theta}_j}{\Delta t}$$
$$\dot{\bar{V}} = \frac{\bar{V}_{j+1} - \bar{V}_j}{\Delta t}$$
$$\dot{\bar{\Omega}} = \frac{\bar{\Omega}_{j+1} - \bar{\Omega}_j}{\Delta t},$$

(4.5)

where Δt is the length of a time element.

The undifferentiated variables can be discretized as

$$\bar{u} = \frac{\bar{u}_{j+1} + \bar{u}_j}{2}$$
$$\bar{\theta} = \frac{\bar{\theta}_{j+1} + \bar{\theta}_j}{2}$$
$$\bar{V} = \frac{\bar{V}_{j+1} + \bar{V}_j}{2}$$
$$\bar{\Omega} = \frac{\bar{\Omega}_{j+1} + \bar{\Omega}_j}{2}.$$

(4.6)

Here, if the above variables defined in a space element are transformed to the nodal variables at the ends of a space element, the final derived set of equations from the above central difference scheme is equivalent to those from the finite element in time.
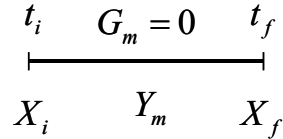
Figure 4.2: Schematic of nonlinear simulation in a time step

Using one of the above procedures, one can derive a set of nonlinear algebraic equations that should be satisfied for each time element, given in Fig. 4.2 as

$$G_m \left(X_f, X_i, Y_m \right) = 0,$$

(4.7)

where X_f and X_i are the column matrix of state variables at the ending node and beginning node of the time element, respectively and Y_m is the column matrix of state variables within the time element. The column matrices are expressed as

$$X = \lfloor q\, U\, u\, \theta\, V\, \Omega \rfloor^T$$
$$Y = \lfloor F\, M \rfloor^T.$$

(4.8)

Since the operators have explicit expressions, the Jacobian matrix can be derived explicitly by differentiation, and the solution of the equations at each time step can be calculated by the Newton-Rapson method. So, the time history of the system can be obtained step by step with specified initial conditions.

Periodic Steady-State Analysis

Wind turbine blades in general, but especially those of HAWTs, the most common configuration in the industry, experience periodic excitation due to gravity. To find the aeroelastic stability characteristics, the periodic steady-state solution should be calculated. Also, the governing equations are then linearized about the steady-state solution to obtain the perturbation equations. One way to obtain the periodic steady-state solution is to build a closed form of equations for one period using the Jacobian matrix obtained from the nonlinear simulation. In this case, one may use the periodicity conditions instead of the initial conditions.

Figure 4.3: Schematic of time integration over one period

The equations in one period, given in Fig. 4.3, are expressed as

$$G_i\left(X_0, Z_i\right) = 0, \qquad i = 1, 2, \cdots, N,$$ (4.9)

where $Z_i = \lfloor X_i\, Y_i \rfloor^T$, and N is the number of time elements in one period. The periodicity condition is

$$X_N = X_0.$$ (4.10)

The final set of equations for one period can be expressed as

$$G\left(Z\right) = 0$$
$$Z = \lfloor Z_1\, Z_2\, \cdots Z_N \rfloor^T.$$ (4.11)

Fast Periodic Steady-State Analysis

The computational cost to obtain the periodic steady-state solution might be expensive, because the size of Eq. (4.11) can be huge. And as the number of space elements increases, the cost would exponentially increase to satisfy the level of aspect ratio (i.e., the ratio of the number of time elements to the number

of space elements) for numerical stability. To make the algorithm as computationally efficient as possible, we can restrict the analysis to wind turbines with identical blades and make use of the symmetric dynamic characteristics of the rotor[1]. This way all blades have the same values for their respective state variables at a given azimuth angle in the periodic steady-state framework. Moreover, the time integral of the period divided by the number of blades will produce the same answer as that determined from the time integral over a period. Peters applied a similar idea to the Floquet analysis [12], making possible a significant reduction in computational effort.

The framework for realizing the idea is the same as the previous one, except for the periodicity condition in Eq. (4.10). If the system is composed of only blades, the periodicity condition is

$$\begin{aligned} X_n^{j+1} &= X_0^j, \quad j = 1, 2, \cdots, b \\ n &= N/b, \end{aligned} \tag{4.12}$$

where j denotes each blade, b is the number of blades, and N is the number of time elements of the whole period. There is no difference between states at a given azimuth angle relative to a reference azimuth position. The mathematical expression for the periodicity condition depends on the composition of each system.

This study describes a specific case for a whole wind turbine system composed of two blades, a teetering hub, a rotating shaft, a yawing nacelle, and a flexible tower fixed in the ground. That is the most common model of HAWT. The periodic steady state of the system can be obtained by the finite element-in-time assembly over the half period, as given in Fig. 4.4.

The state vector in Eq. (4.9) can be symbolically expressed as

$$X_i = \lfloor X_i^t \, X_i^n \, X_i^s \, X_i^h \, X_i^u \, X_i^l \, \rfloor^T, \quad i = 1, 2, \cdots, N, \tag{4.13}$$

where X^t, X^n, X^s, X^h, X^u, and X^l denote the state vector for tower, nacelle, shaft, hub, upper blade, and lower blade, respectively at a time node i.

The periodicity condition is

$$\begin{aligned} X_{N/2}^t &= X_0^t \\ X_{N/2}^n &= X_0^n \\ X_{N/2}^s &= X_0^s \\ X_{N/2}^h &= -X_0^h \\ X_{N/2}^u &= X_0^l \\ X_{N/2}^l &= X_0^u. \end{aligned} \tag{4.14}$$

A similar condition with a minor change in symbolic expression can be applied for state vector Y containing state variables within an element. Eq. (4.11) can be rewritten as

$$\begin{aligned} G\left(Z\right) &= 0 \\ Z &= \lfloor Z_1 \, Z_2 \, \cdots Z_{N/2} \rfloor^T. \end{aligned} \tag{4.15}$$

---

[1]The analysis could be configured to simulate the behavior of a wind turbine with nonidentical blades, but stability analysis of such a system would be prohibitively expensive.

X_0

t_N G_1

Z_N t_1

Z_1

G_2

half period Z_2 t_2
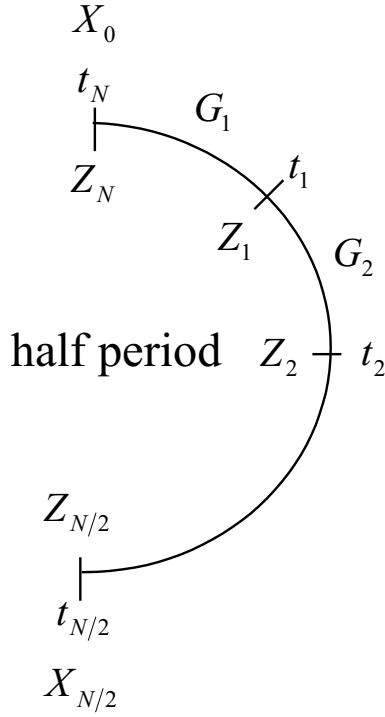
$Z_{N/2}$

$t_{N/2}$

$X_{N/2}$

Figure 4.4: Schematic of time integration over half period

The number of equations in Eq. (4.15) is half the number of equations in Eq. (4.11). Also, the dimension of the Jacobian matrix for numerical computation is a quarter of the original one over the whole period.

By solving Eq. (4.15), one can obtain the periodic steady-state solution over the half period. The periodic steady-state solution over the whole period can be performed by using the nonlinear simulation presented in Eq. (4.7) over one period with the initial condition taken from the steady-state solution at time node 0 (X_0), which is obtained from the periodic steady-state analysis over the half period.

Floquet Stability from Periodic Steady-State Solution

The framework for the periodic steady-state solution can be easily modified to find the stability of a nonlinear steady-state solution. The Floquet theory describes the stability of the periodic systems based on the eigenvalues of the Floquet transition matrix, expressed as

$$\hat{X}_T = [\Phi]\hat{X}_0, \tag{4.16}$$

where $[\Phi]$ is the Floquet transition matrix, $\hat{X}_T$ is the perturbed state vector at time T, and $\hat{X}_0$ is the perturbed state vector at time 0. For simplicity, column matrix Y denoting time-element variables can be inserted in Z as

$$\hat{Z}_T = [\tilde{\Phi}]\hat{Z}_0, \tag{4.17}$$

where

$$\hat{Z}_0 = \lfloor X_0 \, 0 \rfloor^T. \tag{4.18}$$

The effect of Y in the analysis is to produce corresponding eigenvalues with infinity, which can be ignored in Floquet analysis.

The previously described periodic steady-state solution can be used to obtain the Floquet transition matrix. The perturbed form of Eq. (4.9) is

$$J_{i,i-1}\hat{Z}_{i-1} + J_{i,i}\hat{Z}_i = 0 \quad i = 1, 2, \cdots, N, \tag{4.19}$$

where

$$J_{i,i} = \frac{\partial G_i}{\partial \hat{Z}_i}, \tag{4.20}$$

By simple matrix algebra,

$$\hat{Z}_T = [-J_{N,N}^{-1} J_{N,N-1}] \cdots [-J_{1,1}^{-1} J_{1,0}]\hat{Z}_0. \tag{4.21}$$

Therefore,

$$[\tilde{\Phi}] = [-J_{N,N}^{-1} J_{N,N-1}] \cdots [-J_{1,1}^{-1} J_{1,0}]. \tag{4.22}$$

Floquet transition matrix Φ is simply a submatrix of $\tilde{\Phi}$.

Note that the method at this study is equivalent to that in [1]. This means that this procedure is to apply the method in [1] to a specific time integration scheme with the finite element-in-time equation given in Eq. (4.11).

Chapter 5

Numerical Validation

Comparison with ADAMS

The present code has been validated by comparison with results from ADAMS,[TM] a commercially available computer code. (ADAMS was developed by Mechanical Dynamics, Inc.) The ADAMS HAWT model was developed at the National Wind Technology Center (NWTC) of the National Renewable Energy Laboratory (NREL), Golden, Colorado.

CART Model

CART (Controls Advanced Research Turbine) model was developed at NREL; specific information is given in [13]. The CART is a modified Westinghouse model WWG-0600 machine, with a rated power of 600 kW. The rotor is upwind of the tower and consists of two blades and a teetering hub. A diagram of the CART model is shown in Fig. 5.1. This model is composed of a tower, nacelle, high-speed shaft, gear box, low-speed shaft, spindle, and two blades. The tower and the blades are modeled as flexible beams, the high-speed shaft and the spindle are modeled as rigid body, and the lower speed shaft is modeled as a massless flexible body. (Because the shaft is modeled with zero mass, it can be represented as a mechanism to couple rigid bodies together and hence is considered part of the rigid-body subsystem.) Geometric and material properties are presented in Table 5.1. The material properties for tower and blades are presented in [13]. For simplification, the nacelle is assumed to be fixed at the top of the tower.

   The following conditions are specified for running the program. The system is initially at rest, and the gravitational force is neglected. Two external forces excite the system. One is external torque, which is applied to the low-speed shaft. The other is a follower force for the flapping direction at the tip of one blade. Also, all the aerodynamic forces are zero, so the system moves in a vacuum. The time interval is 2 sec, and number of time steps is 400. The number of spatial elements is 20 for the tower, 30 for a blade. The ADAMS model has all the same properties, except that it has 13 stations for the tower and 19 sections for a blade, and internal dampings for numerical stability are given as $C_d = 0.0005C_s$, where C_d is the damping matrix and C_s is the stiffness matrix.

Table 5.1: Physical properties of the CART model

c_n	distance from yaw axis to nacelle mass center	4.02 m
c_s	distance from yaw axis to gearbox	2.519 m
c_h	distance from teeter axis to hub mass center	0.0 m
dn_2	distance from yaw axis to teeter axis	3.867 m
dh_1	distance from teeter axis to blade root	0.0 m
dh_2	distance from shaft axis to blade root	0.688 m
m_y	mass of nacelle	$23,228$ kg
m_s	mass of high-speed shaft	0.0 kg
m_h	mass of spindle	$5,852$ kg
I_{y_1}	moment of inertia of nacelle about lateral axis	3.659×10^7 kg m^2
I_{y_2}	moment of inertia of nacelle about longitudinal axis	1.2×10^7 kg m^2
I_{y_3}	moment of inertia of nacelle about yaw axis	3.659×10^7 kg m^2
$I_{s_{\text{lat}}}$	moment of inertia of high-speed shaft about lateral axis	0.0 kg m^2
$I_{s_{\text{long}}}$	moment of inertia of high-speed shaft about longitudinal axis	34.4 kg m^2
EA_s	axial rigidity of low-speed shaft	1.519×10^{10} N m^2
EI_s	bending rigidity of low-speed shaft	4.776×10^7 N m^2
GJ_s	torsional rigidity of low-speed shaft	1.851×10^7 N m^2
I_{h_1}	moment of inertia of hub about teeter axis	1.5×10^4 kg m^2
I_{h_2}	moment of inertia of hub about shaft axis	0 kg m^2
I_{h_3}	moment of inertia of hub about lateral axis	1.5×10^4 kg m^2
K_h	teeter stiffness	0.0 Nm/rad
C_h	teeter damper coefficient	0.0 Nms/rad
l_b	length of blade	19.995 m
l_t	length of tower	34.862 m
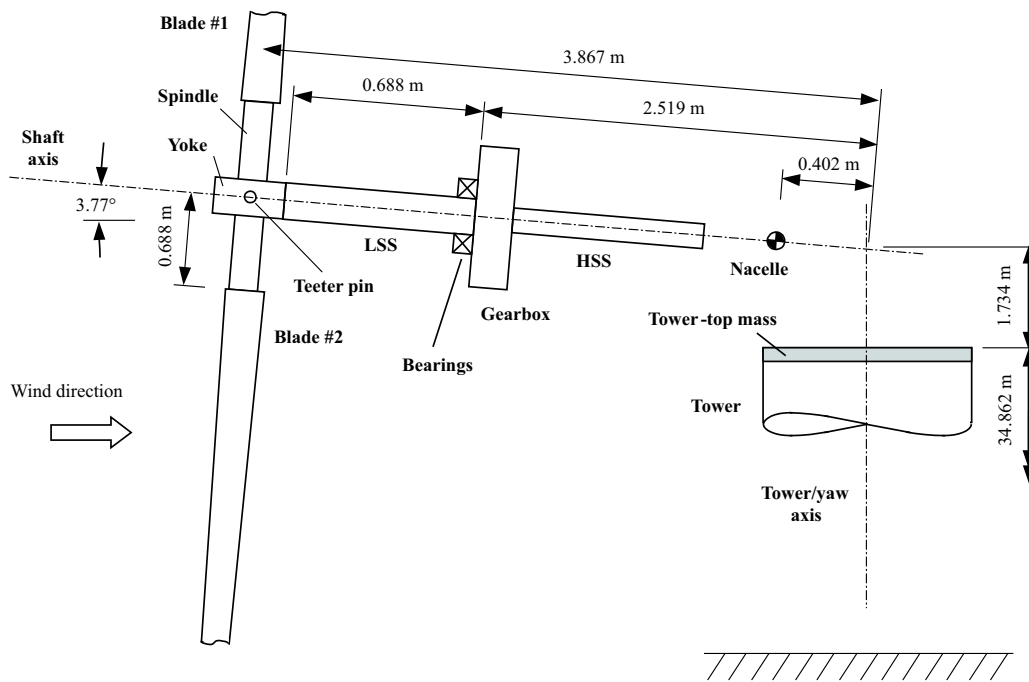
Figure 5.1: CART model: turbine components and dimensions.

Modal Analysis

The most basic measure for deciding whether a computational framework for structural analysis is useful or not is the natural frequency. Natural frequencies from this work are compared with those from experiments, that were done by NREL.

The frequency is taken from the CART model with a nonrotating blade. Also, the nacelle and the hub are fixed at the tower top and at the shaft, respectively. To show the convergence, the number of elements in the tower is 4, 8, 12, 16, 20, and the corresponding number of elements in a blade is 6, 12, 18, 24, 30.

Figures 5.2 through 5.7 show the natural frequencies for the case in which the rotor is vertical. The natural frequencies converge well with those from experimental data, indicated by the dashed line. Also, the convergence rate decreases as the number of elements increases.
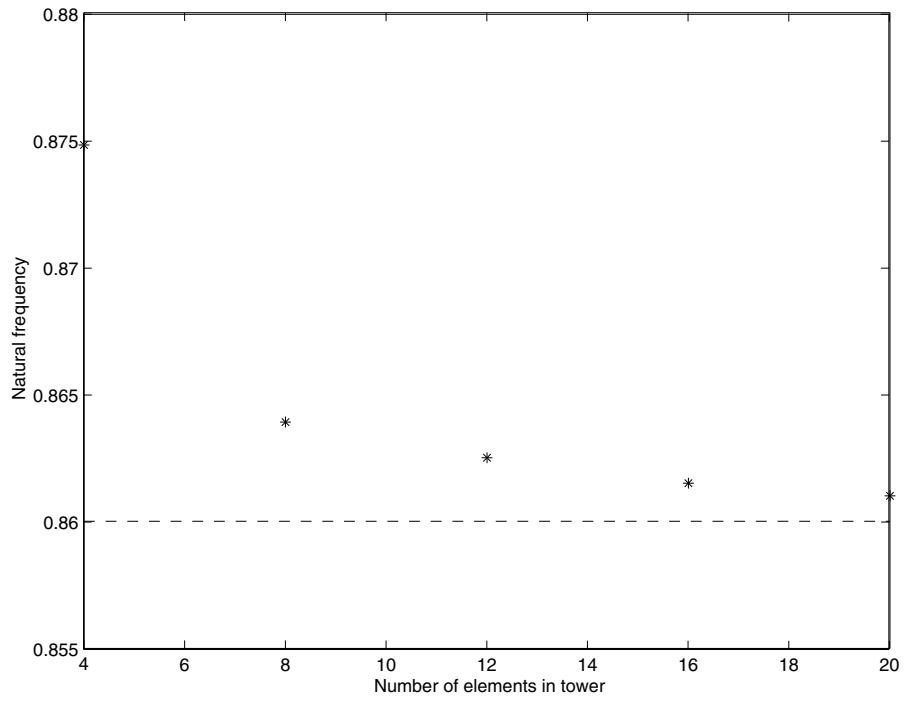
Figure 5.2: 1st natural frequency of CART (vertical)
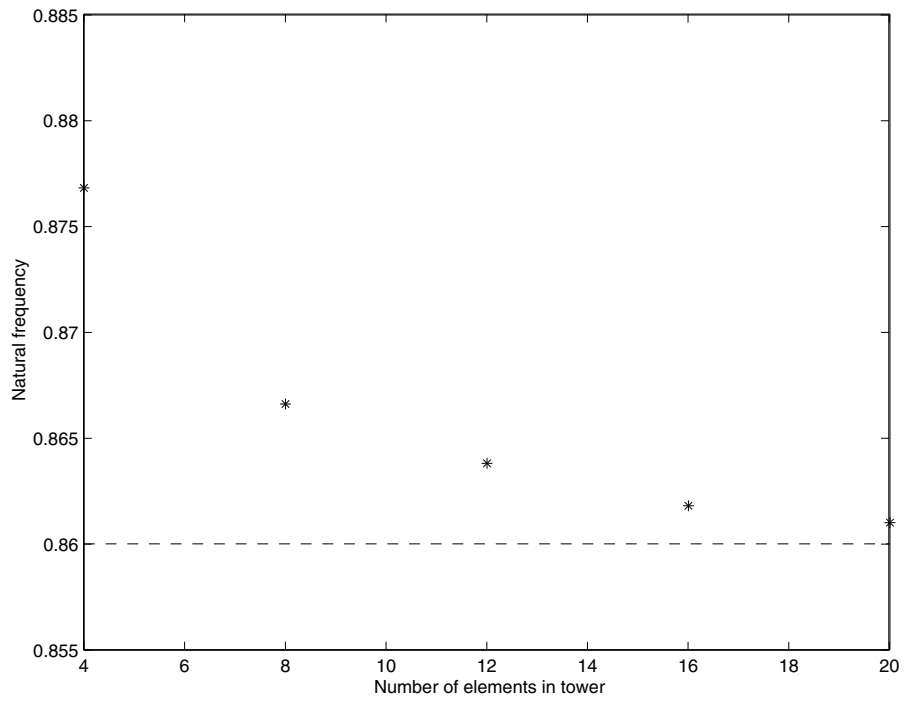
Figure 5.3: 2nd natural frequency of CART (vertical)
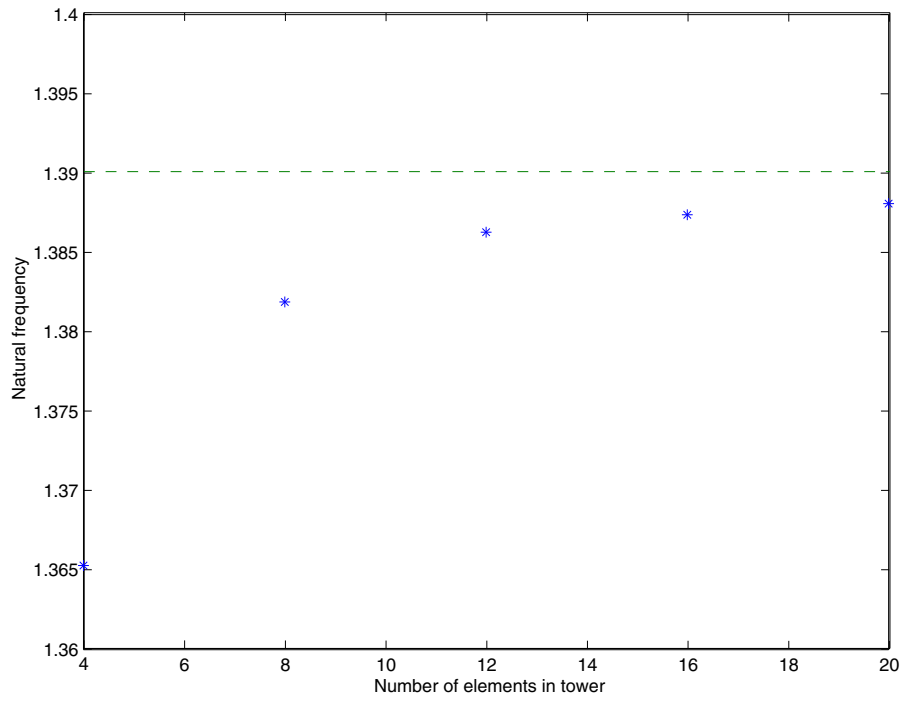
Figure 5.4: 3rd natural frequency of CART (vertical)
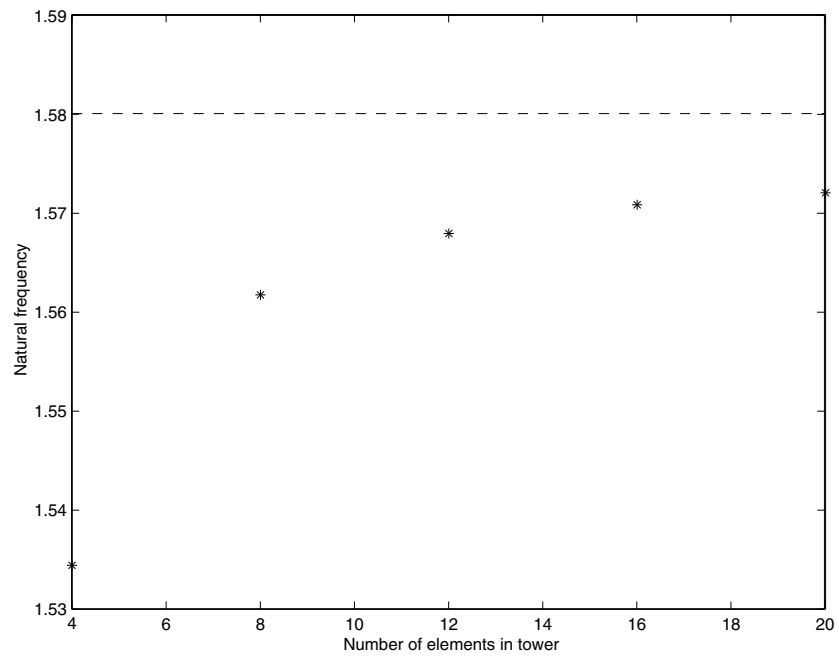
Figure 5.5: 4th natural frequency of CART (vertical)
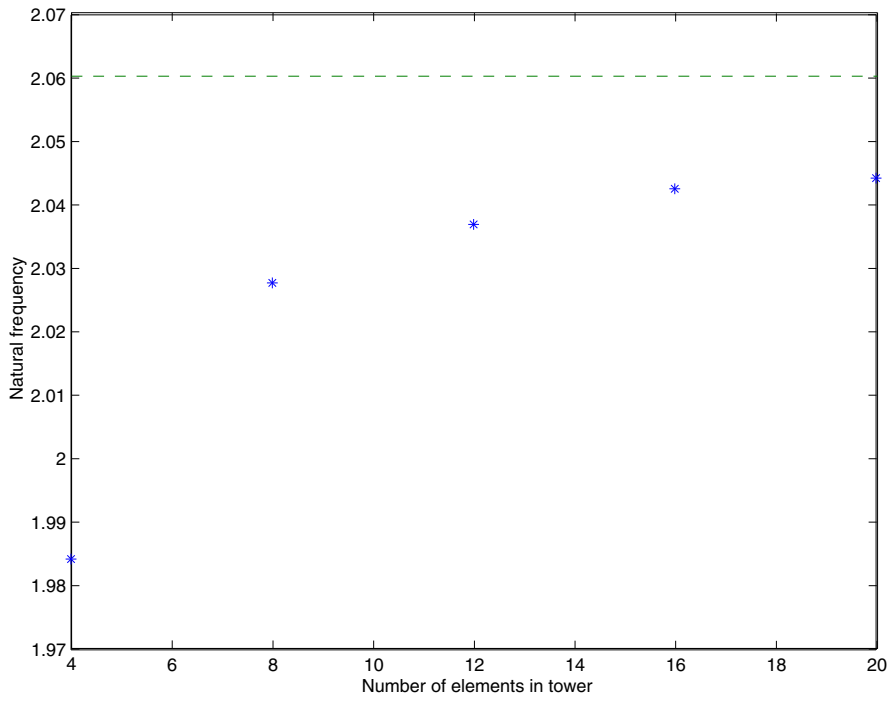
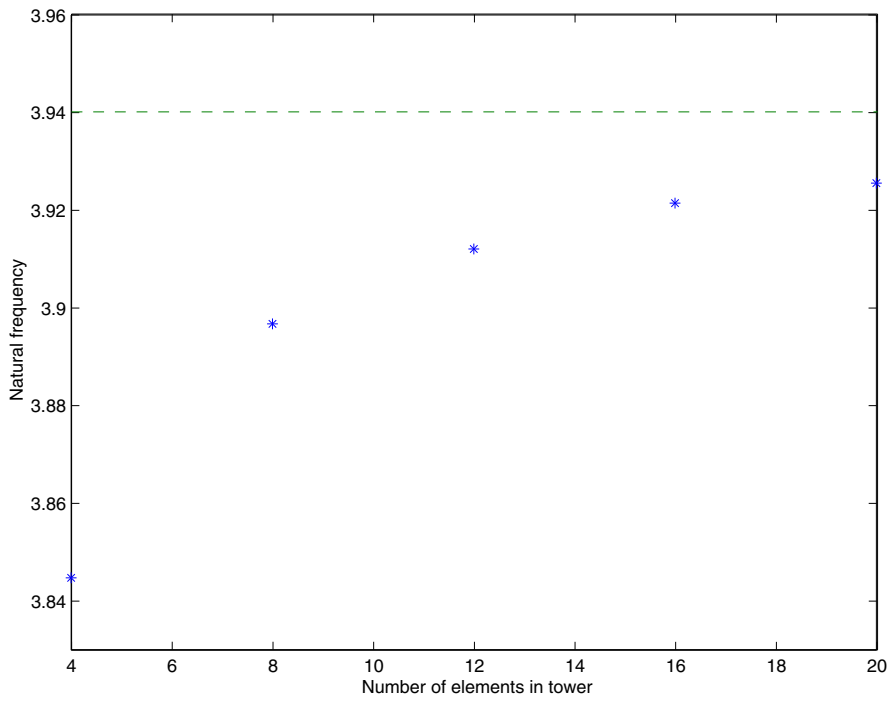Figure 5.6: 5th natural frequency of CART (vertical)

Figure 5.7: 6th natural frequency of CART (vertical)

Figures 5.8 through 5.13 show the natural frequencies for the case in which the rotor is horizontal. As in the vertical rotor cases, the natural frequencies converge well with those from experimental data (dashed line). Also, the convergence rate decreases as the number of elements increases, so it is expected that 8 to 12 elements might be sufficient for a structural analysis of medium numerical accuracy while maintaining the high computational efficiency. Also, the natural frequencies of the isolated blade and the isolated tower converge very well with the experimental data, although they are not presented.
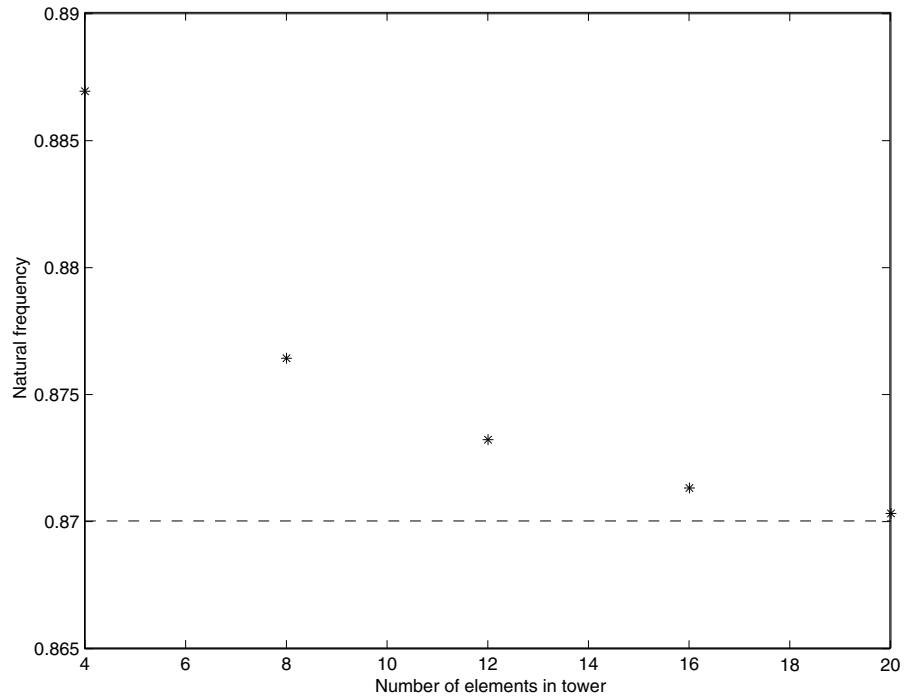
Figure 5.8: 1st natural frequency of CART (horizontal)
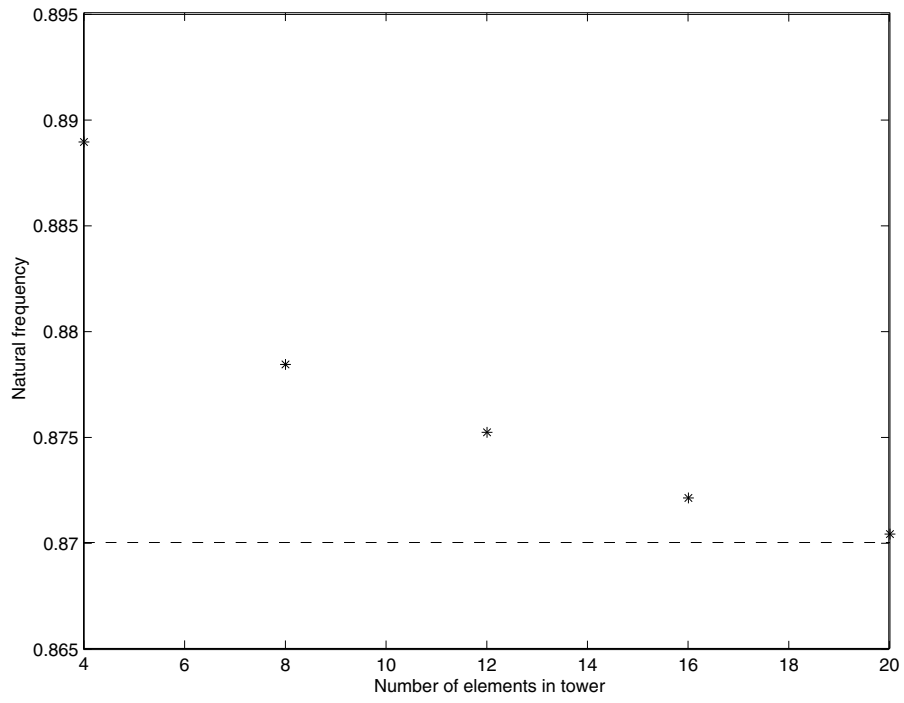
Figure 5.9: 2nd natural frequency of CART (horizontal)
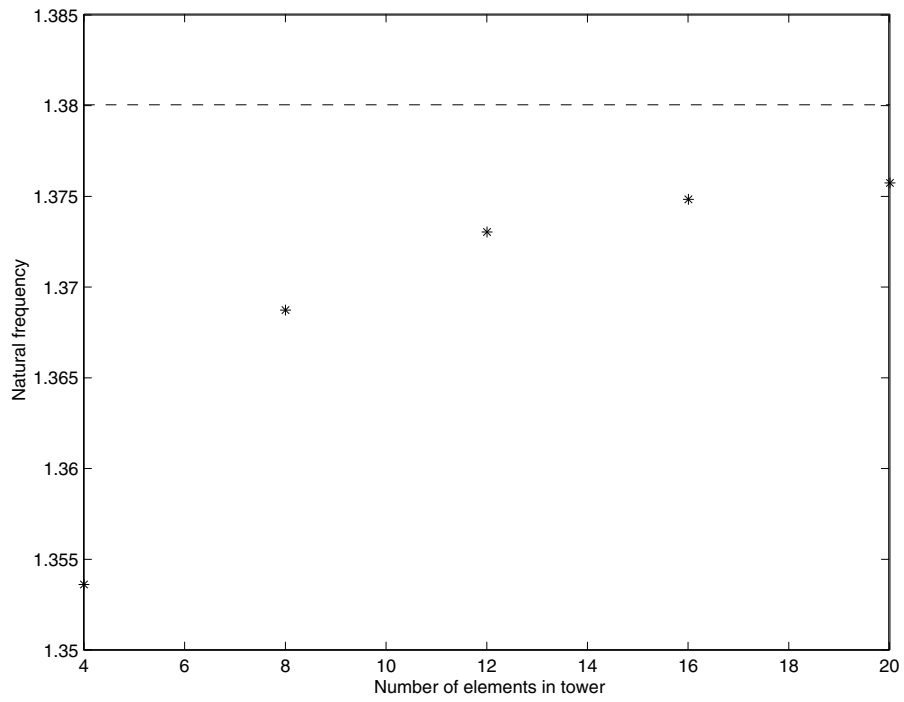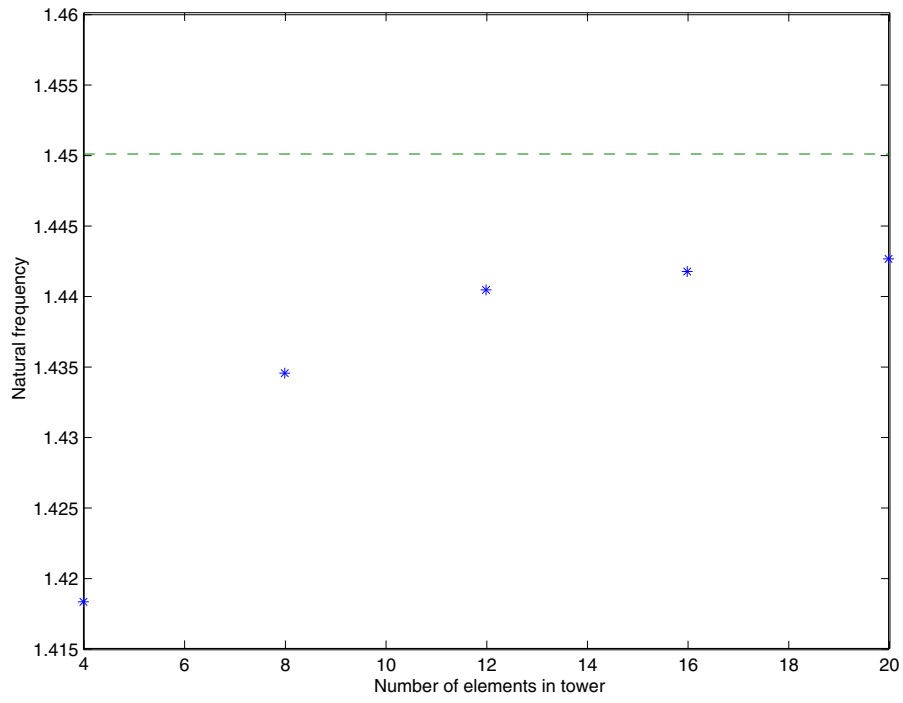

Figure 5.10: 3rd natural frequency of CART (horizontal)

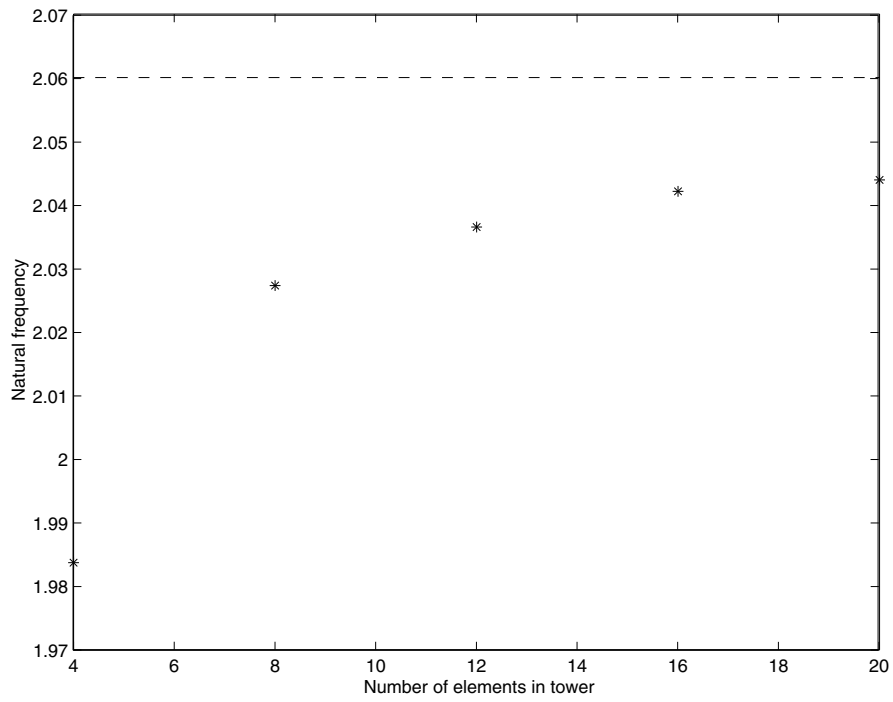Figure 5.11: 4th natural frequency of CART (horizontal)

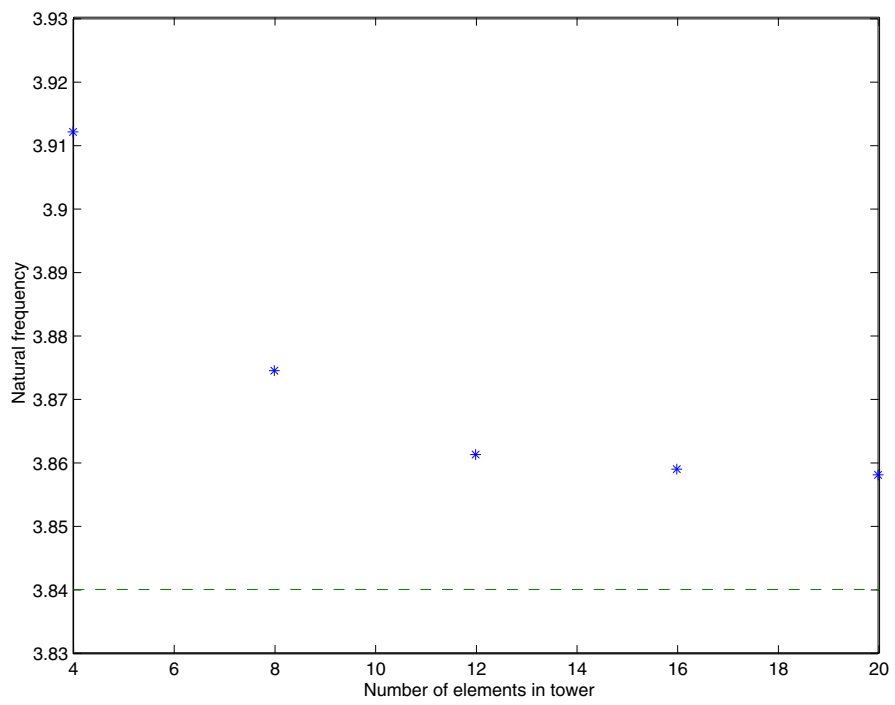Figure 5.12: 5th natural frequency of CART (horizontal)

Figure 5.13: 6th natural frequency of CART (horizontal)

Nonlinear Simulation

To compare results, nine channels are detected from the time history data: rotor azimuth angle, rotor speed, hub teetering angle, displacements of blade tip for 3 directions, and displacements of tower top for 3 directions.

Figure 5.14 through 5.22 show the time history of the nonlinear simulation. In all the graphs, the solid line represents the time history from ADAMS, and the dashed line represents that of this analysis. The results for the teetering angle in Fig. 5.14, the blade tip displacement for the flapping direction in Fig. 5.19, and the tower top displacements in Fig. 5.20 through 5.22 all show the nearly exact match between the results of the two codes. The biggest difference is in the low-speed shaft rotor speed given in Fig. 5.16. Here, the gross motions of two sets of data match well, but there is a local chattering motion in the results of this study; otherwise, the ADAMS results show smooth motion. A possible reason for this chattering motion may be numerical, perhaps caused by the model of the low-speed shaft or the absence of internal damping for numerical stability, such as that modeled in ADAMS, or both. The other graphs show minor differences between the results of the two codes, and they can be explained as the transferring errors from the error in rotor speed. Therefore, we might expect that the code in this study can capture the level of accuracy required by industry.
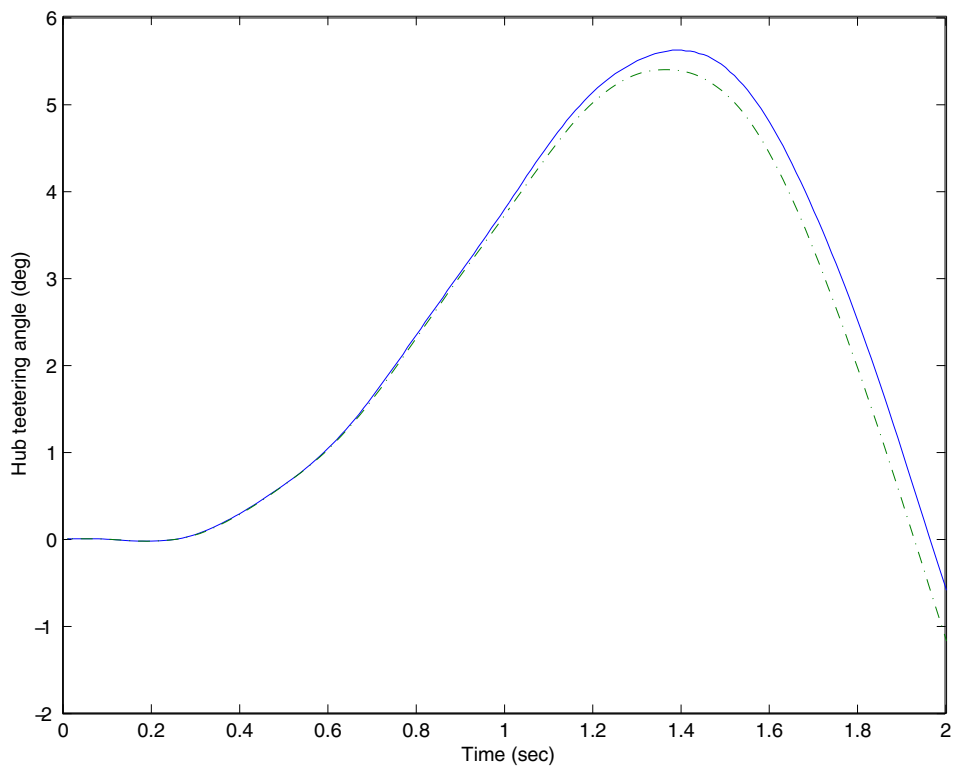
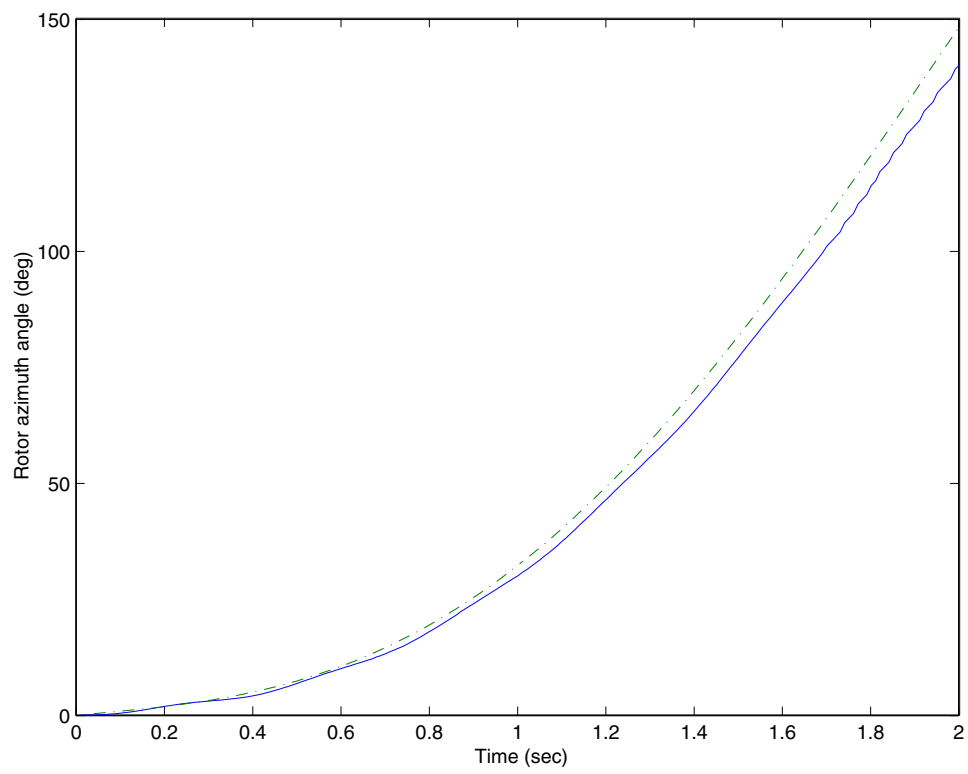Figure 5.14: CART time history – hub teetering angle (deg)

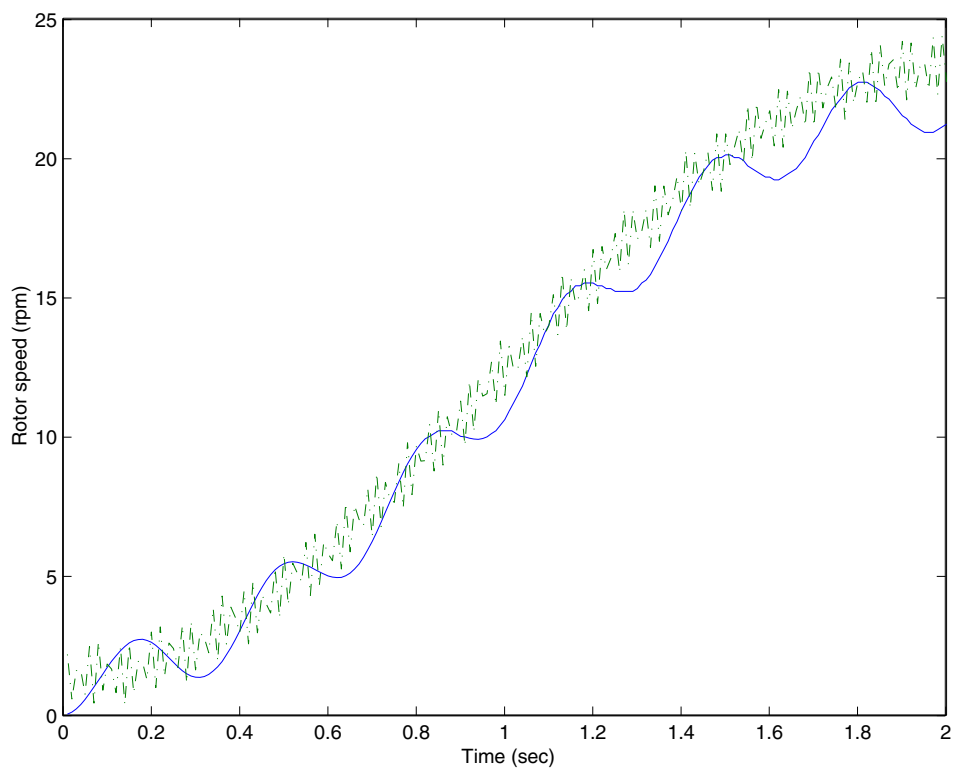Figure 5.15: CART time history – rotor azimuth angle (deg)

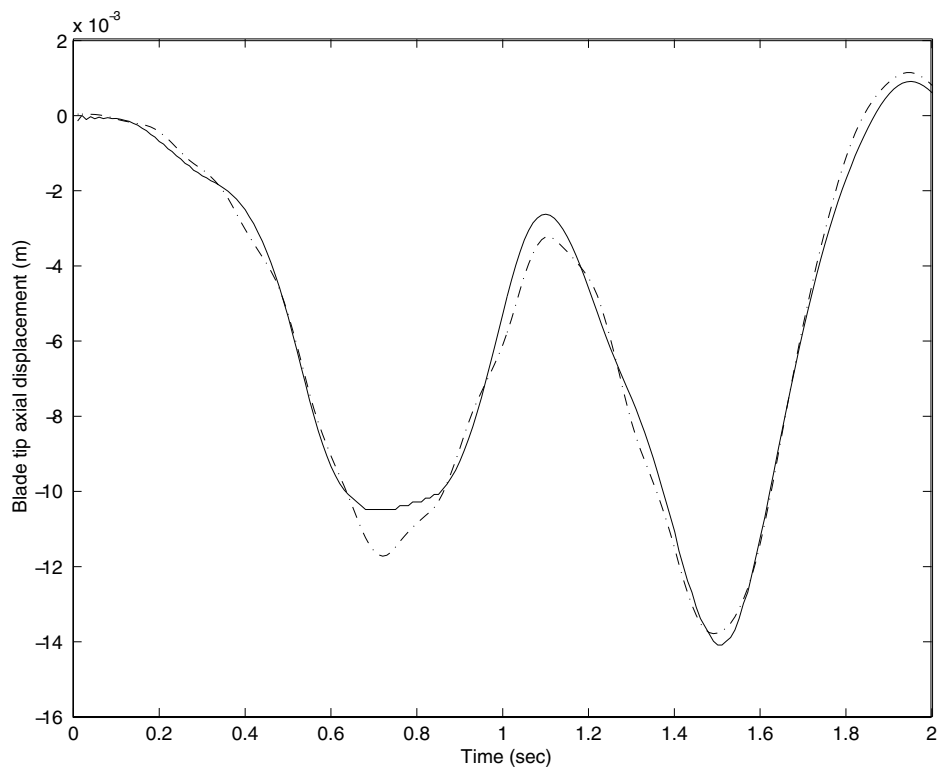Figure 5.16: CART time history – rotor angular speed (rpm)

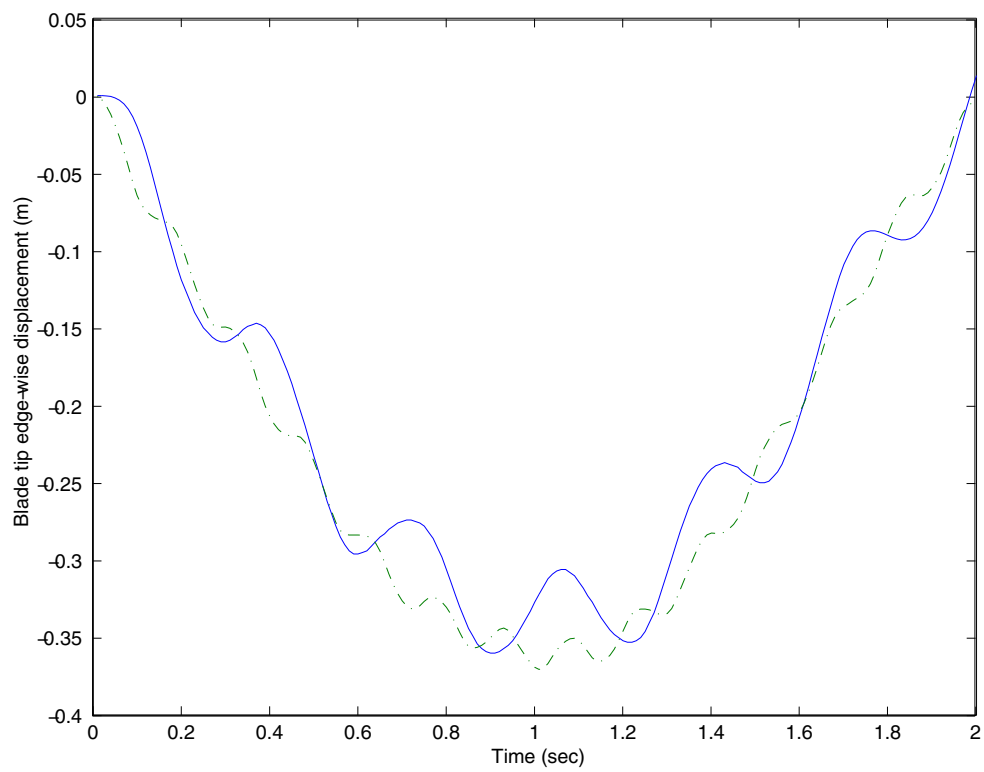Figure 5.17: CART time history – blade tip axial displacement (m)

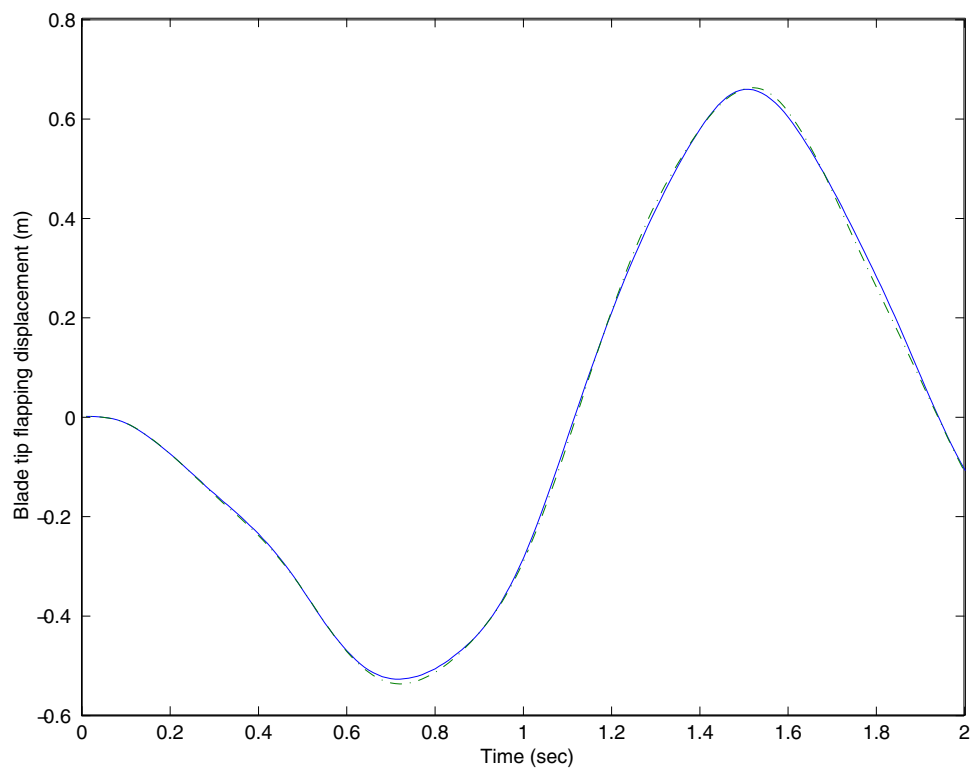Figure 5.18: CART time history – blade tip edge-wise displacement (m)

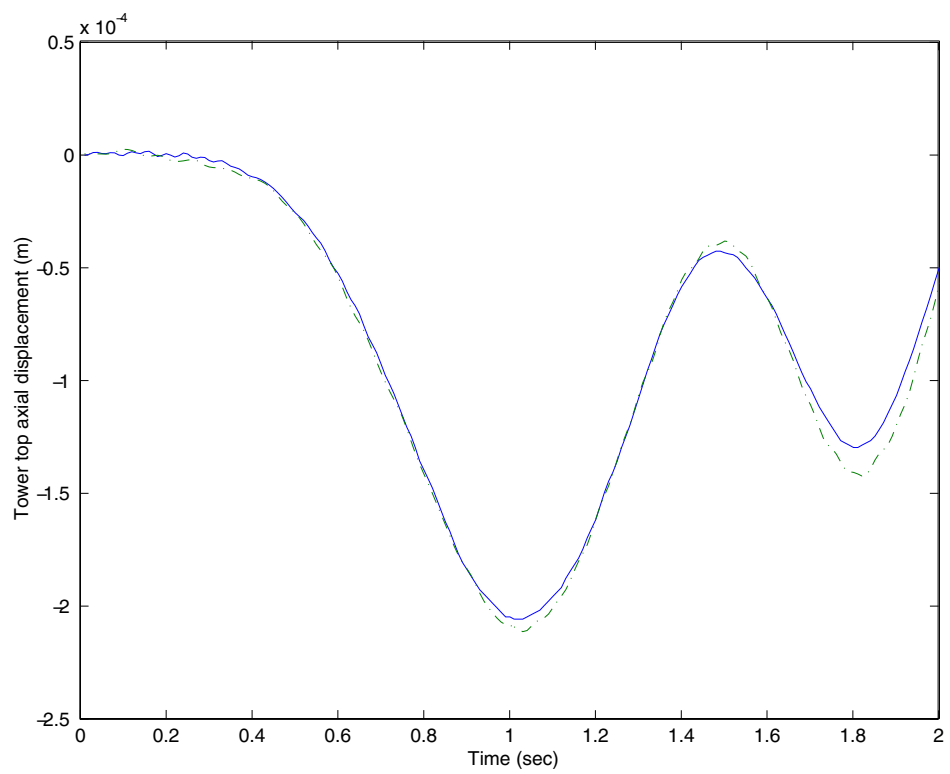Figure 5.19: CART time history – blade tip flapping displacement (m)

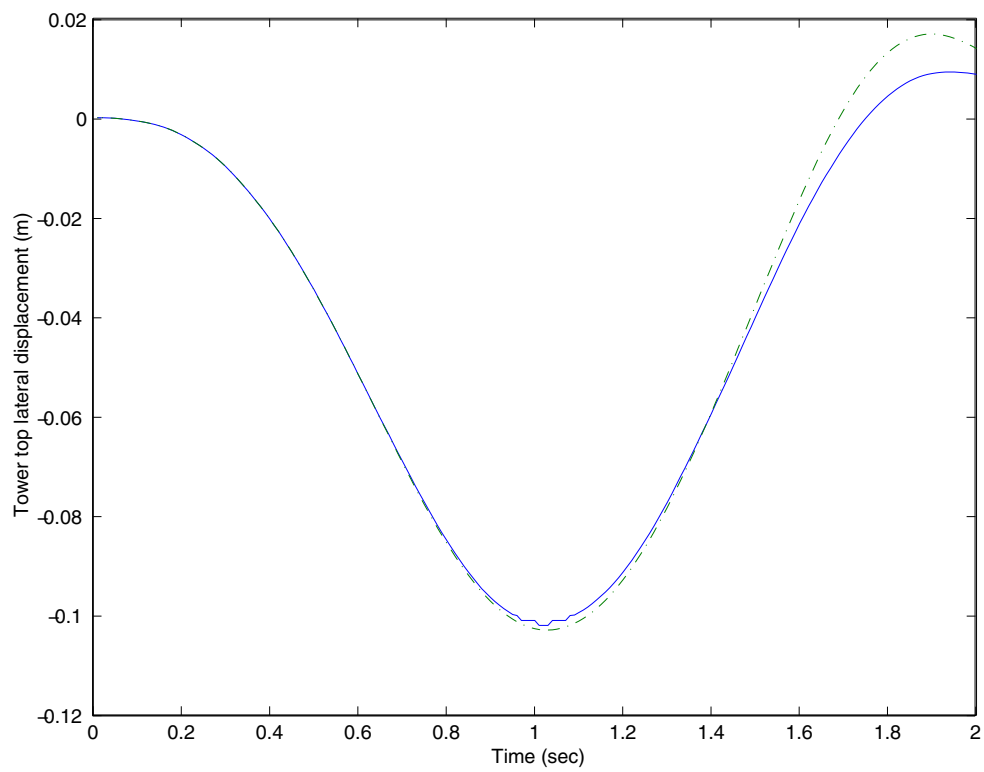Figure 5.20: CART time history – tower top axial displacement (m)

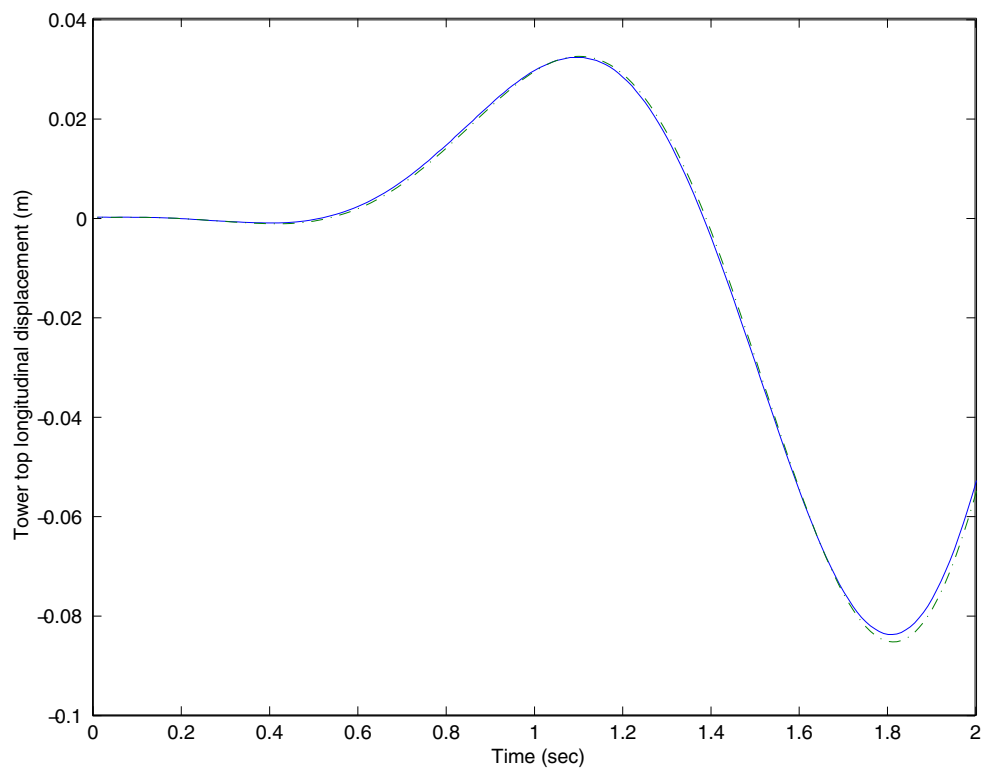Figure 5.21: CART time history – tower top lateral displacement (m)

Figure 5.22: CART time history – tower top longitudinal displacement (m)

Table 5.2: Physical properties of blade spin-up model

length of blade	19.995 m
mass per unit span	149.28 kg/m
cross-sec. mom. of inertia for flapping	29.02 kg m^2/m
cross-sec. mom. of inertia for lead-lag	149.28 kg m^2/m
torsional rigidity	1.29×10^7 N m^2
axial rigidity	2.59×10^9 N m^2
bending rigidity in flapping motion	4.54×10^7 N m^2
bending rigidity in lead-lag motion	2.78×10^8 N m^2

Comparison with DYMORE

Our results in comparison to those of ADAMS are satisfactory, except for the speed of the low speed shaft and the blade lead-lag motion. To investigate the problems more specifically, here the structural model is compared with another highly validated multi-body dynamics code, DYMORE, developed at the Georgia Institute of Technology. The reason to compare with DYMORE is that we could obtain not ADAMS program but ADAMS results.

Blade Spin-up Problem

To investigate the difference in blade lead-lag motion between the results of this study and those of ADAMS, a single blade model with a specified root angular speed is considered. Figure 5.23 is a diagram of the model. The physical properties of the model are presented in Table 5.2. The physical properties are the same as those of the blade parts in the CART model presented in Table 5.1.

Figure 5.24 and 5.25 respectively show the blade tip displacement for the lead-lag direction for root angular speed with sinusoidal functions as

$$\Omega = \frac{2.5}{2}\left[1 - \cos\left(\frac{\pi t}{2}\right)\right]$$
$$\Omega = 2.5\sin\left(\frac{\pi t}{4}\right).$$

(5.1)

The time interval is from 0 to 2 seconds and the number of time steps is 100. The results show that the time histories of the two codes match very well. Also, the local motion with sine input is bigger than that with 1 – cosine input, as expected, because the cumulative impact at the beginning of the time domain of the sine input is larger than that of the 1 – cosine input.

We conclude that the difference in the lead-lag displacement between this study's results and those of ADAMS, given in Fig. 5.18, can be attributed to the differences in conditions other than those of the structural model.

Flexible-Shaft Problem

To investigate the difference in results for the rotor speed of the flexible shaft between this study and ADAMS, a simple rotating system is considered. The system is composed of five components: two flexible
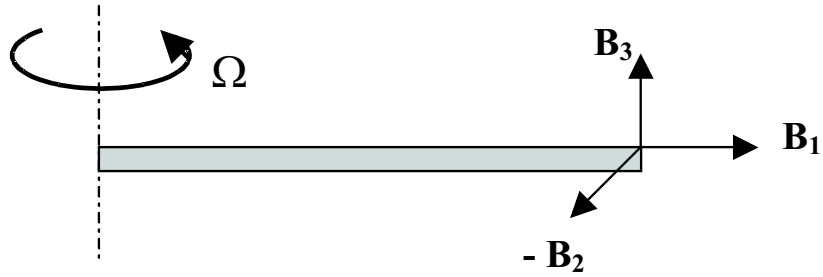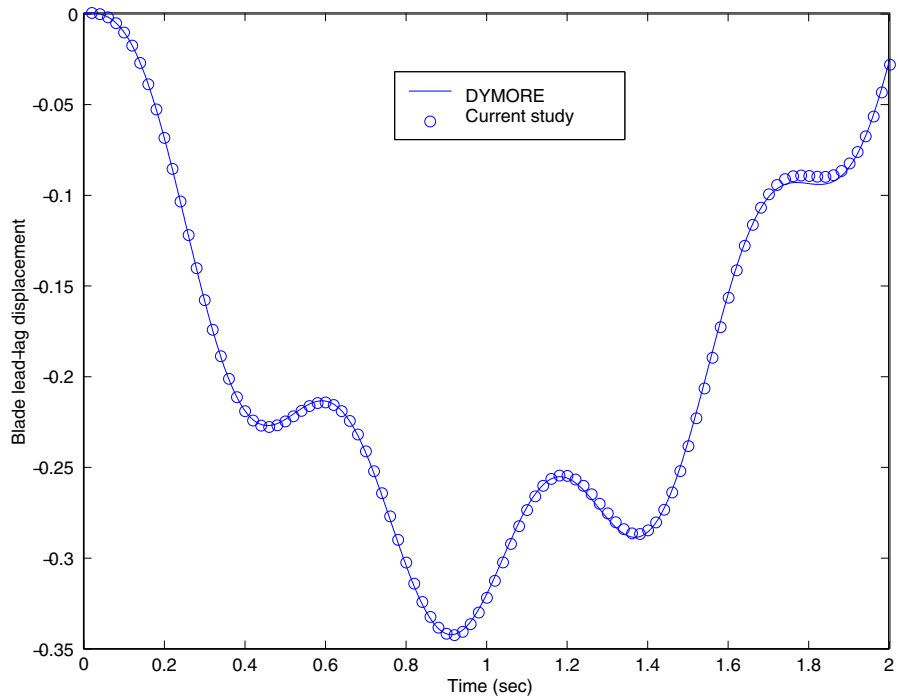
Figure 5.23: Model of blade spin-up problem

Figure 5.24: Time response to 1 – cosine input of blade spin-up model (m)

Table 5.3: Physical properties of flexible-shaft model

mass of hub	5852 kg
mass moment of inertia of hub for H_1 axis	0 kg m^2/m
mass moment of inertia of hub for H_2 axis	15000 kg m^2/m
mass moment of inertia of hub for H_3 axis	15000 kg m^2/m
distance from hub mass center to blade root	1.388 m
length of shaft	1 m
mass per unit span of shaft	3 kg/m
cross-sec. mom. of inertia of shaft for bending	0.25 kg m^2/m
cross-sec. mom. of inertia of shaft for rotating	0.5 kg m^2/m
torsional rigidity of shaft	1.85×10^7 N m^2
axial rigidity of shaft	1.52×10^10 N m^2
bending rigidity of shaft	5.89×10^9 N m^2
point mass at root of shaft	1000 kg
teeter stiffness	0 Nm/rad
teeter damping	0 Nm/rad

blades, a rigid hub, a flexible shaft, and a point inertia. The blades are clamped to the hub, which is teetering with respect to the shaft about the H_2 axis. The point inertia is located at the root of the shaft.

Figure 5.26 shows a diagram of the model. The physical properties of the blade are the same as those given in Table 5.2. The physical properties of the other components are given in Table 5.3. The applied torque is given as

$$T = 2.1 \times 10^6 \sin\left(\frac{\pi t}{2}\right). \tag{5.2}$$

Figure 5.27 shows the time history of the rotor speed taken from the current study. There is local oscillation over the whole time interval. But the local motion can be removed by a filtering process:

$$\bar{X}_i = \frac{(X_{i+1} + X_i)}{2} \quad i = 1, 2, \cdots, N-1, \tag{5.3}$$

where $\bar{X}_i$ denotes the filtered time history, X_i denotes the original time history, and N is the total number of time steps.

Figure 5.28 presents the filtered time history of the rotor speed compared with the result from DYMORE, showing that the rotor speed from the two codes match well. The results both for blade tip edge-wise and flapping displacement also match well those from DYMORE, as shown in Fig. 5.29 and Fig. 5.30. Our results for the frequencies of the blade tip edge-wise displacement from the present work are about same as those from DYMORE, which differ from those of ADAMS as shown in Fig. 5.18.

Figure 5.31 shows the log convergence of our study results to the reference value from DYMORE, with a much larger number of time and space elements. The results show that the convergence matches with typical trends for convergence study. In Fig. 5.31, x is the maximum value of the blade tip edge-wise displacement from our study, x_e is the corresponding reference value from DYMORE with an extremely large number of elements, and N_s is the number of spatial elements in our current study. Therefore, we conclude that the structural model of this study is successfully validated by comparison with ADAMS and DYMORE results.
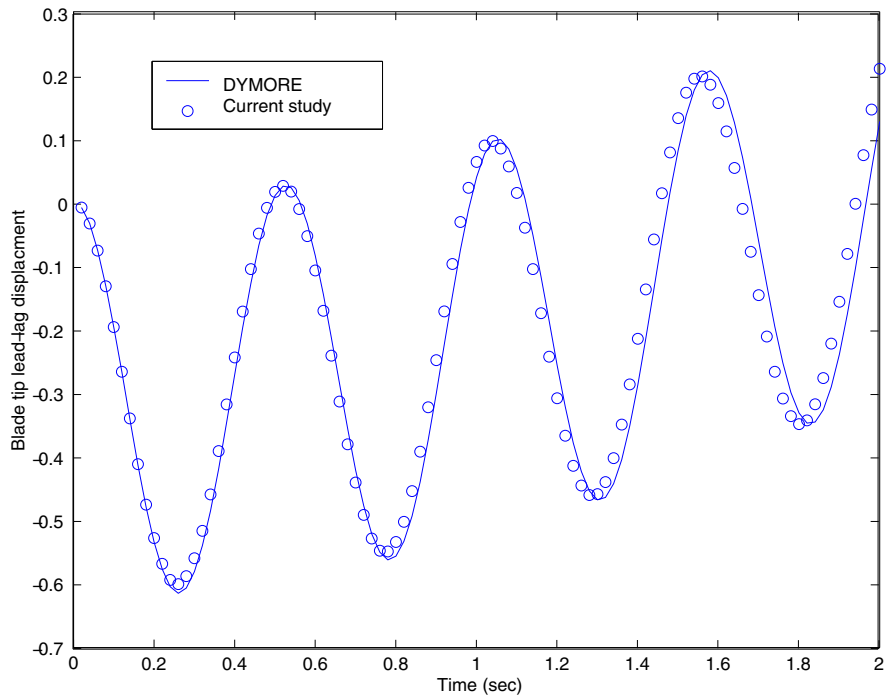
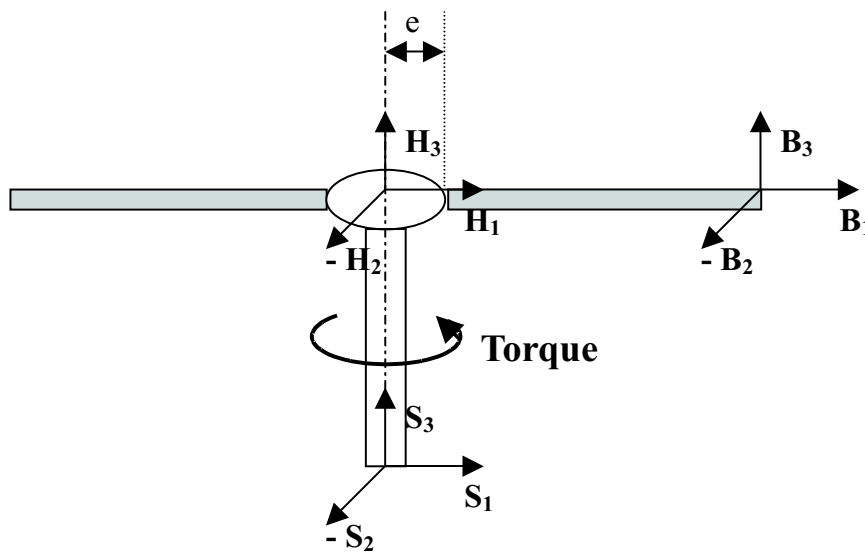Figure 5.25: Time response to sine input of blade spin-up model (m)

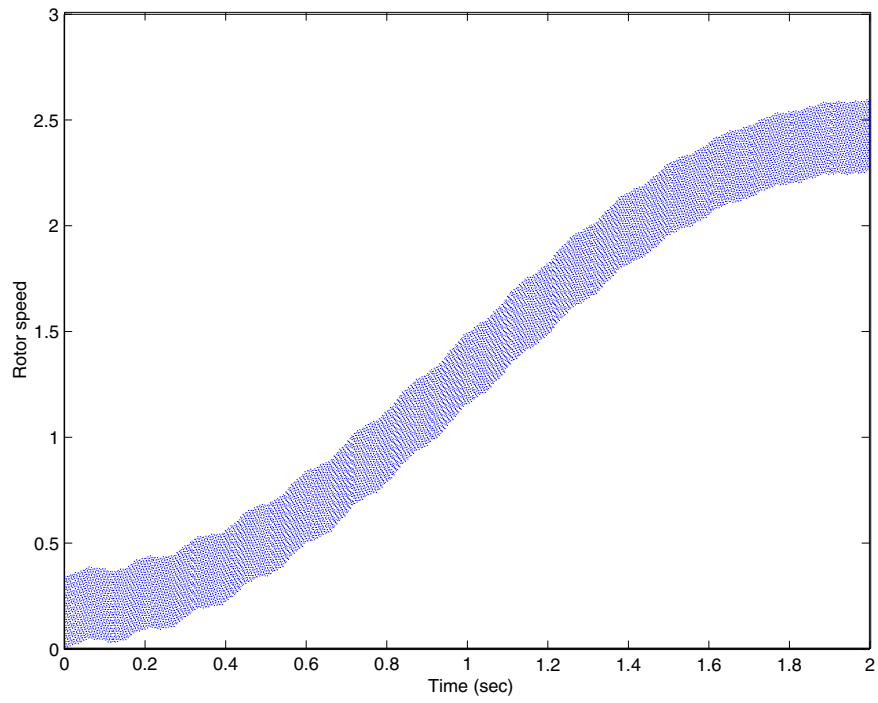Figure 5.26: Model of flexible-shaft problem

Figure 5.27: Rotor speed of flexible-shaft problem without filtering process (rad/s)
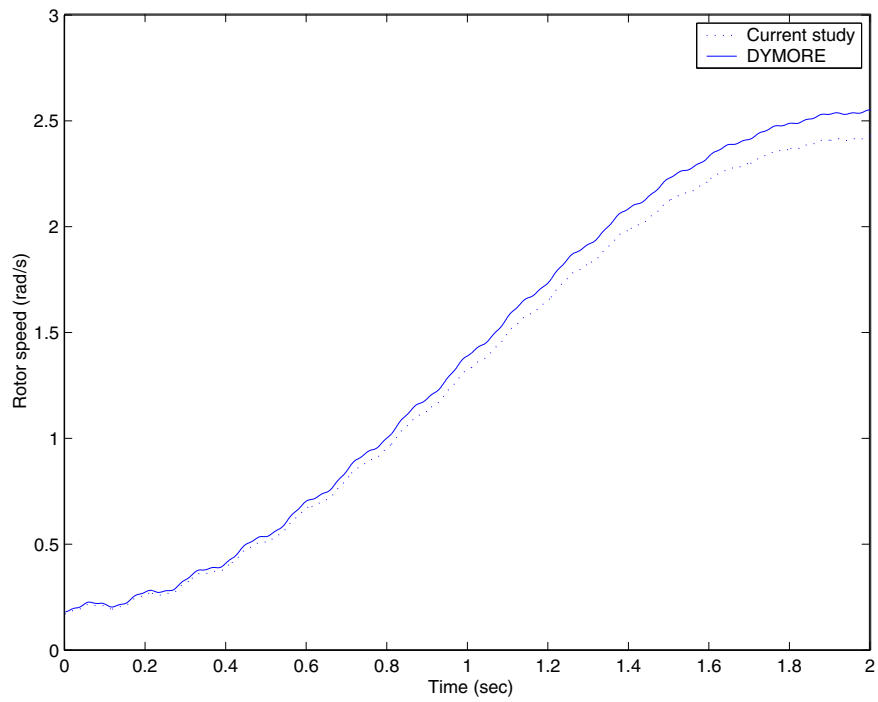

Figure 5.28: Rotor speed of flexible-shaft problem compared with DYMORE (rad/s)
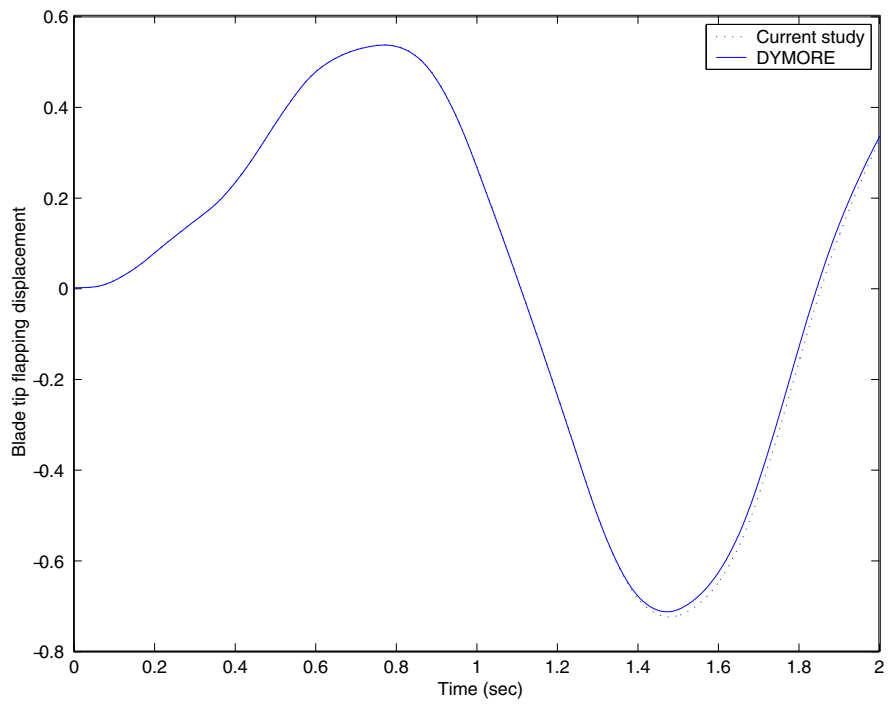
Figure 5.29: Blade tip flapping displacement of flexible-shaft problem compared with DYMORE results (m)
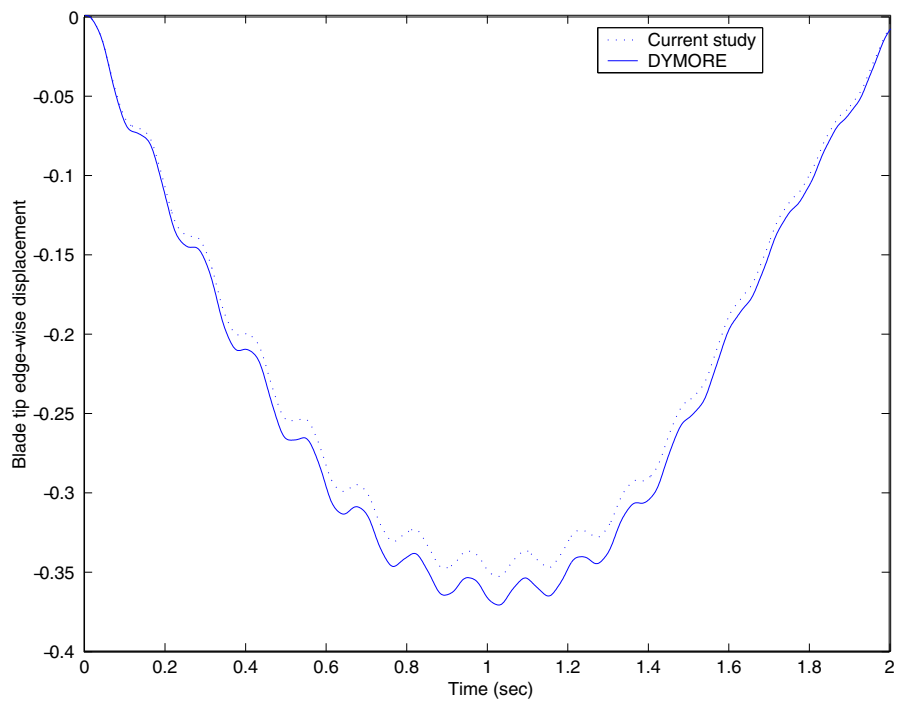
Figure 5.30: Blade tip edge-wise displacement of flexible-shaft problem compared with DYMORE results (m)
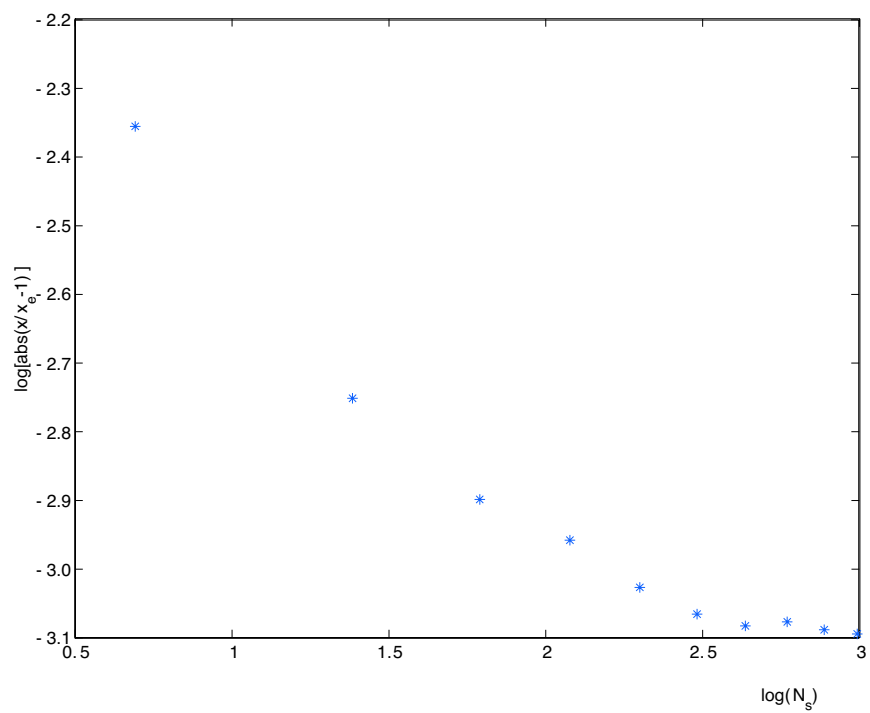
Figure 5.31: Convergence of our results to the DYMORE result for the flexible-shaft problem

Table 5.4: Physical properties of CART model

d_h	longitudinal distance from hub mass center to blade root	0 m
Ω_0	nominal rotor speed	1.4π rad/s
β	precone angle	0 rad
K_h	teeter stiffness	10^5 Nm/rad
C_h	teeter damper coefficient	10^5 Nms/rad
K_y	yaw stiffness	10^5 Nm/rad
C_y	yaw damper coefficient	10^5 Nms/rad

Convergence Study

To validate the accuracy of this code to calculate the periodic steady-state, a convergence study was performed. The model is based on the CART model, its properties are given in Table 5.1. The result in Fig. 5.16 shows the rotor speed to be chattering. To avoid any possible negative influence of this chattering when calculating the periodic steady-state, we use a rigid shaft model. Additional or different properties from those in shown Table 5.1 are given in Table 5.4.

Figures 5.32–5.34 show the periodic steady-state response of the teetering angle, blade tip edge-wise displacement, and tower top fore-aft displacement with the change in the number of time elements. All the results converge well as the number of time elements increases from 10 to 40 per period. Here, the number of space elements is 4 for each blade and tower.

Figures 5.35–5.37 show the periodic steady-state response of the teetering angle, blade tip edge-wise displacement, and tower top fore-aft displacement with the change of the number of the space elements. Similarly to the convergence with a change in the number of time elements, all the results converge well as the number of space elements increases from 2 to 8 in one blade. But the convergent speed in the tower top fore-aft displacement is slower than in the other cases. Here, the number of time elements is 40 per one period.

From the convergence study, it appears that quite a few elements are needed in order for the periodic steady-state solution to convergence. The convergence of the corresponding Floquet results from the linearized model, however, may or may not be consistent to that of the periodic steady-state solution. a model with minimal states may not be sufficiently accurate for control design without some tweaking (such as adjusting the stiffnesses to give agreement between the linearized model and lower-frequency results from a high-fidelity model). Another possibility is to undertake additional research to develop a suitable modal reduction scheme.

Figure 5.32: Periodic steady-state solution – hub teetering angle (rad) with the change in the number of the time elements

Figure 5.33: Periodic steady-state solution – blade tip edge-wise displacement (m) with the change in the number of the time elements

Figure 5.34: Periodic steady-state solution – tower top fore-aft displacement (m) with the change in the number of the time elements
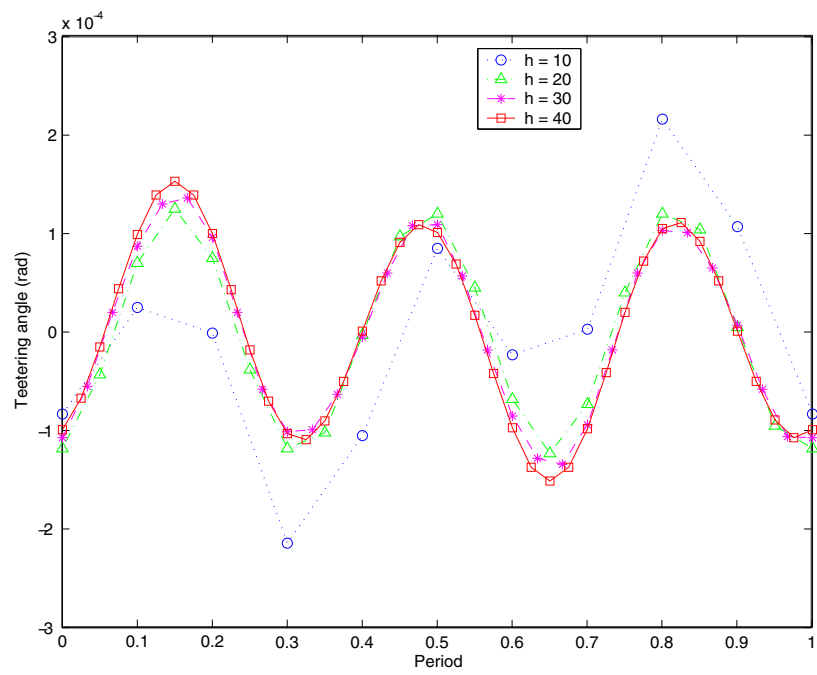
Figure 5.35: Periodic steady-state solution – hub teetering angle (rad) with the change in the number of the space elements
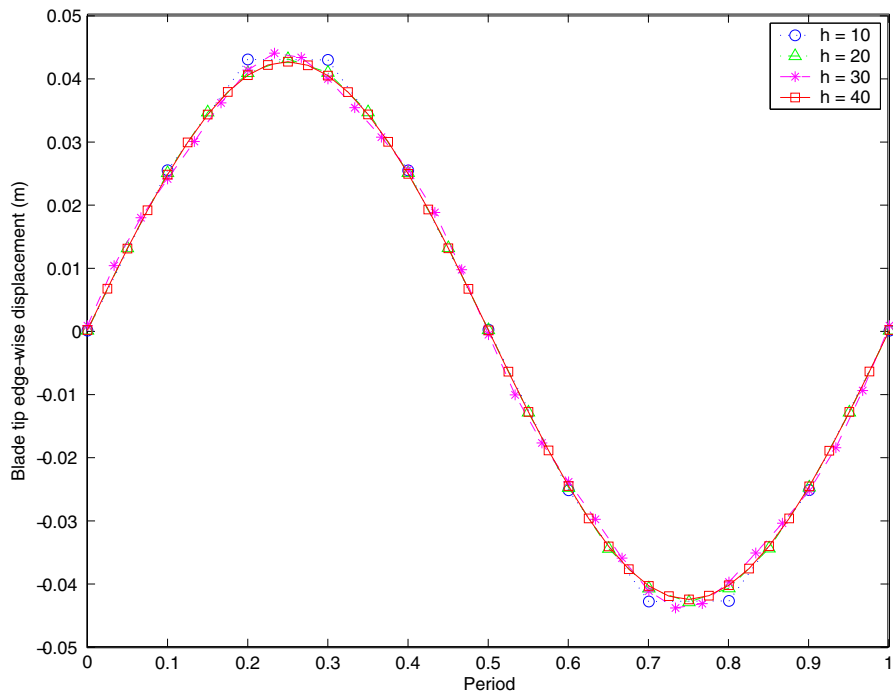
Figure 5.36: Periodic steady-state solution – blade tip edge-wise displacement (m) with the change in the number of the space elements
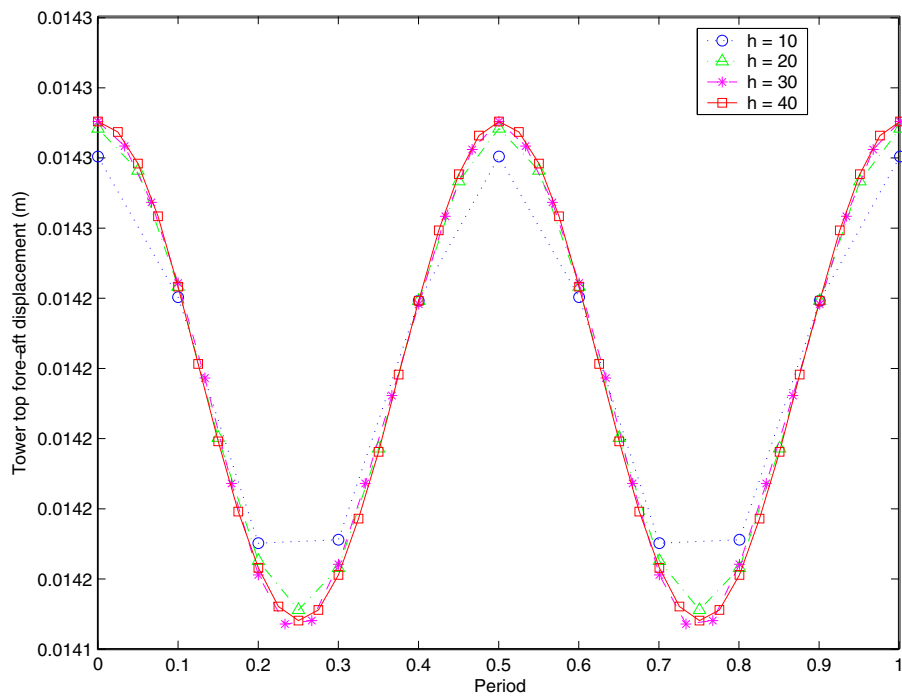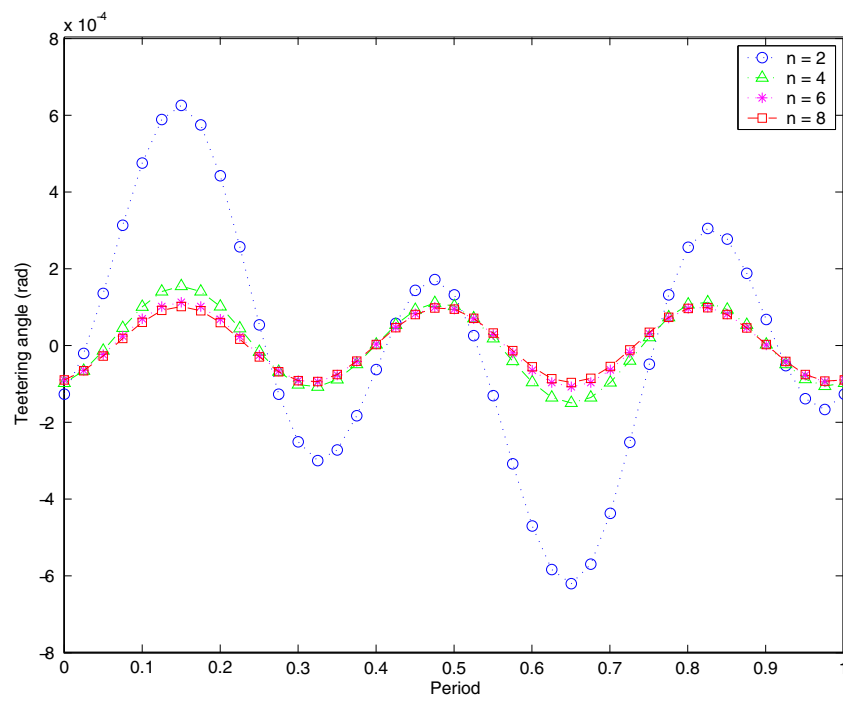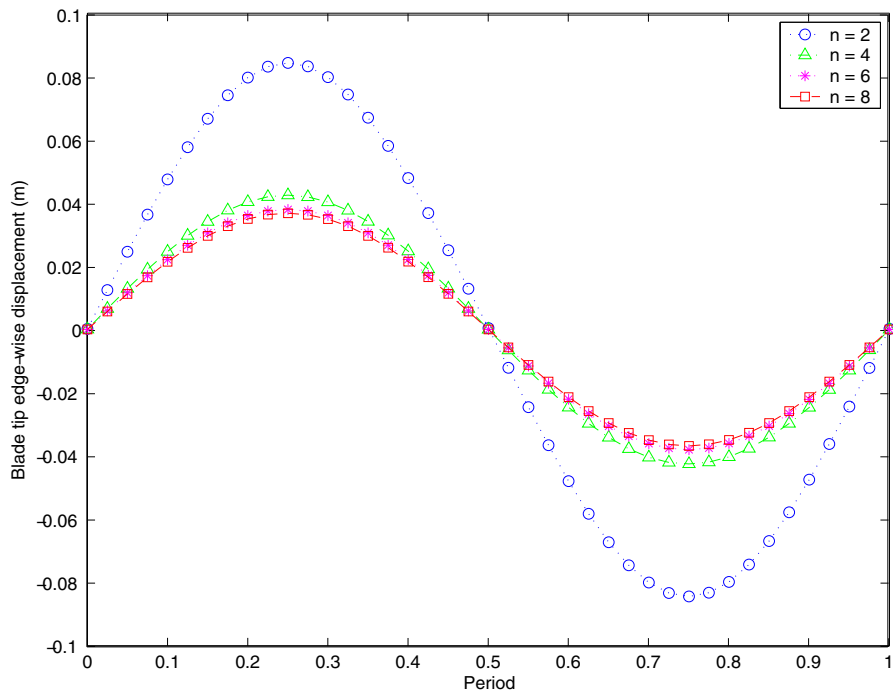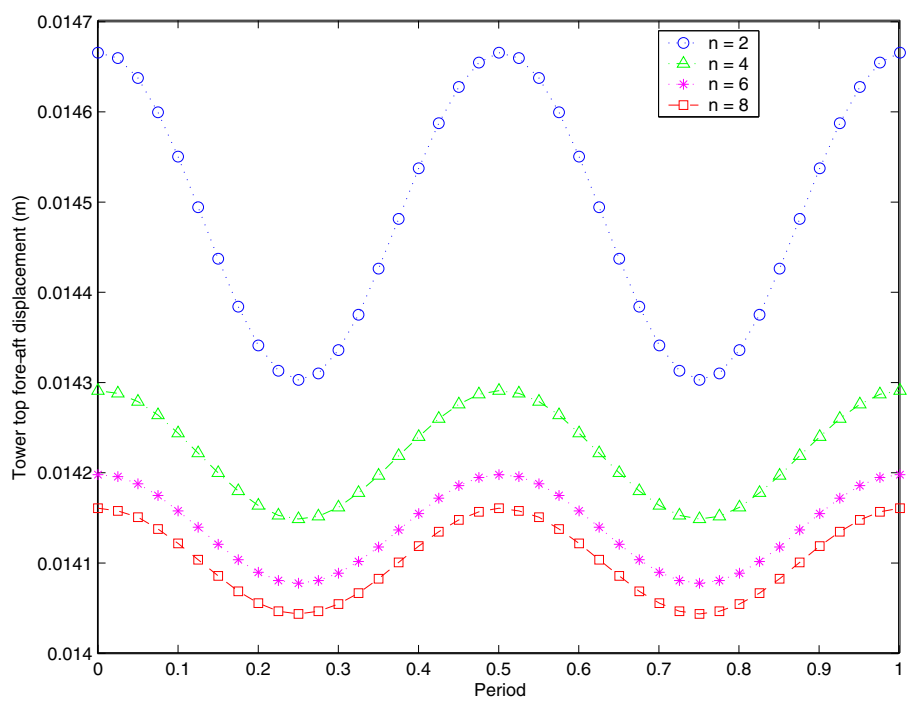
Figure 5.37: Periodic steady-state solution – tower top fore-aft displacement (m) with the change in the the number of the space elements

Chapter 6

CART Dynamic Analysis

A stability analysis of a wind turbine is presented in this chapter; it is based on the computational framework developed in Chapter 4. The model is the same as that for the convergence study described in Chapter 5. The number of space elements in the tower and the blade is 4, and the number of time elements is 40 in a period. To investigate the Floquet stability, we present the trend of the maximum real part of the stability components with respect to various parameters.

Effect of Precone Angle

Figure 6.1 shows that the steady-state response of the hub teetering angle has a symmetric mirror image with the change of the sign in the precone angle, or it could be explained by the shift in the phase at $180°$. The sign change in the precone angle does not much change the shape of the graph shown in Fig. 6.2, but it causes a shift in the amplitude as well as in the phase of the blade tip flapping displacement, as shown in Fig. 6.3. The amplitude of the tower top fore-aft displacement is shifted with the change of the precone angle, as shown in Fig. 6.4.

Figure 6.5 shows the trend of the log of the instability measure versus the precone angle. The instability measure slightly increases as precone varies from $-10°$ to $0°$ and stiffly increases as precone varies from $0°$ to $10°$. Note that the possibility always exists for some of the instabilities to be numerical as opposed to physical. This issue is initially explored below but should be further investigated in future research.

Effect of Rotor Speed

Figure 6.6 shows the amplitude of the steady-state response of the hub teetering angle increases as the rotor speed increases; the shape of the function for high-speed cases is not a simple harmonic function. The blade tip edge-wise displacement, shown in Fig. 6.7, also has the maximum amplitude for the case with the highest rotor speed; but the shape of the function is simple, and the frequency content of the shape is the same. Figure 6.8 shows that the increase in amplitude is most dramatic in tower top fore-aft displacement. Figure 6.9 shows that instability measure increases, as the rotor speed increases.
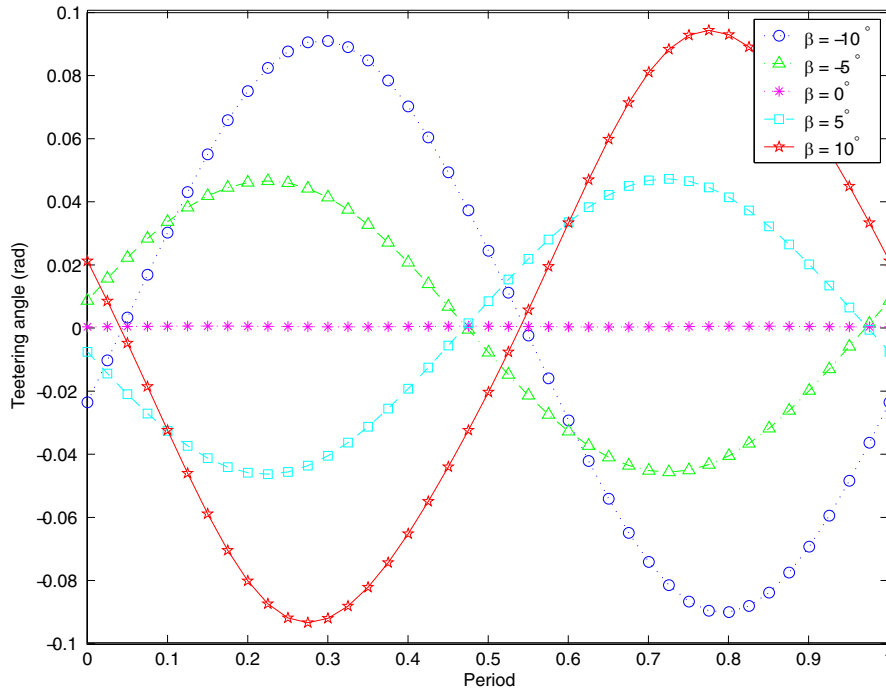
Figure 6.1: Periodic steady-state solution – hub teetering angle (rad) with changes in precone angle

Effect of Teetering Stiffness and Damping

Figure. 6.10 shows that the amplitude of the steady-state response of the hub teetering angle decreases as the teetering stiffness and damping increase. The results in the blade tip edgewise displacement and tower top fore-aft displacement are very similar with changes of stiffness and damping as shown in Fig. 6.11 and Fig. 6.12, respectively.

Figure 6.13 shows that the instability measure is maximum in the case $K_h = C_h = 10^5$, and Fig. 6.14 shows the results near the maximum point with high resolution.

Figure 6.2: Periodic steady-state solution – blade tip edge-wise displacement (m) with changes in precone angle
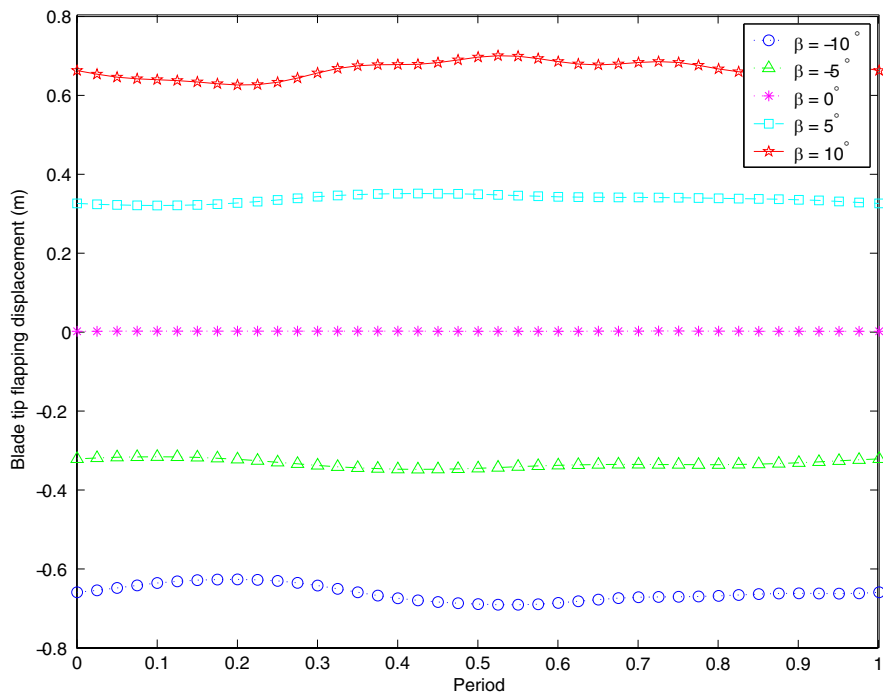
Figure 6.3: Periodic steady-state solution – blade tip flapping displacement (m) with changes in precone angle
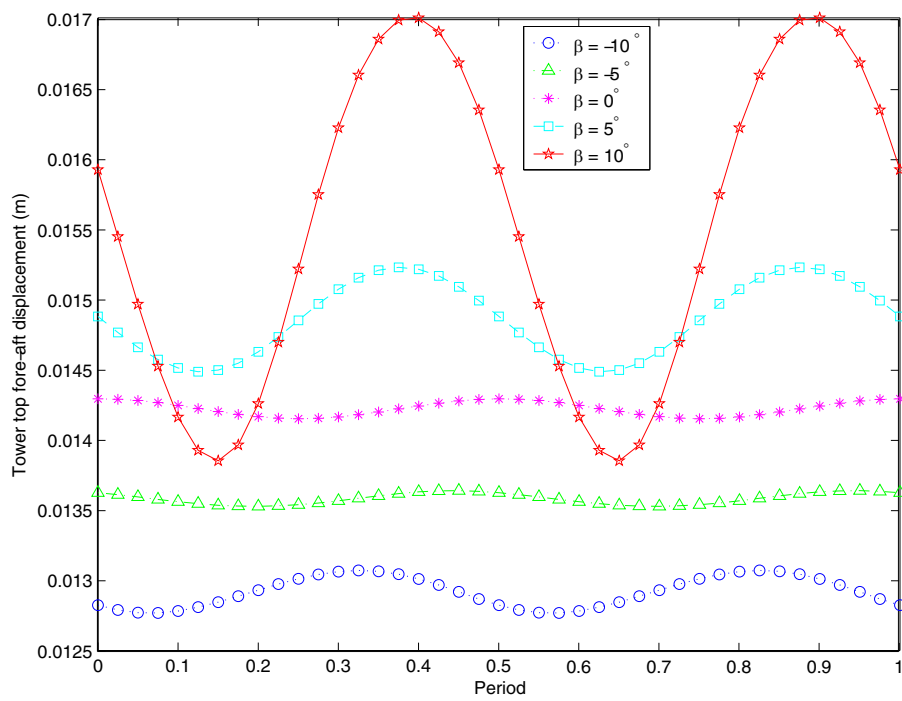
Figure 6.4: Periodic steady-state solution – tower top fore-aft displacement (m) with changes in precone angle
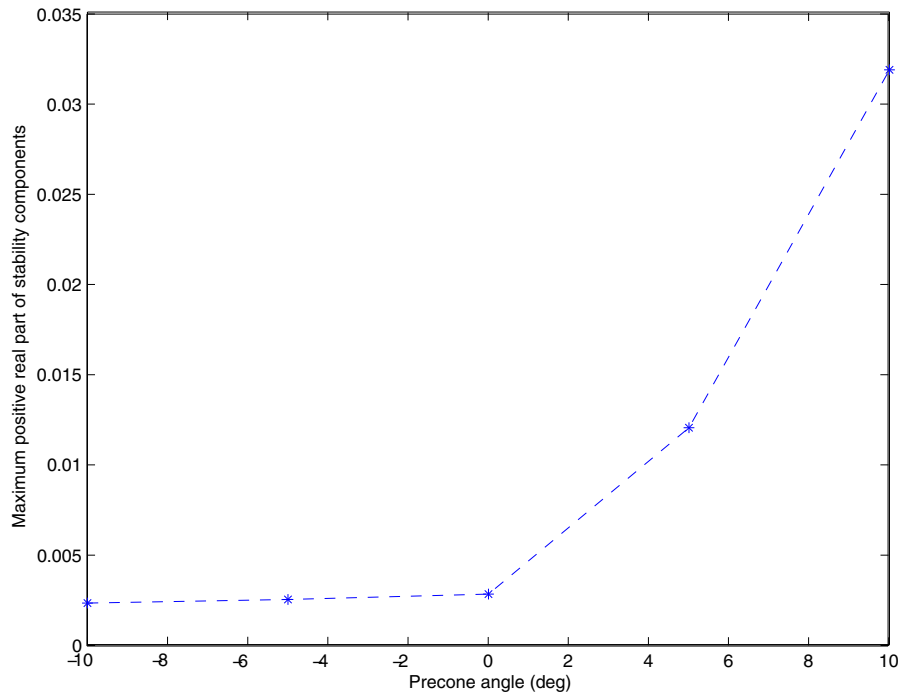
Figure 6.5: Maximum real part of Floquet stability components with changes in precone angle

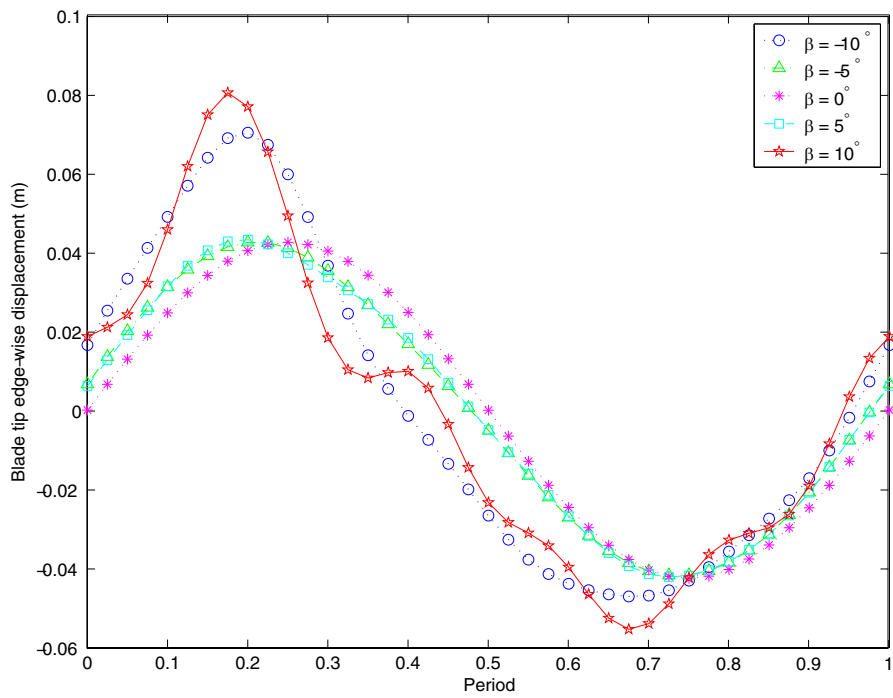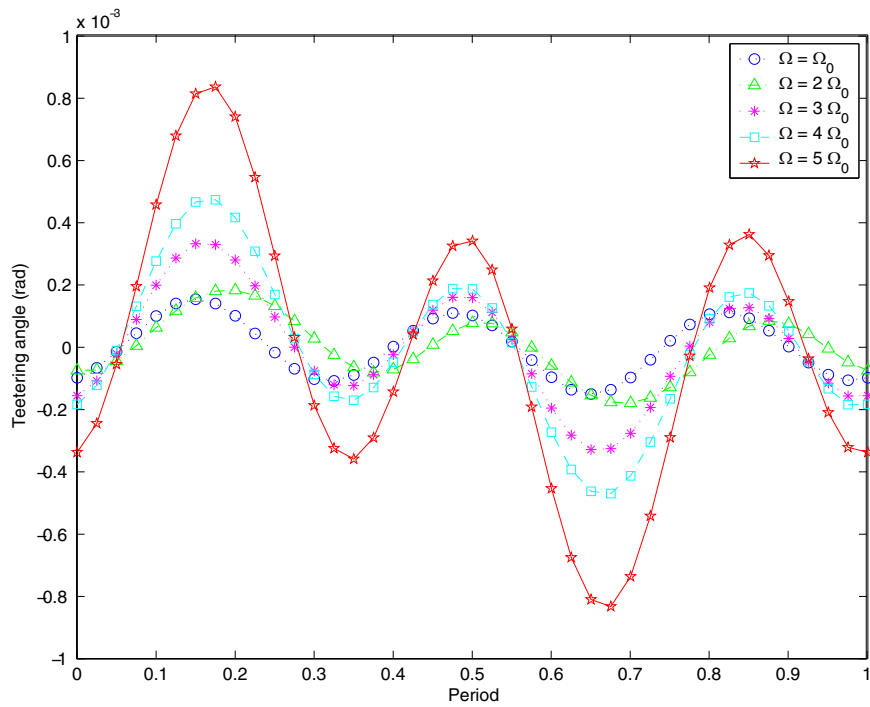Figure 6.6: Periodic steady-state solution – hub teetering angle (rad) with changes in rotor speed
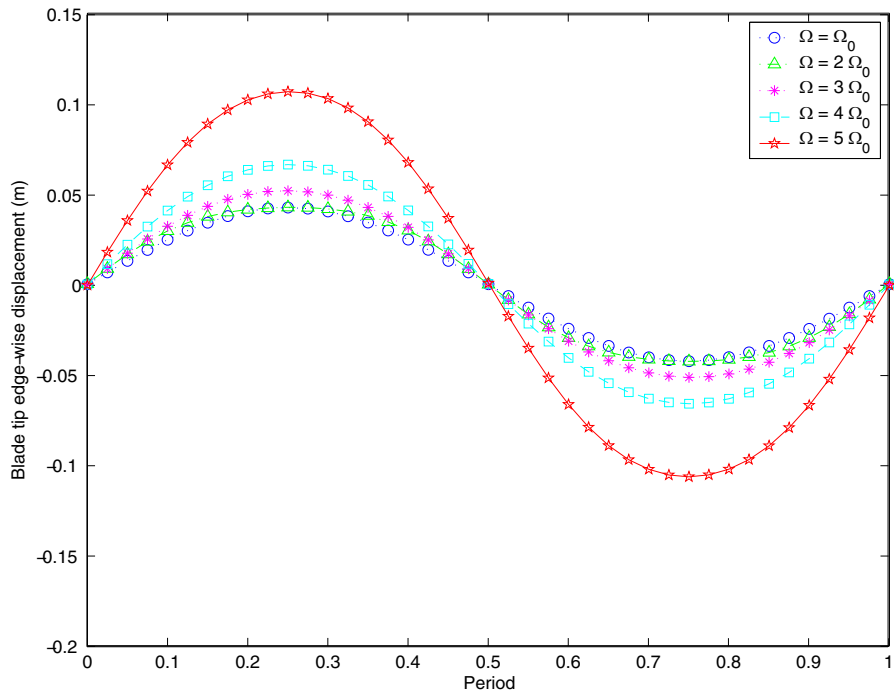
Figure 6.7: Periodic steady-state solution – blade tip edge-wise displacement (m) with changes in rotor speed
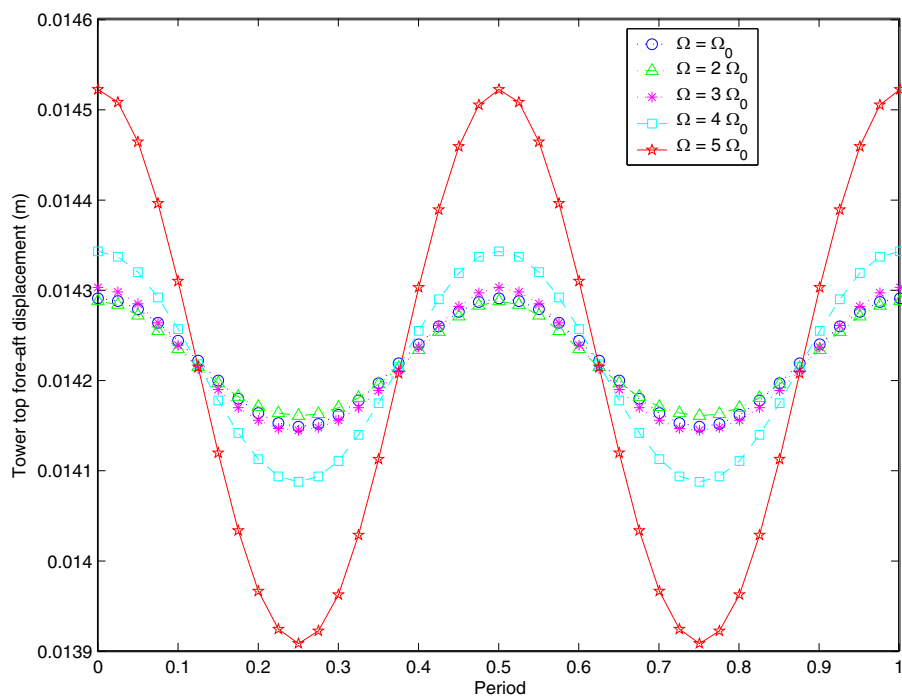
Figure 6.8: Periodic steady-state solution – tower top fore-aft displacement (m) with changes in rotor speed
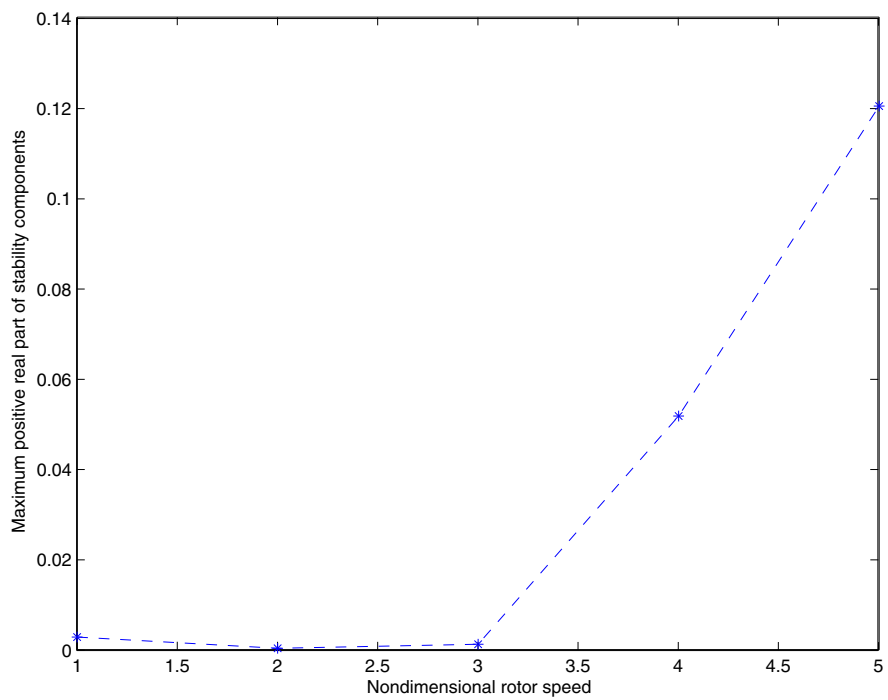
Figure 6.9: Maximum real part of Floquet stability components with changes in rotor speed
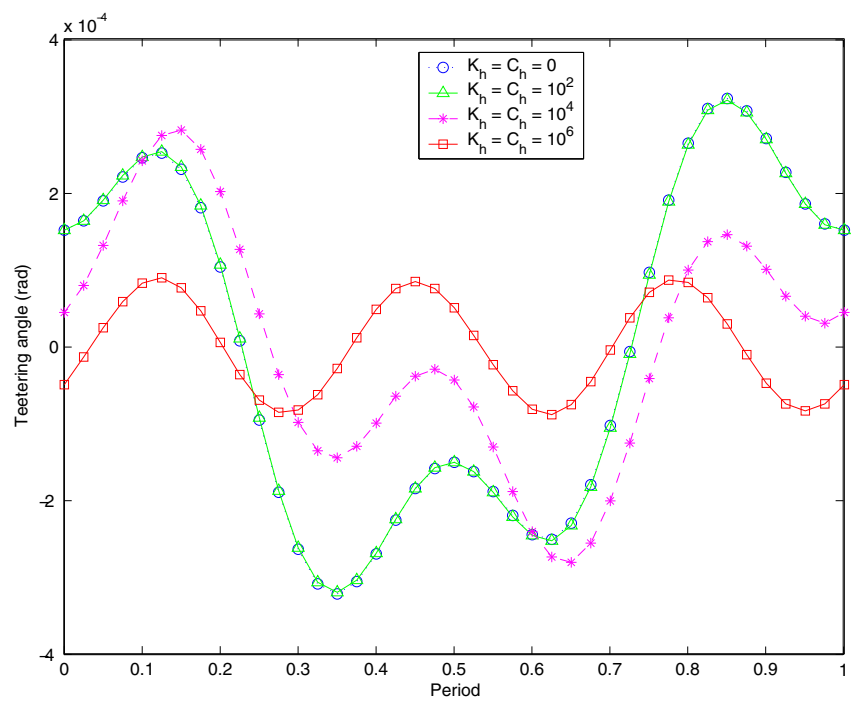
Figure 6.10: Periodic steady-state solution – hub teetering angle (rad) with changes in teetering stiffness and damping
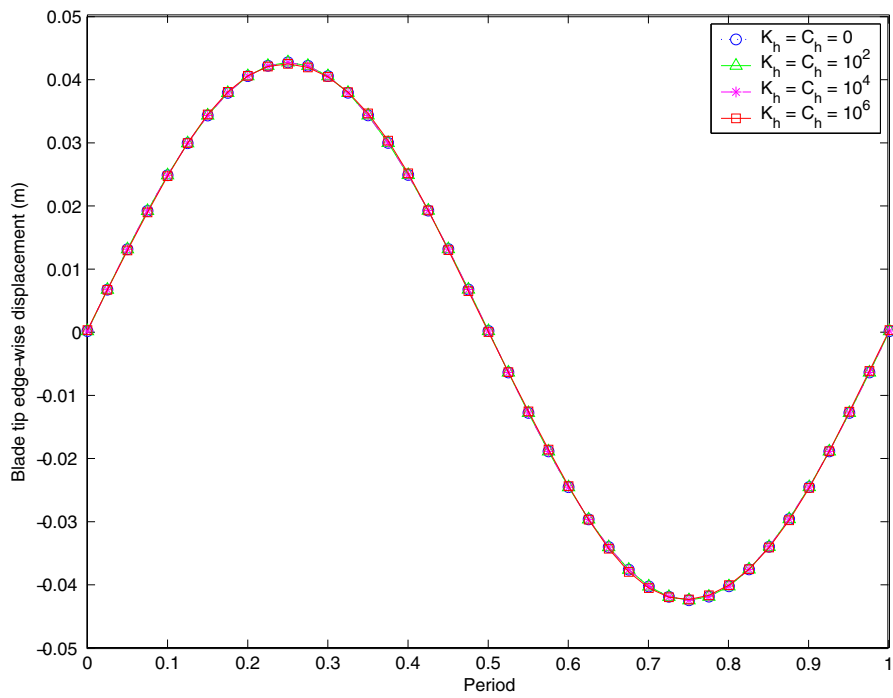
Figure 6.11: Periodic steady-state solution – blade tip edge-wise displacement (m) with changes in teetering stiffness and damping
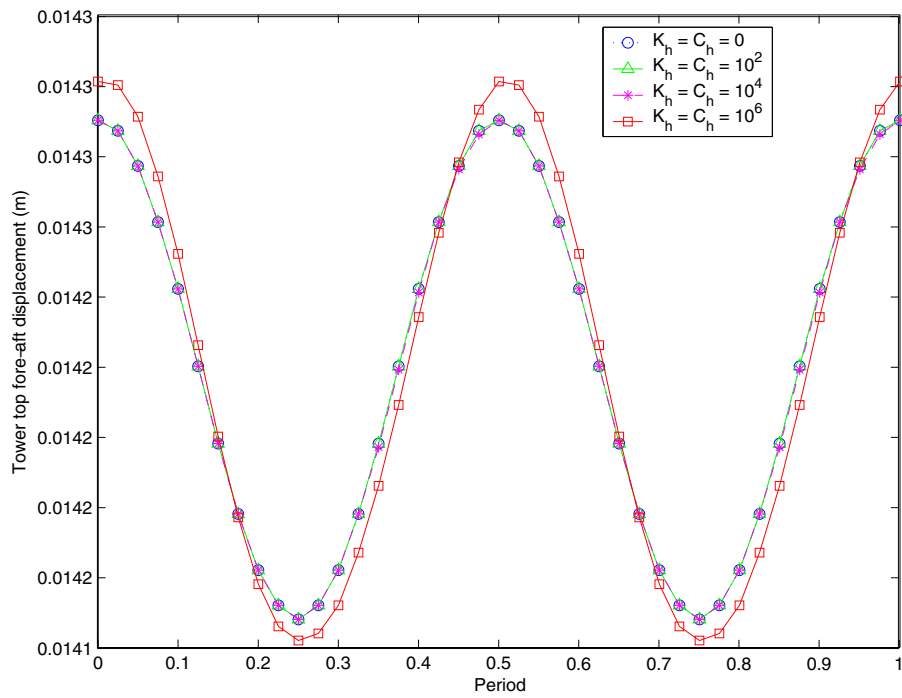
Figure 6.12: Periodic steady-state solution – tower top fore-aft displacement (m) with changes in teetering stiffness and damping
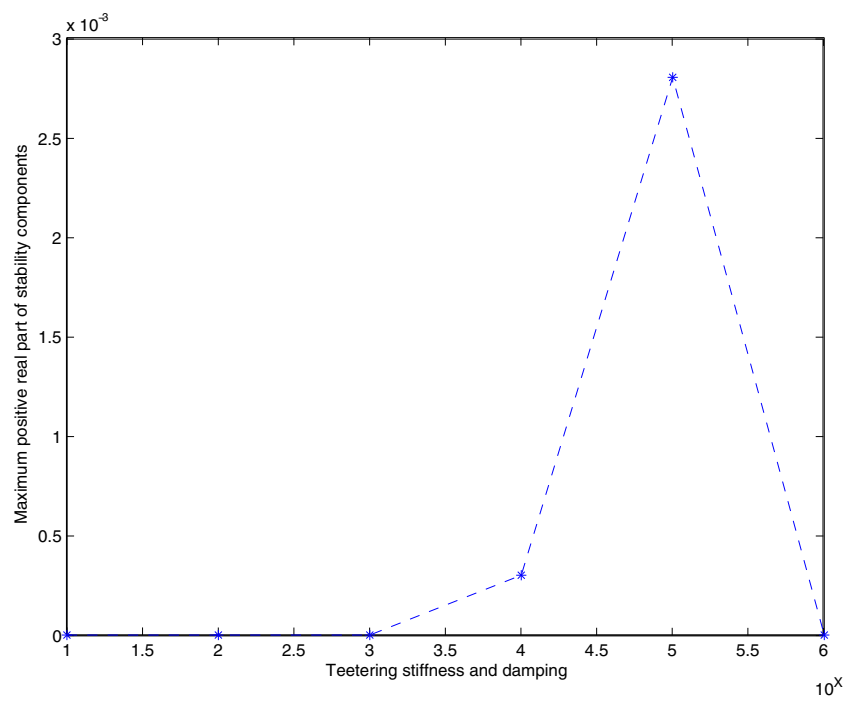
Figure 6.13: Maximum real part of Floquet stability components with changes in teetering stiffness and damping
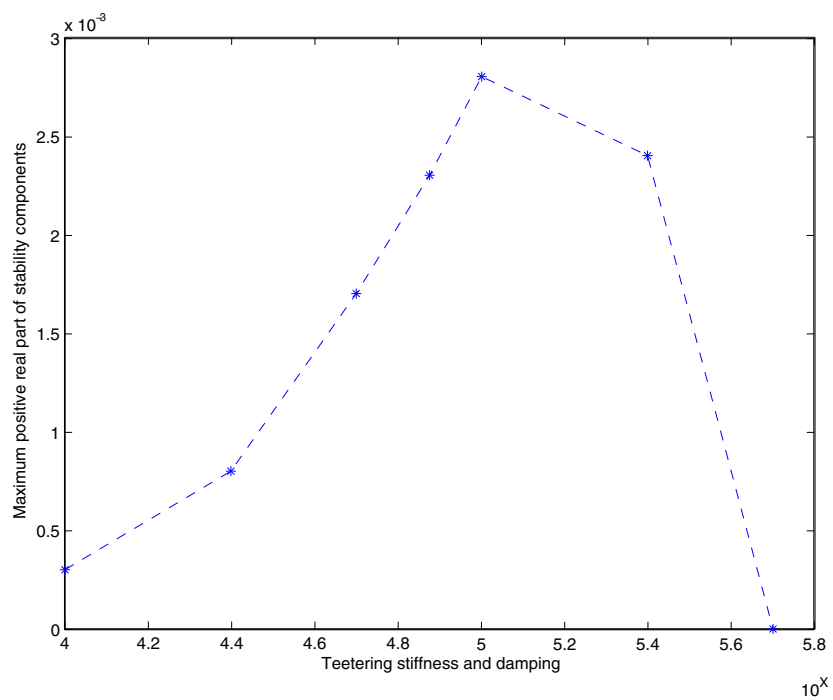
Figure 6.14: Maximum real part of Floquet stability components with changes in teetering stiffness and damping (high resolution)

Effect of Yawing Stiffness and Damping

Figure 6.15 shows that the amplitude of the steady-state response of the hub teetering angle decreases with a phase shift as the yawing stiffness and damping increase; it identifies the coupling between the yawing motion of the nacelle and the teetering motion of the hub. The results in the blade tip edgewise displacement and tower top fore-aft displacement are very similar with changes of stiffness and damping, as shown in Fig. 6.16 and Fig. 6.17, respectively, except that the stiffness and damping are very low in Fig. 6.17.
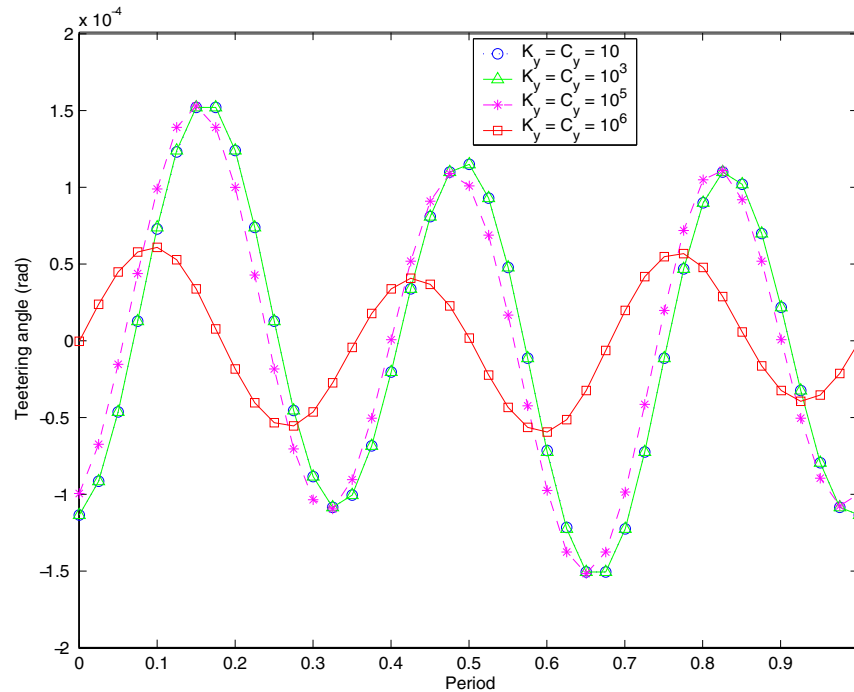
Figure 6.15: Periodic steady-state solution – hub teetering angle (rad) with changes in yawing stiffness and damping

Figure 6.18 shows that the instability measure decreases as stiffness and damping increase. The measure decreases dramatically in the case $K_h = C_h = 10^3$.

Effect of Teetering Hinge Offset

As expected, the periodic response of teetering angle and blade tip flapping displacement have mirror images as the sign of the hinge offset changes, and the amplitude increases as the magnitude of the hinge offset increases, as shown in Fig. 6.19 and Fig. 6.21. The results of the blade tip edgewise displacement look identical, as shown in Fig. 6.20.There are shifts in amplitude, i.e., differences in the static response, for the tower top fore-aft displacement, as shown in Fig. 6.22.

Figure 6.23 shows that the instability measure decreases as the teetering hinge offset increases from -0.2m to 0.2m, which is quite reasonable.
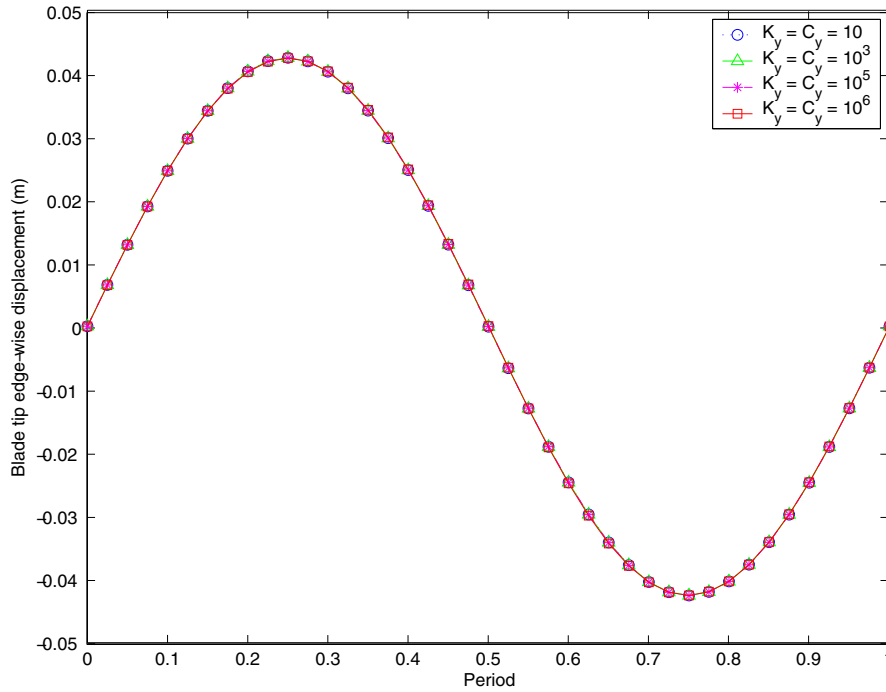
Figure 6.16: Periodic steady-state solution – blade tip edge-wise displacement (m) with changes in yawing stiffness and damping

Effect of Linearization

A conventional Floquet stability analysis is based on linearization about an approximate constant steady-state (approximate linearization). In this research, we perform the Floquet stability analysis with linearization about the periodic steady-state (consistent linearization), which is more realistic. Here, the instability measures, i.e., the maximum real part of the Floquet stability components, are calculated to investigate the effect of the different type of the linearization with the changes of parameters.

Figure 6.24 and 6.25 illustrate that the difference in the instability is not much affected by the change in teetering stiffness or damping and the change in the teetering hinge offset. In those cases, the instability measures from the approximate linearization are slightly larger than those in the consistent one. The effect of change in the precone angle is more evident, as shown in Fig. 6.26. While the precone angle is negative, the instability measures are about the same for both the approximate and the consistent linearization. As the precone angle increases into the positive region, however, the instability from the approximate linearization is larger than in the consistent one.

The differences in the instability measure with the change of the rotor speed (made dimensionless by Ω_0) and yawing stiffness/damping are more dramatic, as shown in Fig. 6.27 and Fig. 6.28. In the range of rotor speed larger than $3\Omega_0$, the instability in the consistent linearization is much larger than that in the approximate one, and the difference is maximum when the rotor speed is $5\Omega_0$. This means that a wind turbine that is structurally designed on the basis of the stability analysis from the constant steady-state might actually be quite unstable at some rotor speeds. (The CART model does not operate at such high rotor
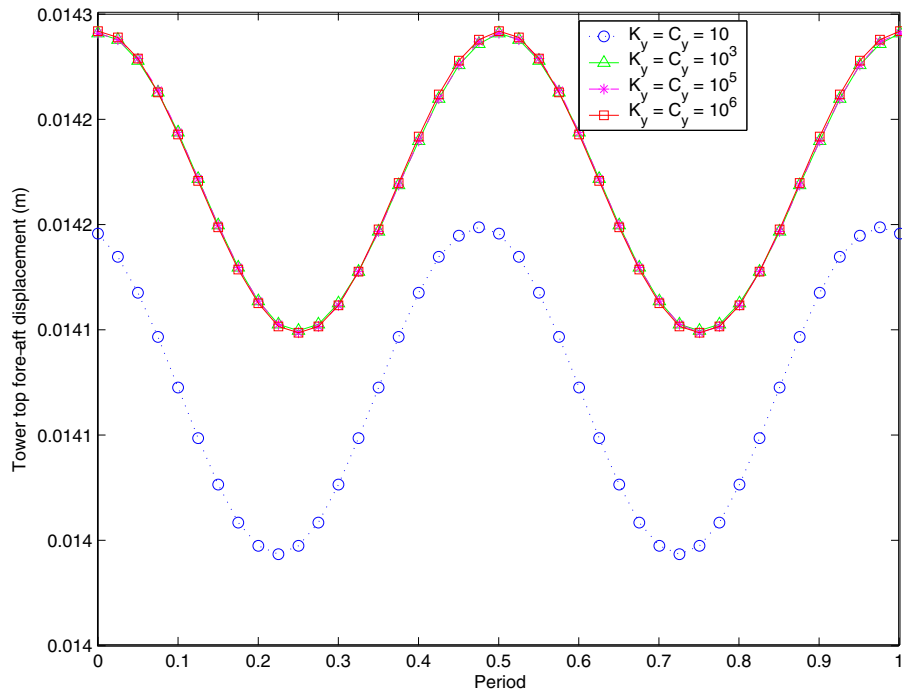
Figure 6.17: Periodic steady-state solution – tower top fore-aft displacement (m) with changes in yawing stiffness and damping

speeds, however, and is thus quite safe.) Similarly, where the yawing stiffness/damping is less than 10^4, the instability measure from the calculation based on consistent linearization is much larger than that of the approximate one.
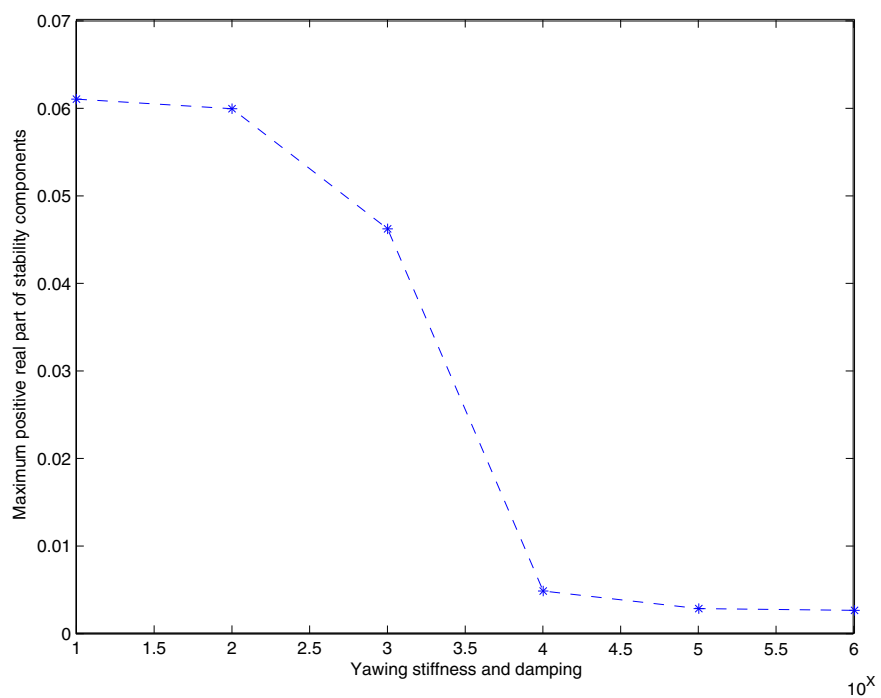
Figure 6.18: Maximum real part of Floquet stability components with changes in yawing stiffness and damping
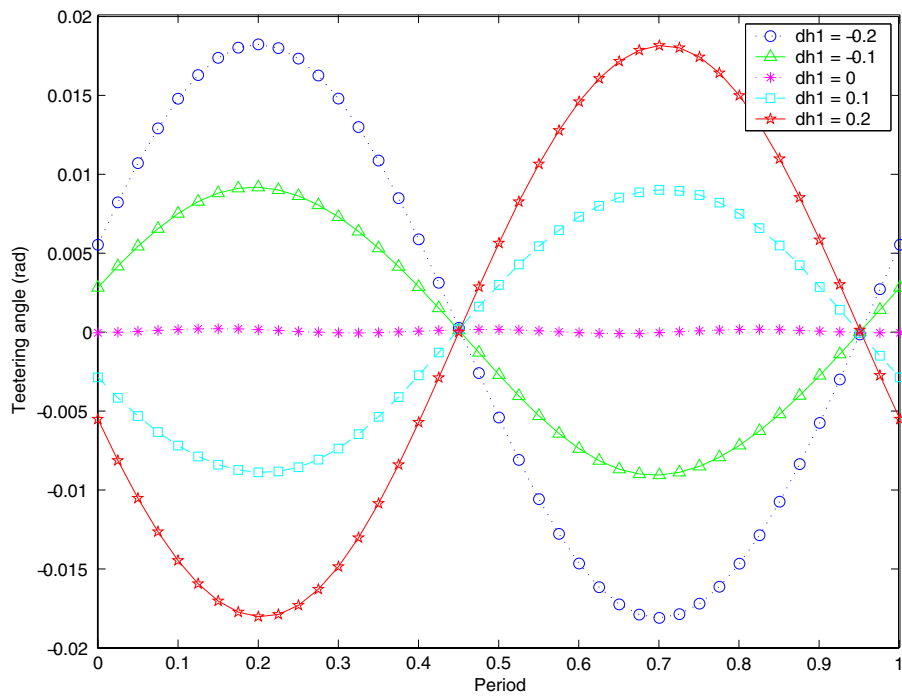
Figure 6.19: Periodic steady-state solution – hub teetering angle (rad) with changes in the teetering hinge offset
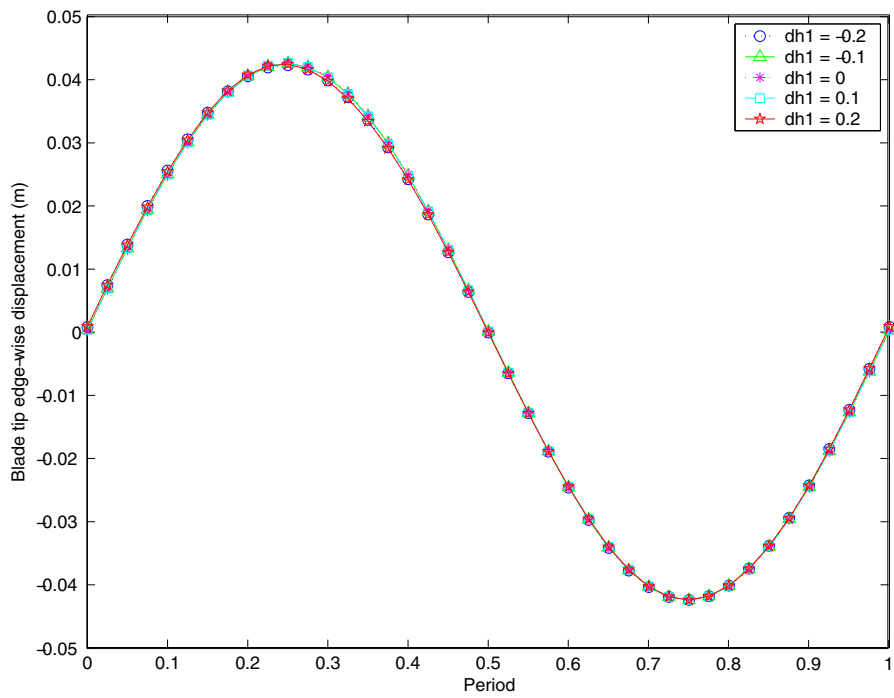
Figure 6.20: Periodic steady-state solution – blade tip edge-wise displacement (m) with changes in the teetering hinge offset
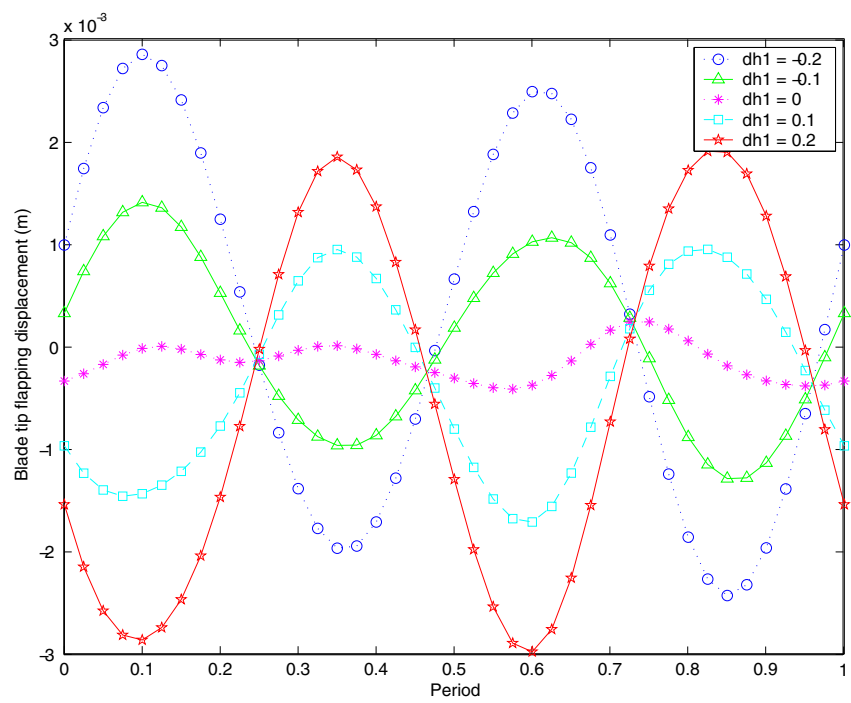
Figure 6.21: Periodic steady-state solution – blade tip flapping displacement (m) with changes in the teetering hinge offset
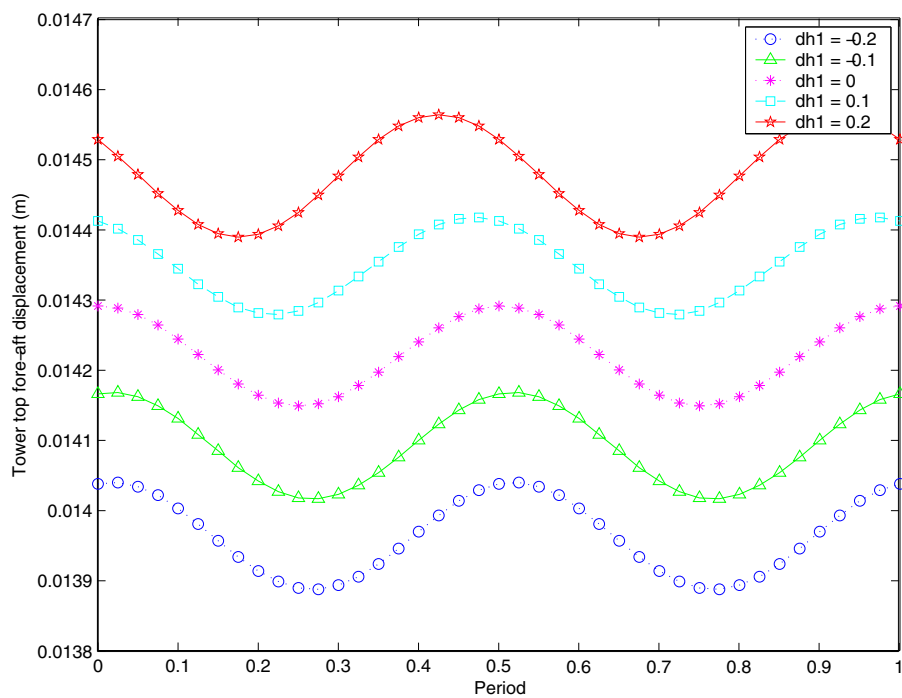
Figure 6.22: Periodic steady-state solution – tower top fore-aft displacement (m) with changes in the teetering hinge offset
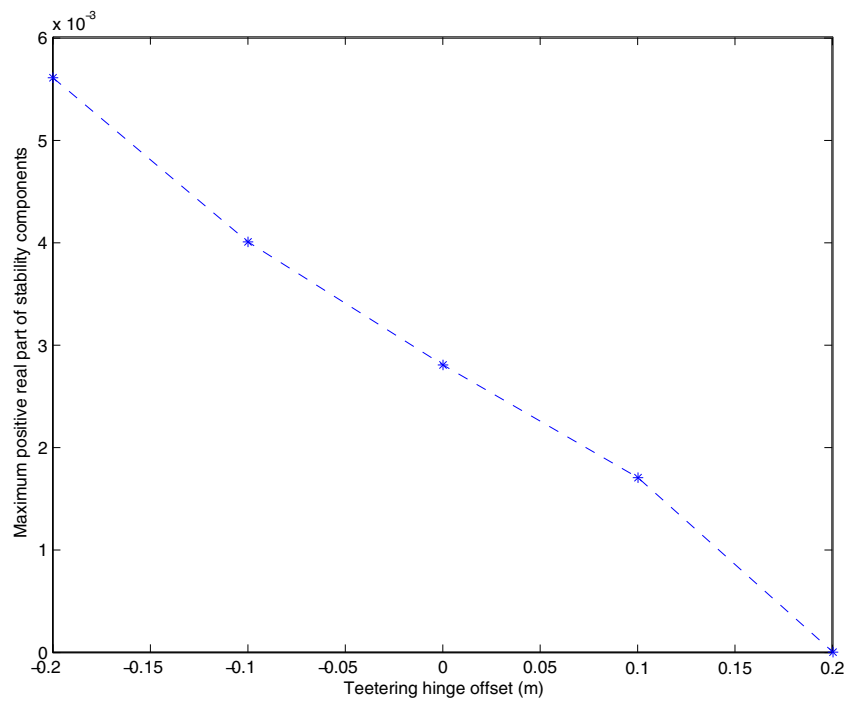
Figure 6.23: Maximum real part of Floquet stability components with changes in the teetering hinge offset
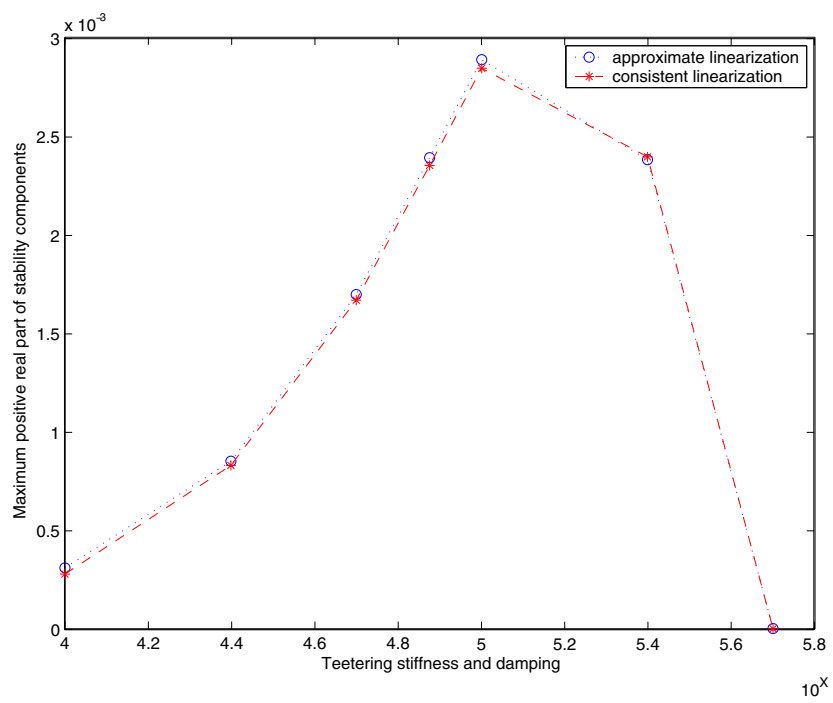
Figure 6.24: Maximum real part of Floquet stability components with changes in teetering stiffness and damping
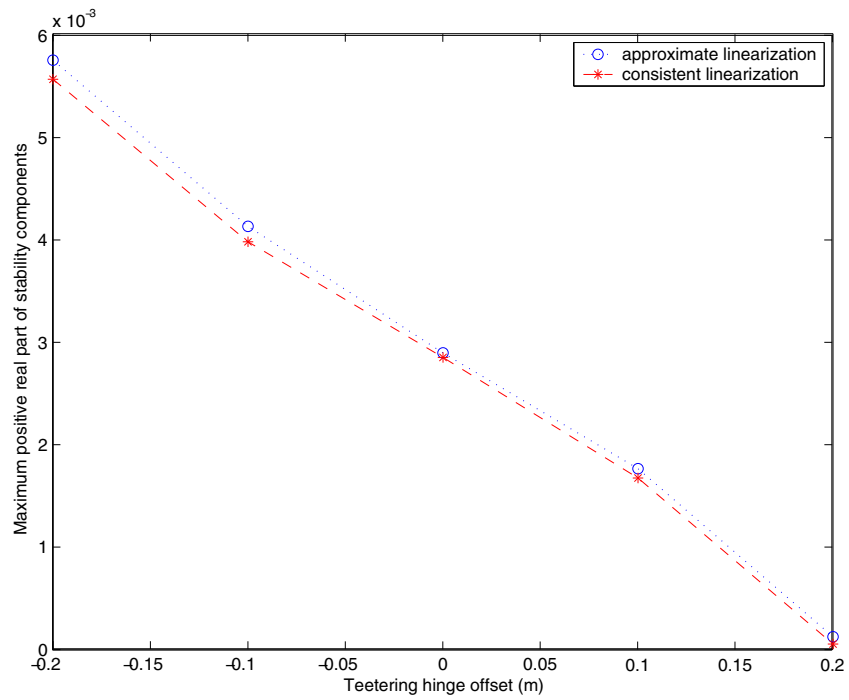
Figure 6.25: Maximum real part of Floquet stability components with changes in teetering hinge offset
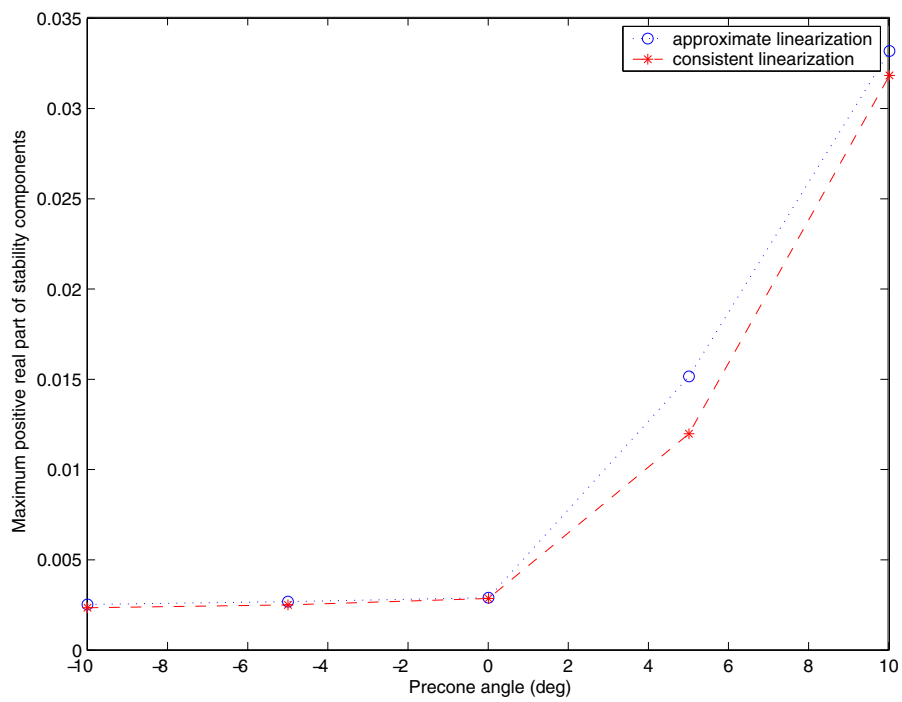
Figure 6.26: Maximum real part of Floquet stability components with changes in precone angle
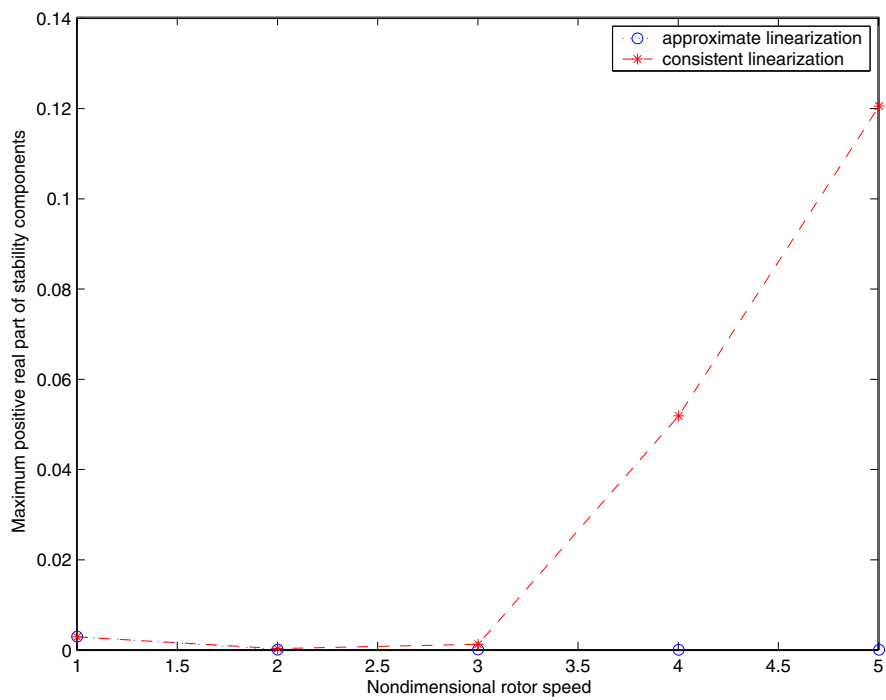
Figure 6.27: Maximum real part of Floquet stability components with changes in rotor speed
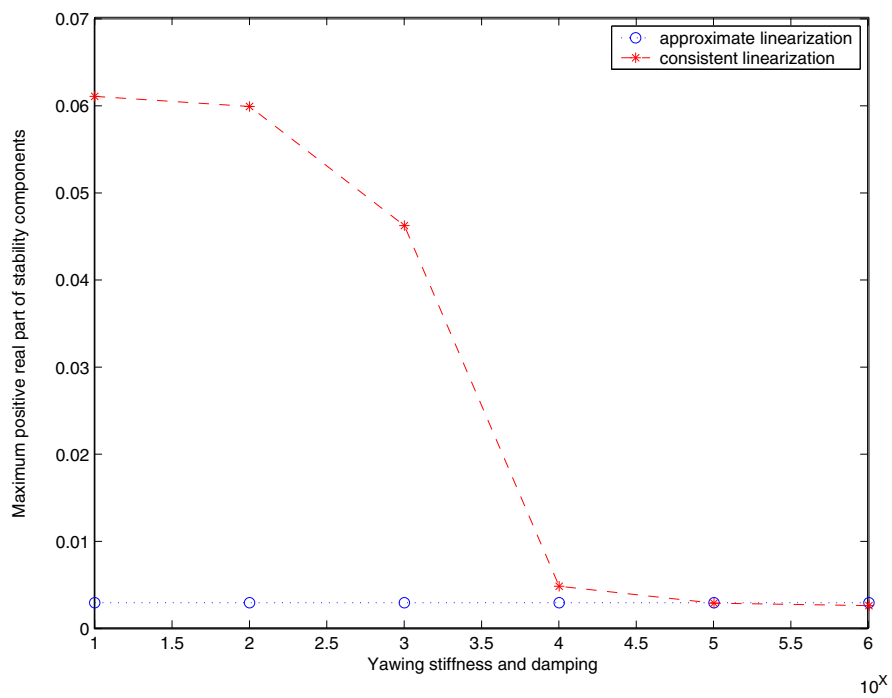
Figure 6.28: Maximum real part of Floquet stability components with changes in yawing stiffness and damping

Chapter 7

Conclusion

The goal of this work has been to develop a theoretical model for the aeroelastic analysis of rotating systems and a corresponding computational framework for application to wind turbine control design. Achievements have been made in the following areas:

Aeroelastic formulation

The research integrated the mixed variational formulation and Kane's method. The integration successfully derives system equations of relatively small size, which is important in control design for computational efficiency. The use of Kane's method with conventional generalized speeds is already highly advantageous over Lagrangian equations. Using the generalized speeds of this study further reduces the size of the equations by 30% for the general horizontal-axis wind turbine model. The reduction in computational cost for simulation or control design with the reduction in equations may be significant, but it was not investigated in this work.

The research develops the computational framework for an aeroelastic analysis of the whole wind turbine. The nonlinear simulation scheme is developed using a finite element in time, and the periodic steady-state solving procedure is achieved by the composition of the Jacobian matrix from the nonlinear simulation and the periodicity condition. To reduce the computational cost, a half-period time integration scheme is developed with the appropriate boundary conditions. The periodic steady-state framework is directly used for Floquet stability analysis, and it is equivalent to results of a conventional system matrix analysis, which is linearized about the periodic steady-state solutions.

This research can produce aeroelastic system equations linearized about the periodic steady-state solution, which is not common in the wind turbine dynamics field. The system equations are explicit functions of time, so they can be directly applied to control design.

Finite element program

A structured computer program, called WTFlex, has been developed for a horizontal-axis wind turbine aeroelastic analysis based on the methodo in this research. The code includes all the aspects described in this work; nonlinear simulation, periodic steady-state solution, Floquet analysis, and system equation

manipulation. The main contribution of this research and the code is first its achievement as a bridge directly connecting the flexible structural analysis and control design in wind turbine research.

Numerical validation

The methodology of the present research has been validated with other highly validated codes. Most results compared with ADAMS are satisfactory in numerical accuracy, except for results for the rotor speed of the flexible shaft and blade edge-wise motion. But they were validated with DYMORE, developed at the Georgia Institute of Technology, by studying more specific cases in great detail. Also, the results from the convergence study show the code is self-evident.

Wind turbine dynamic stability analysis

The analysis presents a dynamic analysis of CART (Control Advanced Research Turbine) with parametric studies, including precone angle, rotor speed, teetering/yawing stiffness and damping, and teetering hinge offset. Changes in these parameters cause changes in the amplitude and phase of the periodic steady state without a change in the frequency. Also, the periodic response identifies that there is a dynamic coupling between the yawing motion of the nacelle and the teetering motion of the hub. The instability measure, which is the maximum real part of the eigenvalues of the Floquet transition matrix, increases as the precone angle and rotor speed increase, and it decreases as yawing stiffness/damping and teetering hinge offset increase. Especially with the change in teetering stiffness and damping, it has the maximum value when stiffness and damping have unique values. Also, the Floquet instability is affected by the type of linearization. In the range where instability is low, i.e., the more stable case, the instability measure is not much affected by the type of linearization. But when the instability is high, i.e., the less stable case, the measure is very much affected by the linearization.

Bibliography

[1] BORRI, M., "Helicopter rotor dynamics by finite element time approximation," *Computers and Mathematics with Applications*, vol. 12A, pp. 149 – 160, January 1986.

[2] CESNIK, C. E. S., and HODGES, D. H., "VABS: A new concept for composite rotor blade cross-sectional modeling," *Journal of the American Helicopter Society*, vol. 42, no. 1, pp. 27 – 38, 1997.

[3] GESSOW, A., and MYERS, G. C., *Aerodynamics of the Helicopter*. Bethesda, MD: College Park Press, 1985.

[4] HOCHSTADT, H., *Differential Equations*. New-York: Dover Publications, Inc., 1964.

[5] HODGES, D. H., "An extension of blade element momentum theory to incorporate nonlinear lift and drag coefficients," *Journal of the American Helicoper Society*, vol. 25, pp. 48–50, October 1980.

[6] HODGES, D. H., "A mixed variational formulation based on exact intrinsic equations for dynamics of moving beams," *International Journal of Solids and Structures*, vol. 26, no. 11, pp. 1253 – 1273, 1990.

[7] HODGES, D. H., SHANG, X., and CESNIK, C. E. S., "Finite element solution of nonlinear intrinsic equations for curved composite beams," *Journal of the American Helicopter Society*, vol. 41, no. 4, pp. 313 – 321, 1996.

[8] KANE, T. R., and LEVINSON, D. A., *Dynamics: Theory and Applications*. New York, New York: McGraw-Hill Book Company, 1985.

[9] MITIGUY, P. C., and KANE, T. R., "Motion variables leading to efficient equations of motion," *International Journal of Robotics Research*, vol. 15, pp. 522 – 532, October 1996.

[10] NAYFEH, A., and MOOK, D., *Nonlinear Oscillations*. New York: John Wiley & Sons, 1979.

[11] PATIL, M. J., HODGES, D. H., and CESNIK, C. E. S., "Nonlinear aeroelastic analysis of complete aircraft in subsonic flow," *Journal of Aircraft*, vol. 37, no. 5, pp. 753 – 760, 2000.

[12] PETERS, D. A., "Fast Floquet theory and trim for multi-bladed rotorcraft," *Journal of the American Helicopter Society*, vol. 39, pp. 82–89, October 1994.

[13] STOL, K., and BIR, G., "Geometry and structural properties for controls advanced research turbine (CART)," Tech. Rep. TP-32087, NREL, 2002.

Appendix A
WTFlex User's Guide

Introduction

This manual describes a new research computer code for the analysis of flexible Horizontal Axis Wind Turbines (HAWT's) called WTFlex, version 1.0. The work leading to the development of this code was sponsored by the National Wind Technology Center, NREL, under subcontract No. XCX-9-29204-03. The code was developed under the oversight of the principal investigator, Prof. Dewey H. Hodges. Dr. Donghoon Lee wrote the code as a graduate research assistant and was awarded the Ph.D. degree in December 2003.

The purpose of this manual is to provide a simple and practical explanation of how to use the code. The theoretical basis of the methodology for this code has been presented in [9] as well as in the body of this report.

We first explain how to install the code and set the data files. Next we show the capabilities and limitations of the code by presenting the basic assumptions of the methodology and analysis and the fixed and free parameters of the model. We then describe how to perform a Floquet stability analysis and check the results, especially mode shapes. Finally we describe how to perform nonlinear simulations.

The present code and graphical user interface (GUI) for WTFlex 1.0 are only for structural dynamics analysis of HAWT's. An aeroelastic analysis and code has been developed as well, making use of the aerodynamic model described in the text. However, WTFlex proved to be far less robust in its ability to extract a periodic solution when running with the aerodynamics module than it is without it. Moreover, since NREL's own aerodynamic theories are better suited for HAWT's, a new aerodynamics module should be developed along with a modified GUI.

Getting Started with WTFlex

Installation of WTFlex

Once you have the zip file "WTFlex.zip" please follow the following procedure:
Step 1. Extract the zip file into a new folder named "WTFlex." You should find that there are 2 sub-folders named "WTFlex_Flq" and "WTFlex_TM." The former is for Floquet stability analysis with constant rotor speed, and the latter is for time simulation with external excitations.
Step 2. Launch "Matlab" on your computer.
Step 3. Set "MatLab path" of the folder "WTFlex_Flq" or "WTFlex_TM" depending on your purposes. If your version of MatLab is higher than 6.0, just set your current directory as the folders.

Step 4. Copy and paste the appropriate data files for blade and tower into folder "data", if you want to use discretized data for the bodies (this will be explained later).
Step 5. Type "WTFlex_Flq" or "WTFlex_TM" in the MatLab command window, depending on your purposes. The program's GUI should be shown on your monitor
Step 6. Input the running parameters (this will be explained later).
Step 7. Run WTFlex by pushing the button <Solve>.
Step 8. Get results (this will be explained later).

Setting of Data Files

To perform the analysis for nonuniform flexible bodies, WTFlex requires users to set data files, which are compatible with the format the code requires:
- The file name for blade and tower properties are respectively should be "blade.txt" and "tower.txt".
- Each row should represent the station of the body along with the axial direction, and each column represents the type of material properties.
- The first column should represent the distance from the root of the body to the station.

The recent paper [14] contains an appropriate example of data files.

Scope and Graphical User Interface (GUI)

Figure 1 shows the general model of HAWT's. Here the rigid bodies subsystem is composed of the nacelle, the shaft, and the rotor hub. The flexible body subsystems are comprised of the two blades and the tower.

Basic Assumptions

- There is no air
- Number of blades is two, and they are identical and equally spaced
- Nacelle is one rigid body which has 1 degree of freedom, yaw motion with respect to the tip of the tower
- Generator and shaft is one rigid body which has 1 degree of freedom, rotational motion with respect to the nacelle
- Hub is a rigid body which has 1 degree of freedom, teetering motion with respect to the shaft
- Bed plate is a point mass fixed at nacelle
- Teeter axis is at the end of the rigid shaft
- Tilt axis is at the tower top
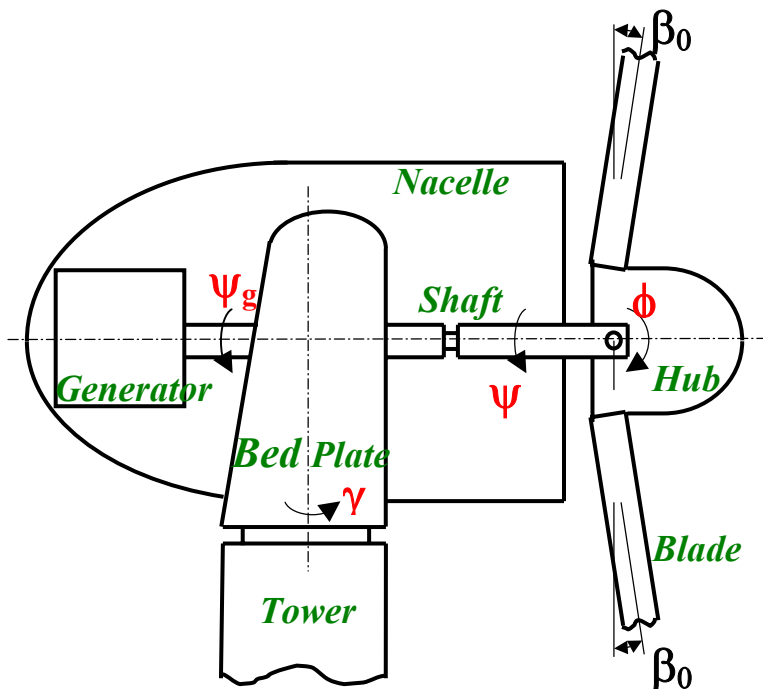
Figure 1. Schematic of HAWT Model
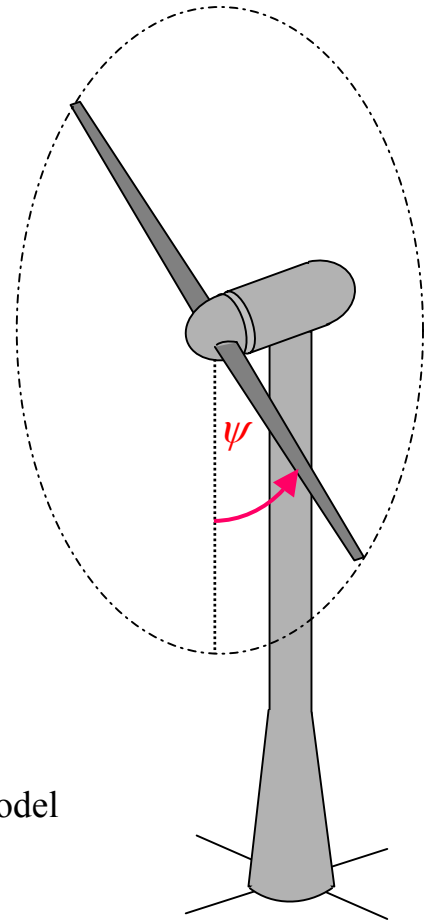
User-Controllable Parameters (in GUI)

Figure 2 shows the geometric parameters of HAWT. The free parameters including the geometric parameters are as follows:
  (1) Lumped parameters
    (a) Geometry
    - c_n1: longitudinal distance from yaw axis to nacelle c.g.
    - c_n2: vertical distance from bed plate to nacelle c.g.
    - c_s: distance from yaw axis to shaft c.g.
    - c_h: distance from teetering axis to hub c.g. (note carefully that it is positive in the longitudinal direction)
    - d_h1: longitudinal distance from hub c.g. to blade root.
    - d_h2: lateral distance from hub c.g. to blade root.
    - L_b: length of blades
    - L_t: length of tower
    - tilt: tilt angle of nacelle with respect to tower top
    - pcon: precone angle of blade (β_0)
    - pitch: pitch angle of blade
    where the units for all lengths and angles are [m] and [deg], respectively.
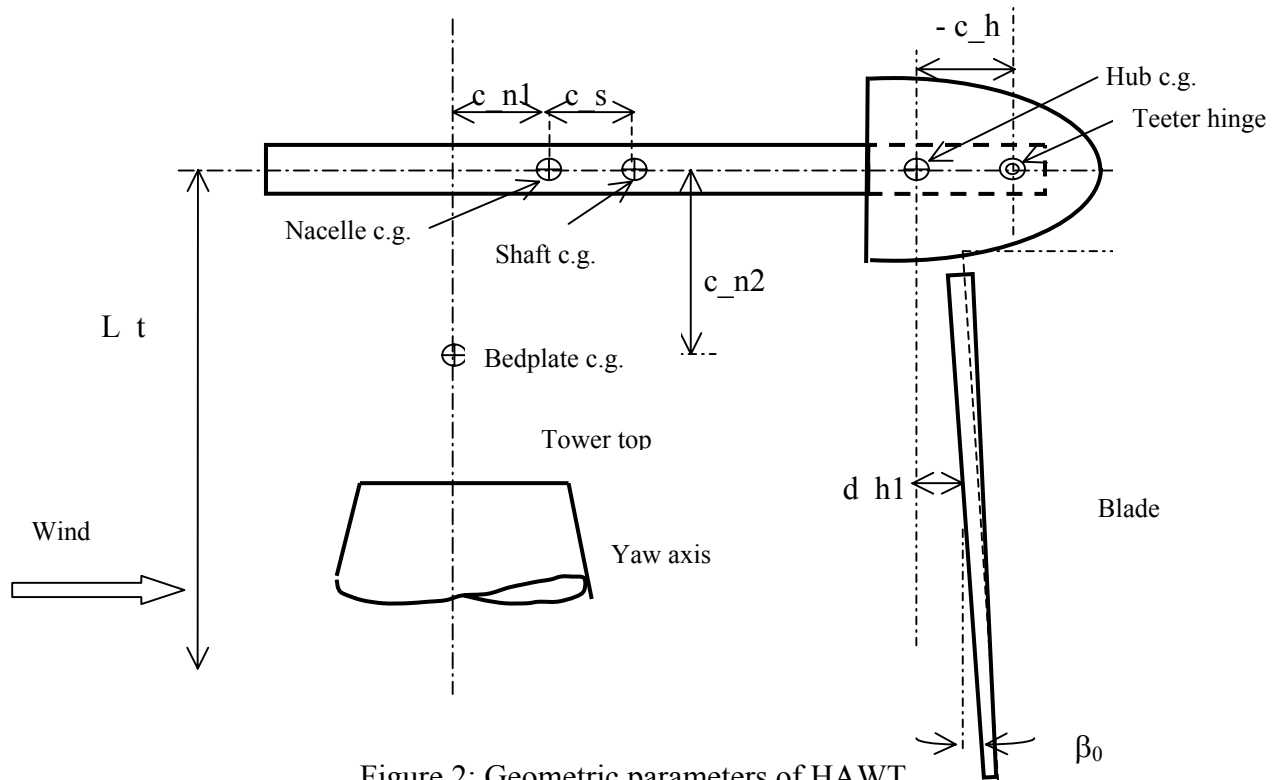
Figure 2: Geometric parameters of HAWT

 (b) Material
- m_n: total mass of nacelle
- In_1: moment of inertia of nacelle about lateral axis
- In_2: moment of inertia of nacelle about longitudinal axis
- In_3: moment of inertia of nacelle about vertical axis
- m_s: total mass of shaft
- Is_lt: moment of inertia of shaft about lateral axis
- Is_lg: moment of inertia of shaft about longitudinal axis
- m_h: total mass of hub
- Ih_1: moment of inertia of hub about lateral axis
- Ih_2: moment of inertia of hub about longitudinal axis
- Ih_3: moment of inertia of hub about vertical axis

where the units for all masses and moment of inertias are [kg] and [kg-m^2], respectively, and all the moment of inertias are defined at each body's center of mass and in the basis of each body's frame.

(c) Stiffness and Damping
- K_y: yawing stiffness
- C_y: yawing damping
- K_h: teetering stiffness

- C_h: yawing dampingWhere the unit of all the stiffnesses and dampings are respectively [N-m/rad] and [N-m/rad^2]

(2) Distributed Parameters (per unit length)

Users can set distributed parameters with constant values (for uniform beams) or discretized values (for a non-uniform beams). Also, one can model blades as anisotropic beams by setting the off-diagonal components of stiffness matrix of blade (for example, S14). WTFlex and its GUI supports the input of the anisotropic materials by means of the 4×4 or 6×6 cross-sectional stiffness matrix, which is represented as

$$\begin{Bmatrix} F \\ M \end{Bmatrix} = [S] \begin{Bmatrix} \gamma \\ \kappa \end{Bmatrix}$$

where F and M are column matrices the elements of which are components of cross-sectional force and moment vectors in the deformed beam frame, and γ and κ are column matrices of cross-sectional strain measures, extensional and transverse shear measures in the former and twist and curvature measures in the latter. To use discretized data, the user should mark on the blank of each item, and set the number of the column corresponding to the item in the data file. Also the symbols in the GUI represent:

- m_b: mass of blades
- Ib_2: moment of inertia of blades per about tangential axis
- Ib_3: moment of inertia of blades about rotational axis
- m_t: mass of tower
- It_1: moment of inertia of tower about lateral axis
- It_2: moment of inertia of tower about longitudinal axis
- GJt: torsional stiffness of tower
- EIt1: bending stiffness of tower about lateral axis
- EIt2: bending stiffness of tower about longitudinal axis
- EAt: axial stiffness of tower

(3) Running options
- OMEGA (WTFlex_Flq): nominal speed of shaft
- Time Int (WTFlex_TM): the time interval for nonlinear simulation
- Time Steps: number of time elements respectively in one period (WTFlex_Flq) and in the time interval (WTFlex_TM)
- Blade Elements: number of space elements in one blade
- Tower Elements: number of space elements in tower

(4) Results (WTFlex_Flq)
- Stability Exponents: by checking the blank, a data file, which contains the results of stability exponents (to be explained later), is saved into folder "results".
- Dominant Eigenvalue: by checking the blank, a data file, which contains the results of dominant eigenvalues (to be explained later), is saved into folder "results".
- Mode shape: after all the calculations are finished, this button will pop up. If a user clicks this button, another window will pop up to show mode shapes and eigenvectors (to be explained later).

(5) Excitations (WTFlex_TM)

All the excitation is defined as form of sinusoidal function as

$$F = A\sin(xt + y)$$

where A is the amplitude, x is the coefficient of time, t is the time, and y is the phase angle.

- TOR: torsion applied to shaft
- Fu_2: body fixed force applied to upper blade tip for edgewise direction
- Fu_3: body fixed force applied to upper blade tip for flapping direction
- Fd_2: body fixed force applied to lower blade tip for edgewise direction
- Fd_3: body fixed force applied to lower blade tip for flapping direction
- Ft_1: body fixed force applied to tower top for lateral direction
- Ft_2: body fixed force applied to tower top for fore-aft direction

Stability Analysis (WTFlex_Flq)

Calculation Procedure

By clicking the button "Solve" after setting all the parameters as previously explained, the user will find the following messages consecutively on the "MatLab command window":

- <Constant Steady State>: means that the code is calculating constant steady-state solutions, used as an initial guess for calculating the periodic steady-state solution.
- <ErrCSS = number>: represents the numerical error at the current iteration in calculating the constant steady-state solution, which is defined as the L^2 norm of the equation vector using the current temporary solutions.
- <Periodic Steady State & Floquet Stability>: means that the code is calculating the periodic steady-state solutions and the Floquet stability analysis with linearization about the periodic steady-state solutions.
- <ErrPSS = number>: represents the numerical error to calculate the periodic steady-state solution, which is defined as the L^2 norm of equation vector with the temporary solutions of the iteration. If this value diverges, we recommend that the user increase the number of time elements.
- <Dominant Eigenvalue>: means that the code is calculating the dominant eigenvalues.
- <All the calculation is finished>: All the results are calculated.

Types of Results

(1) Stability Exponents: They are found by the Floquet analysis for the system and are references for dynamic stability of the system, represented as

$$s_i = \frac{1}{T}\log|\lambda_i| + j\frac{1}{T}\tan^{-1}\frac{\text{Im}(\lambda_i)}{\text{Re}(\lambda_i)}$$

where λ_i is the ith eigenvalue of the Floquet transition matrix.

(2) Dominant Eigenvalues: They are found by the DFT (Discrete Fourier Transform) of the time history of variables, with the initial condition being the eigenvector corresponding to the eigenvalue of the Floquet transition matrix. This procedure can be represented as

$$\hat{Z}(t) = Z(t)e^{\lambda t}$$

$$\lambda_{dom} = \lambda + \max[\text{FFT}(\hat{Z}(t))]$$

where $Z(t)$ is the time history of a typical variable of the state vector, with initial condition being the eigenvector of the Floquet transition matrix; λ is the eigenvalue per revolution of the Floquet transition matrix (eigenvalue/period); FFT is the fast Fourier transform function; and λ_{dom} is the dominant eigenvalue.

(3) Mode shapes: There are three Figures that show the mode shapes corresponding to each eigenvalue: front view, side view, and plane view. The directions are shown in Figure 3.

The components of eigenvector for torsional motion of blades are presented with values instead of the mode shape because it is not effective to estimate the modes. The resulting window showing the information on the mode shapes is presented in Figure 4. There are the arrows and numbers to explain the buttons and figures.

1. Dominant eigenvalue (per revolution) of the present mode
2. Button to move to the next and previous mode shape
3. Button to see the components of eigenvector for the side view
   - Teeter: teeter angle of the hub
   - Tower: fore-aft bending motions of the tower elements
   - Ublade: flapping motions of the upper blade elements
   - Lblade: flapping motions of the lower blade elements
4. Button to see the components of eigenvector for the plane view
   - Yaw: yaw angle of the nacelle
   - Tower: twisting motions of the tower elements
5. Button to see the components of eigenvector for the front view
   - Tower: lead-lag motions of the tower elements
   - Ublade: lead-lag motions the upper blade elements
   - Lblade: lead-lag motions of the lower blade elements
6. Button to see the components of eigenvector for the blade torsion
   - Ublade: torsional motions of the upper blade elements
   - Lblade: torsional motions of the lower blade elements
From 3 to 6, please note the eigenvector is normalized by its maximum component
7. Side view
   - Yellow: tower
   - Black: shaft
   - Blue: upper blade
   - Green: lower blade
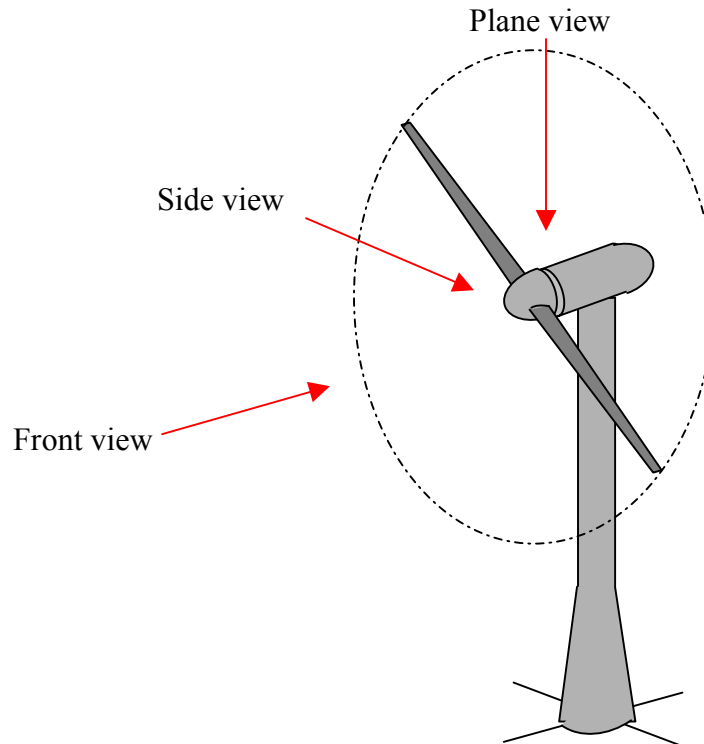
Figure 3. Directions for viewing mode shapes

8. Plane view
   - Blue: the original orientation of the nacelle
   - Green: nacelle and shaft
9. Front view
   - Yellow: tower
   - Red: hub
   - Blue: upper blade
   - Green: lower blade

Nonlinear Simulation (WTFlex_TM)

For nonlinear simulation, the initial condition of the wind turbine is stationary with rotor vertical position. Same as the "Stability Analysis", clicking the button "Solve" activates the code to calculate. After the message "All the calculation is finished" 10 graphs will pop up on the monitor:
   - Yawing angle of nacelle [rad]
   - Teetering angle of hub [rad]

- Rotational angle of shaft [rad]
- Rotational speed of shaft [rad/sec]
- Tower top lateral displacement [m]
- Tower top fore-aft displacement [m]
- Upper blade (initially) tip edgewise displacement [m]
- Upper blade (initially) tip flapping displacement [m]
- Lower blade (initially) tip edgewise displacement [m]
- Lower blade (initially) tip flapping displacement [m]

Figure 4. Windows for mode shapes
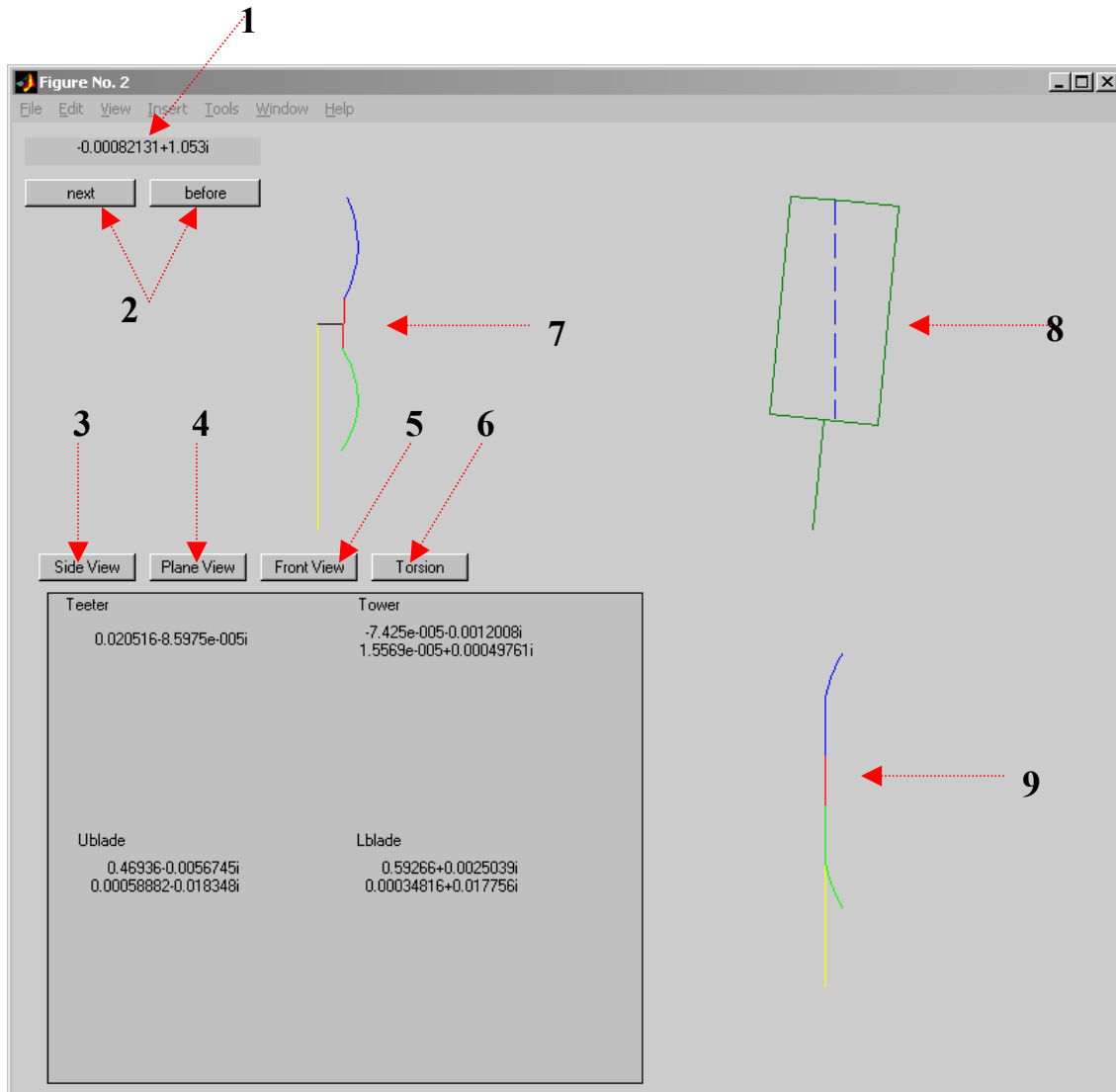
Abstract

A computational framework for aeroelastic analysis of Horizontal Axis Wind Turbines (HAWT's) is presented. The structural model is separated into multi-rigid-body and flexible-body parts. Equations for the former are derived using Kane's method, and the flexible portions are assumed to be beam-like structures, and are described using a mixed formulation. This formulation leads to equations of motion of a relatively low order in terms of geometrically-exact beam finite elements. The flexible and rigid subsystems are coupled with an aerodynamic model to form an aeroelastic analysis. A nonlinear, periodic, steady-state solution and a linearized transient solution about the periodic steady state are obtained. The computational framework for two-bladed, horizontal axis wind turbines is built using time finite elements over a half-period. The linearized ordinary differential equations have periodic coefficients in time, and a Floquet stability analysis for the linearized system is directly undertaken using quantities obtained in the periodic steady-state calculation. Numerical results are presented for horizontal axis wind turbines including steady-state response and Floquet characteristic exponents and operating mode shapes. Effects are investigated of parameters such as pre-cone, rotor speed, teetering hinge lateral offset, teetering and yawing stiffness and damping, and composite blade properties on the dynamics of the system.

REPORT DOCUMENTATION PAGE

Form Approved
OMB No. 0704-0188

The public reporting burden for this collection of information is estimated to average 1 hour per response, including the time for reviewing instructions, searching existing data sources, gathering and maintaining the data needed, and completing and reviewing the collection of information. Send comments regarding this burden estimate or any other aspect of this collection of information, including suggestions for reducing the burden, to Department of Defense, Executive Services and Communications Directorate (0704-0188). Respondents should be aware that notwithstanding any other provision of law, no person shall be subject to any penalty for failing to comply with a collection of information if it does not display a currently valid OMB control number.
PLEASE DO NOT RETURN YOUR FORM TO THE ABOVE ORGANIZATION.

1. **REPORT DATE** *(DD-MM-YYYY)* September 2004	2. **REPORT TYPE** Subcontract Report	3. **DATES COVERED** *(From - To)* 9/10/1999 - 10-31-2003

4. **TITLE AND SUBTITLE** Multi-Flexible-Body Analysis for Application to Wind Turbine Control Design	5a. **CONTRACT NUMBER** DE-AC36-99-GO10337
	5b. **GRANT NUMBER**
	5c. **PROGRAM ELEMENT NUMBER**
6. **AUTHOR(S)** D. Lee and D.H. Hodges	5d. **PROJECT NUMBER** NREL/SR-500-35228
	5e. **TASK NUMBER** WER4.7001
	5f. **WORK UNIT NUMBER**

7. **PERFORMING ORGANIZATION NAME(S) AND ADDRESS(ES)** Georgia Tech Research Corporation 400 Tenth Street, NW, Room 246 Atlanta, Georgia 30332-0420	8. **PERFORMING ORGANIZATION REPORT NUMBER** XCX-9-29204-03

9. **SPONSORING/MONITORING AGENCY NAME(S) AND ADDRESS(ES)** National Renewable Energy Laboratory 1617 Cole Blvd. Golden, CO 80401-3393	10. **SPONSOR/MONITOR'S ACRONYM(S)** NREL
	11. **SPONSORING/MONITORING AGENCY REPORT NUMBER** NREL/SR-500-35228

12. DISTRIBUTION AVAILABILITY STATEMENT
National Technical Information Service
U.S. Department of Commerce
5285 Port Royal Road
Springfield, VA 22161

13. SUPPLEMENTARY NOTES
NREL Technical Monitor: Alan Laxson

14. ABSTRACT *(Maximum 200 Words)*
A computational framework for aeroelastic analysis of Horizontal Axis Wind Turbines (HAWT's) is presented. The structural model is separated into multi-rigid-body and flexible-body parts. Equations for the former are derived using Kane's method; and the flexible portions are assumed to be beam-like structures, described using a mixed formulation. The equations of motion are of a relatively low order in terms of geometrically-exact beam finite elements. The flexible and rigid subsystems are coupled with an aerodynamic model to form an aeroelastic analysis. A nonlinear, periodic, steady-state solution and a linearized transient solution about the periodic steady state are obtained. The computational framework for two-bladed, HAWT's is built using time finite elements over a half-period. The linearized ordinary differential equations have periodic coefficients in time, and a Floquet stability analysis for the linearized system is directly undertaken using periodic steady state results. Numerical results are presented for horizontal axis wind turbines including steady-state response and Floquet characteristic exponents and operating mode shapes. Effects on the dynamics of the system for pre-cone, rotor speed, teetering hinge lateral offset, teetering and yawing stiffness and damping, and composite blade properties are investigated. A user's guide for the computer program WTFlex is included in the appendix.

15. SUBJECT TERMS
wind energy; wind turbine; flexible-body; control design; structural modeling; aeroelastic; HAWT

16. SECURITY CLASSIFICATION OF:			17. LIMITATION OF ABSTRACT	18. NUMBER OF PAGES	19a. NAME OF RESPONSIBLE PERSON
a. REPORT Unclassified	b. ABSTRACT Unclassified	c. THIS PAGE Unclassified	UL		
					19b. TELEPONE NUMBER *(Include area code)*

Standard Form 298 (Rev. 8/98)
Prescribed by ANSI Std. Z39.18

F1146-E(05/2004)